Observations of the X-ray Pulsars XTE J1946+274, 4U 0115+634, and GX 304−1

Der Naturwissenschaftlichen Fakultät
der Friedrich-Alexander-Universität
Erlangen-Nürnberg
zur

Erlangung des Doktorgrades Dr. rer. nat.

vorgelegt von

Sebastian Müller

aus Fürth

FRIEDRICH-ALEXANDER UNIVERSITÄT ERLANGEN-NÜRNBERG
NATURWISSENSCHAFTLICHE FAKULTÄT

ecap ERLANGEN CENTRE FOR ASTROPARTICLE PHYSICS
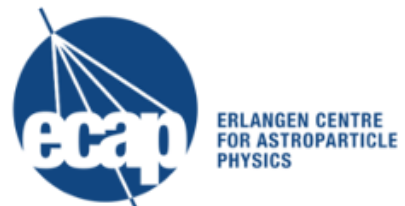
Als Dissertation genehmigt
von der Naturwissenschaftlichen Fakultät
der Friedrich-Alexander-Universität Erlangen-Nürnberg

Zusammenfassung

Akkretierende Röntgenpulsare sind Doppelsternsysteme, die aus einem Neutronenstern und einem optischen Begleitstern bestehen. Mit Dichten ähnlich der von Atomkernen und magnetischen Feldstärken in der Größenordnung von etwa 10^{12} G gehören diese Neutronensterne zu den extremsten Objekten im Universum. Die optischen Begleitsterne der in dieser Arbeit betrachteten Systeme sind sogenannte „Be-Sterne", welche relativ hohe Temperaturen und große Massen besitzen. Ein Hauptmerkmal eines Be-Sterns ist die in hohem Maße veränderliche, äquatoriale Scheibe, von der Materie auf den Neutronenstern übertragen werden kann. Die Wechselwirkungen zwischen dem akkretierten Material und dem Magnetfeld führen zur Bildung von Akkretionssäulen an den magnetischen Polen des Neutronensterns. Die dabei entstehenden Akkretionshügel am Fuß der Akkretionssäulen emittieren thermische Strahlung, die wiederum mit dem einfallenden Material wechselwirken. Diese Wechselwirkungen, sowie Bremsstrahlungsprozesse innerhalb der Akkretionssäulen, führen zur Emission von Röntgenstrahlung, was zum Auftreten der hellsten Quellen dieser Strahlung am Himmel führen kann.

Die Magnetfeldstärken in der näheren Umgebung von Neutronensternen übersteigen die von Menschen technisch realisierbaren Felstärken um viele Größenordnungen. Aus diesem Grund bieten Röntgenpulsare die einzigartige Möglichkeit, die Physik von Materie, die solch starken Magnetfeldern ausgesetzt ist, zu studieren. So sagt etwa die Theorie eine Quantisierung der Bewegung der Elektronen senkrecht zu den Magnetfeldlinien voraus. Die entsprechenden Übergänge liegen, bei den vorliegenden Magnetfeldstärken energetisch im Bereich der Röntgenstrahlung, was bei einigen Röntgenpulsaren in Absorption erscheinende Spektrallinien zur Folge hat. Diese Linien werden auch Zyklotronlinien genannt. Die beobachtete Abhängigkeit der Zentralenergie dieser Linien von der Röntgenleuchtkraft erlaubt es, Rückschlüsse über die Emissionsregionen und somit auch über die physikalischen Prozesse innerhalb der Akkretionssäulen zu ziehen. Aus theoretischen Modellierungen dieser Säulen geht hervor, dass es unterschiedliche Leuchtkraftbereiche mit unterschiedlichen Vorhersagen für die Variation der Energie der Zyklotronlinien gibt. So sollte für relativ niedrige Leuchtkräfte eine positive Korrelation zwischen dem Röntgenfluss und der Linienenergie auftreten, während für hohe Leuchtkräfte eine negative Korrelation dieser Größen erwartet wird.

Eines der Hauptprobleme im Zusammenhang mit der Analyse von Röntgenspektren akkretierender Pulsare ist die Modellierung des Breitbandkontinuums. Vor allem die kaum verstandene Geometrie, aber auch die komplexen physikalischen Prozesse innerhalb der Akkretionssäulen machen die Modellierung sehr anspruchsvoll und zeitaufwendig. Folglich sind Modellspektren von Röntgenpulsaren, die auf physikalischen Grundlagen basieren, noch in der Entwicklungsphase. Stattdessen wird bei den meisten Analysen auf empirische Breitbandmodelle zurückgegriffen.

In dieser Arbeit beschreibe ich Beobachtungen der drei Röntgenpulsare XTE J1946+274, 4U 0115+634 und GX 304−1 mit verschiedenen Röntgenteleskopen und erörtere deren wissenschaftliche Analyse und Interpretation.

Für das System XTE J1946+274 wurde 2001 die Entdeckung und Identifizierung einer Zyklotronlinie veröffentlicht (Heindl et al., 2001). Meine Analyse von *RXTE*-, *INTEGRAL*- und *Swift*-Daten zweier neuerer Ausbrüche dieser Quelle zeigt, dass diese Linie bei der damals bestimmten Energie nicht mehr vorhanden ist. Ferner finde ich schwache Hinweise darauf, dass die Linie sich stattdessen bei signifikant

niedrigeren Energien befindet. Typische Variabilitäten, hervorgerufen durch Änderungen des Röntgenflusses, können eine derart starke Änderung der Linienenergie nicht erklären. Dies würde bedeuten, dass XTE J1946+274 für verschiedene Ausbrüche unterschiedlichen Ausbruchsmechanismen unterliegt.

Mit fünf bestätigten Zyklotronlinien spielt 4U 0115+634, mit der höchsten Anzahl gesicherter Linien, eine herausragende Rolle unter allen Röntgenpulsaren. Praktisch alle bisherigen Analysen dieser Quelle resultierten in einer negativen Korrelation zwischen dem Röntgenfluss und der Energie der fundamentalen Zyklotronlinie. In dieser Arbeit kann ich dieses Ergebnis unter Verwendung empirischer spektraler Standardmodelle reproduzieren. Jedoch finde ich heraus, dass dieses Verhalten auf ein unphysikalisches Zusammenspiel zwischen den Kontinuums- und den Zyklotronparametern zurückzuführen ist. Bei Anwendung eines alternativen Kontinuummodels auf den gleichen Datensatz verschwindet diese negative Korrelation und die Fundamentallinie zeigt keine erkennbare Variabilität der Energie für alle beobachteten Röntgenflüsse. Dieses Ergebnis hat starke Auswirkungen auf die physikalische Interpretation dieses Paradebeispiels eines Röntgenpulsars. Dies ist das erste Mal, dass ein derart starker Einfluss der Wahl des Kontinuumsmodells auf die Parameter der Zyklotronlinie nachgewiesen wird. Ich bin in der Lage, dieses Ergebnis unter Verwendung von *Suzaku*-Daten eines späteren Ausbruchs zu bestätigen.

Bei der Analyse des Systems GX 304–1 zeigt sich ein ungewöhnlich starker Anstieg der Wasserstoff-Säulendichte, die nach etwa drei Tagen wieder auf das ursprüngliche Niveau zurückgegangen ist. Mögliche Szenarien, die diese Beobachtung erklären könnten, werden diskutiert. Eine der vielversprechendsten Erklärungen ist die Bedeckung des Röntgenstrahlung emittierenden Neutronensterns durch die Be-Scheibe des optischen Begleitsterns.

Das Hauptresultat dieser Arbeit ist die Abhängigkeit freier Fitparameter, vor allem der Zyklotronlinien, und deren Verhalten von der Wahl des Kontinuummodells. Im Rahmen dieser Arbeit wird die Stärke und Reichweite solcher Einflüsse verdeutlicht. Aus diesem Grund sind künftig Modelle, die auf physikalischen Prozessen fußen, unabdingbar, um sichere Erkenntnisse über Röntgenpulsare zu erlangen.

Abstract

An accreting X-ray binary pulsar consists of a neutron star and an optical companion star. With densities of the order of atomic nuclei and magnetic field strengths of $\sim 10^{12}$ G, these neutron stars are among the most extreme objects in the universe. The optical companions of the systems treated in this work are so called "Be-type stars". These relatively hot and massive stars host a highly variable circumstellar disk. Triggered by the periastron passage of the neutron star, by the expansion of the Be-disk, and/or by other processes, mass originating from the Be-disk can be transferred onto the neutron star. Interactions between the strong magnetic field and the accreted matter lead to the formation of columns at the magnetic poles of the neutron star. Thermal emission from accretion mounds, which are located at the polar caps of the neutron star, interacts with the infalling matter. These interactions and bremsstrahlung processes within the accretion columns lead to the emission of X-rays resulting in the brightest sources of this radiation in the sky.

Since the magnetic field strengths in the vicinity of neutron stars exceed man-made field strengths by many orders of magnitude, observations of X-rays from these binary systems allow for studying and testing of physical theories for such extreme conditions, e.g., the quantization of the electrons' motion perpendicular to the magnetic field line into discrete Landau levels. In some accreting X-ray pulsars, transitions of electrons at the respective energies imprint absorption features onto the X-ray spectra, the so called "cyclotron resonance scattering features", or short "cyclotron lines". The behavior of the centroid cyclotron line energy depending on the X-ray luminosity allows conclusions about the variation of the X-ray emitting region. These results can be used to draw conclusions about the physical processes within the accretion column. Theory predicts several X-ray luminosity regimes with a different behavior of the cyclotron line, i.e., for relatively low luminosities a positive correlation between the X-ray flux and the cyclotron line energy is expected, while for high luminosities a negative correlation should be observed.

One of the central problems concerning the analysis of X-ray spectra of these outbursts is the modeling of the broadband X-ray continua. The hardly known geometries and the complex physical processes within the accretion columns make it very complicated to physically model the X-ray spectra. As a consequence, model spectra based on a physical description are still under development. Instead, there are several different semi-physical empirical models, which are used in most cases to describe the broadband continuum.

In this thesis I report on X-ray observations of outbursts of the three neutron star binary pulsars XTE J1946+274, 4U 0115+634, and GX 304−1 with different telescopes and discuss the respective analyses and the resulting conclusions.

For XTE J1946+274 a cyclotron line was detected in 2001 (Heindl et al., 2001). My spectral analysis of simultaneous *RXTE*, *INTEGRAL*, and *Swift* observations, using standard phenomenological models to describe the broadband X-ray continuum, reveals the absence of this feature at the respective energy during two outbursts of a recent outburst series. I find weak evidence for this feature to occur at a much lower energy, which cannot be explained by typical variations caused by flux changes. This result indicates that the outburst mechanism of XTE J1946+274 probably varies between different outbursts.

With five confirmed cyclotron lines, 4U 0115+634 plays a decisive role among X-ray binary pulsars. For these systems, this is the highest number of detected cy-

clotron lines. Virtually all previous analyses of this source showed a negative correlation between the centroid energy of the fundamental cyclotron line and the X-ray flux. In this work I reproduce this result using joint observations of the X-ray observatories *RXTE* and *INTEGRAL*. However, I find that this result is caused by an unphysical interplay between the continuum parameters and the cyclotron line parameters. Applying an alternative continuum model to the same dataset, the cyclotron line energy shows no detectable variation for all observed luminosities, coming along with strong impacts on the physical interpretations for this source. This is the first time that such a strong dependence of spectral features on the choice of the empirical continuum model has been proven. I confirm this result using *Suzaku* observations of a subsequent outburst of 4U 0115+634.

The analysis of *RXTE* observations of an outburst of GX 304−1 revealed an extraordinarily strong increase of the equivalent hydrogen column density by a factor of about four. After about three days, the column density declined to the initial value. Several possible scenarios explaining this result are discussed. One of the most promising scenarios is the occultation of the X-ray emitting neutron star by the Be-disk of the optical companion star.

The main conclusion of this work is the previously unknown dependance of free fit parameters, in particular the cyclotron line parameters and their behavior, on the choice of the continuum model. The strong influence on the fundamental cyclotron line's parameters of 4U 0115+634 clearly demonstrates this problem and shows how strong this impact can be. Physical models joining the broadband continuum and the cyclotron lines are under development and have a great potential to improve the situation, even more when using high quality spectra of forthcoming missions like *NuStar*.

Contents

CONTENTS

Chapter 1

Introduction

"WHY are we interested in the boulders forming the rings of Saturn? Why do we want to know the temperature of stars, which are light years away from us? What is the advantage if we know how many black holes are lurking somewhere in the universe? And why do we spend money for these things?" Sure, these questions asked by a lady who attended a guided observatory tour in Bamberg, are justified. Indeed, at first glance, the science of the physical processes happening in deep space does not provide us with many practical applications. Anyway, the declared objective of astrophysicists is different. From thousands of years ago, when our forefathers and mothers started to observe the sky and tried to understand the nature and movements of the celestial bodies, till this day, the driving force for astronomers and physicists has not changed: curiosity. It is human nature to ask about things we do not understand. Of course, many enigmas of the universe have been solved by now, however, we are far away from understanding everything. This lack of knowledge is the reason for scientists to continue questioning and making large efforts to get a better view behind the scenes of the world we live in. As a recent example, with the "Large Hadron Collider"[1] (LHC) in Geneva, physicists use a giant particle accelerator to search for the Higgs boson, which might be responsible for one of the most fundamental quantities: the mass. Other scientists point huge telescopes to the faintest stars and try to find extrasolar planets similar to our Earth, and might at some time be able to give an answer to the question, whether there is life beyond Earth. Even without a direct financial gain, nobody can seriously deny being interested in this kind of important question.

In addition to these fundamental questions, one should keep in mind that, without science, our world would look extremely different and backward. Developments like modern transportations, computer technologies, new materials, etc., would not have been possible without science. Even astronomy, a field of fundamental research, contributes to these practical advances: in the beginning, light sensitive Charge-Coupled Device (CCD) chips were used in astronomy. Today, these CCDs are an every day product and are used in, e.g., modern digital cameras. Furthermore, navigation systems, based on the Global Positioning System (GPS), only became possible with the help of Einstein's General Theory of Relativity, which has been verified by the observations of astronomers.

Compared with other branches of physics, astronomy and astrophysics have a basic disadvantage: they are generally purely observational sciences. While scientists

---

[1]http://lhc.web.cern.ch/lhc/

working in, e.g., particle physics, quantum optics, or solid state physics mostly make use of laboratories with special experimental setups, which can be tailored exactly to their questions, in astrophysics, scientists can only use data obtained from systems, which are outside of influence. However, the big advantage in astronomy is the occurrence of extreme physical conditions in many of the systems we study. "Laboratories" like the surroundings of black holes exhibit the strongest gravitational forces in the universe. Neutron stars, which are a basic part of this work, and magnetars show magnetic field strengths which are many magnitudes larger than the strongest man-made magnetic fields on Earth. Astronomy and astrophysics allow us to study the behavior of matter under these extraordinarily violent conditions.

Especially the relatively young field of X-ray astronomy is able to give us insight into, among many other astrophysical fields of research, processes in the vicinity of these extreme objects like neutron stars and black holes. The work I present in this thesis is related to the X-rays emitted by systems which consist of a neutron star orbiting a companion star. Transfer of matter from the optical companion star onto the neutron star leads to violent X-ray outbursts. The respective X-ray sources in the sky allow us to study the physics of material encountering extremely high magnetic field strengths.

1.1 Properties and Evolution of Stars

Q UANTITATIVELY, stars can be defined as massive, self-luminous plasma balls in the universe, which are in hydrostatic equilibrium. In this Section, I give an overview of the physical properties of stars. Furthermore, the evolution of stars, from their birth to their death as well as their remnants are described. Finally, I give a brief introduction on the classifications and orbits of binary stars. This Section is based on the text books Kippenhahn & Weigert (1990), Unsöld & Baschek (2001), Carroll & Ostlie (2007), and Karttunen et al. (2007).

1.1.1 Spectral Classification and the Hertzsprung-Russell Diagram

To be able to classify stars, physical quantities which describe these objects are required. One of these quantities is the logarithmically scaled absolute luminosity M. Another one is the effective temperature T_{eff}, which is defined as the temperature of an ideal black body emitting the same flux density as the respective star.

One of the most common classifications is the Harvard classification (see, e.g., Unsöld & Baschek, 2001). The respective sequence (with the relatively famous memory hook "Oh, Be A Fine Girl/Guy, Kiss Me!") is

$$\mathrm{O} \xleftrightarrow{0...9} \mathrm{B} \xleftrightarrow{0...9} \mathrm{A} \xleftrightarrow{0...9} \mathrm{F} \xleftrightarrow{0...9} \mathrm{G} \xleftrightarrow{0...9} \mathrm{K} \xleftrightarrow{0...9} \mathrm{M}.$$

The main property of the Harvard sequence is the effective temperature. Spectral lines which strongly depend on T_{eff} are used to define the Harvard classes. While O stars are very hot and blue stars with a typical effective temperature of $\sim 200\,000\,\mathrm{K}$, M stars are cool and red stars with $T_{\mathrm{eff}} \approx 3600\,\mathrm{K}$. Furthermore, there are subclasses between these spectral types, which are indicated by the numbers 0–9.

One of the most important diagrams in astronomy is the "Hertzsprung-Russell Diagram" (HRD), which displays the position of stars regarding the Harvard type in x-, and the absolute magnitude in y-direction. Alternatively, the x-axis often shows the
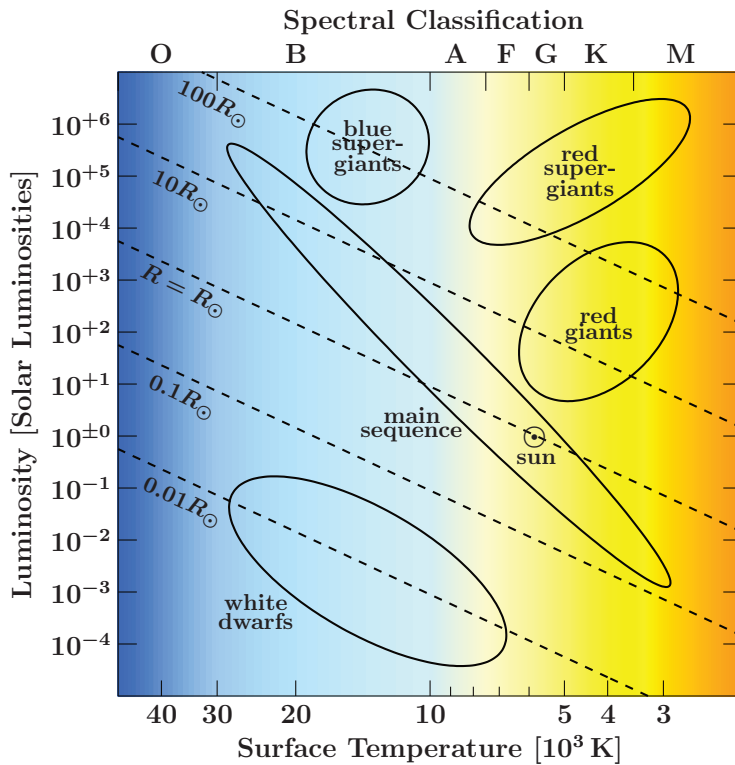
Figure 1.1: Sketch of the Hertzsprung-Russell Diagram. The color gradient indicate the temperature of the star. Typical positions of certain types of stars are marked as well as the position of the sun. Dashed lines correspond to stars with constant stellar radii.

descending effective temperature. Figure 1.1 displays a sketch of the HRD. Dashed lines indicate constant stellar radii.

At first glance, one might expect that stars are distributed uniformly in the HRD, however, there are certain regions, where the stars are clustering (see the marked regions in Fig. 1.1). The majority of stars is located along a diagonal curve, the so called main sequence (MS). However, there are other positions, where stars are clustering, e.g., several regions with different types of giant stars or with white dwarfs. The HRD is a very useful tool to describe and to study stellar evolution. There are typical tracks in the HRD which describe the evolutionary paths of stars. These tracks depend on the initial masses of the stars (see Sect. 1.1.2).

1.1.2 Evolution of Single Stars

Stars are born within collapsing gas clouds, whose masses are high enough to overcome the gas pressure. The collapse of a gas cloud can only start, if its mass is larger than the so called Jeans mass $M_J \approx 3 \times 10^4 (T^3/n)^{1/2} M_\odot$, where T denotes the temperature in K and n the density in atoms m^{-3} (e.g., Carroll & Ostlie, 2007). Typical values of M_J are generally much higher than the masses for single stars. Thus, stars are not born alone, but are formed within interstellar clouds in groups of a few hundred stars in loose associations, i.e., open clusters. For a detailed paper about the formation of proto stars see, e.g., Shu et al. (1987).

When a star ignites core hydrogen burning, it starts its life at the MS in the HRD. Basically, there are two hydrogen-to-helium-burning processes, i.e., the proton-proton (pp) chain and the Bethe-Weizsäcker (CNO) cycle. Both processes lead to the exothermic fusion of H nuclei forming He. While for cooler stars the pp chain is the dominant fusion process, for relatively hot stars the CNO cycle becomes important. These two processes have different energy generation rates. As a consequence, massive stars

burn up their Hydrogen much faster than less massive stars. Stars which are similar to our sun remain several billions of years on the MS. In contrast, stars with much higher masses finish this stage after a few hundred millions of years, or even less. The processes, after a star has finished its MS phase, strongly depend on the mass of the star and are described in the following (based on Kippenhahn & Weigert, 1990, Carroll & Ostlie, 2007 and Maeder, 2009).

1.1.2.1 Sun-like Stars ($0.26\,M_\odot \lesssim M \lesssim 1.5\,M_\odot$)

After leaving the MS, a star with a mass which is similar to the solar mass starts a phase of hydrogen shell burning, leading to an increase of the stellar radius. In the HRD, the star leaves the MS towards the region with lower temperatures and higher luminosities, the so-called red giant branch. The helium core of this star contracts, leading to an increase of the temperature of the central matter. This process leads to a degeneration of the helium core, meaning that neither the density nor the pressure in the core depends on the temperature. If T reaches a certain value, the helium in the core ignites which leads to an even higher temperature in the core. Since the efficiency of the helium burning increases with increasing temperature, the core ends up in a vicious circle, i.e., the so called "helium flash". However, if the core exceeds a certain temperature, the degeneration of the core matter is cancelled. The core can expand and cool down. A phase of stationary helium burning, where the star is located at the horizontal branch in the HRD, starts until the helium is depleted. After this phase, nuclear fusion within another shell begins, which results in a further expansion of the star. During this phase with two burning shells, the star is located on the asymptotic giant branch in the HRD and ejects its outer gas layers and produces a planetary nebula. Since no other nuclear fusion process can start after this phase, the remaining gas ball contracts and ends its life as a white dwarf.

1.1.2.2 Massive Stars ($2.5\,M_\odot \lesssim M \lesssim 8\,M_\odot$)

After the hydogen fusion, a star with a higher mass starts the helium burning in its core under non-degenerated conditions. As a consequence, this stars does not undergo a helium flash. The helium fusion happens on the so called helium MS in the HRD. After this phase, carbon burning starts under degenerated conditions within the core, which leads to a carbon flash. This flash probably leads to the supernova explosion of the star. However, it is still not clear, how massive a star has to be to undergo a supernova explosion.

1.1.2.3 Supermassive Stars ($M \gtrsim 8\,M_\odot$)

For supermassive stars, the carbon core burning starts even before a degeneration of the core matter is possible. This produces various elements like O, Ne, Na, Mg, etc. Depending on the mass of this star, subsequent burning processes of these elements lead to an onion-like structure of the stellar interior. Eventually, in the star's innermost, silicon burning leads very rapidly (within a few days) to the production of the most massive chemical element which can be produced exothermally by nuclear fusion: iron. Due to the extremely high density and temperature within the iron core, the material undergoes a process which is called *photodisintegration*, i.e., Fe is stripped down to protons and neutrons by high energy photons. Inverse β-decay,

$$p + e^- \longrightarrow n + \nu_e, \tag{1.1}$$

leads to a drastic increase of the neutrino luminosity of the star during the silicon burning process. Since the electrons within the iron core cannot provide a stabilizing pressure, the core starts to collapse extremely rapidly. The speed of the collapsing material is proportional to the distance to the center, which leads to a decoupling of the inner core and the region outside, where the speed exceeds the local sound speed, and where the material collapses with nearly free-fall velocity. The inner core collapse proceeds until densities about three times larger than the nuclear density are reached. Under this condition, from Pauli's exclusion principle for neutrons follows that the strong force suddenly changes from being attractive towards being repulsive. As a consequence, the inner core stops its collapse and a bounce leads to pressure waves moving outwards into the still collapsing outer core. However, this shock is strongly damped when moving outwards. Neutrinos emitted in the central region provide the "missing" energy to ignite a *supernova explosion* of Type II. During this explosion, the *r-process* leads to the production of elements which are more massive than Fe. The increased neutron flux causes capture processes as

$$\text{}^{A}_{Z}\text{X} + n \longrightarrow \text{}^{A+1}_{Z}\text{X} + \gamma, \tag{1.2}$$

where A is the mass number and Z the proton number of an element X. Subsequently, β-decay can follow as

$$\text{}^{A+1}_{Z}\text{X} \longrightarrow \text{}^{A+1}_{Z+1}\text{X} + e^{-} + \bar{\nu}_{e} + \gamma. \tag{1.3}$$
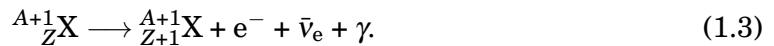
The *r*-process is characterized by a shorter β-decay time compared to the time scale of the neutron capture and mainly produces elements with $A{>}60$. Note that the other case, where the neutron capture time scale exceeds the half-life of the β-decay, the following reaction is called the *s-process*, which can occur in the nuclei burning phases of stellar evolution (for a detailed review on the synthesis of elements in stars, see, e.g., Burbidge et al., 1957).

After the supernova explosion, the core ends up as a compact object like a neutron star or a black hole (see Sect. 1.2).

1.1.3 Be-Stars

A class of stars, which is important for this work, is the class of Be-objects. A review of these objects, on which this Section is based, is given by Porter & Rivinius (2003). These stars are defined as non-super-giant B stars with one or more Balmer lines in emission, which can be absent every now and then (Collins, 1987). Their optical spectra are characterized by typically double peaked emission lines (Struve, 1931), mostly from HI, HeI, and FeI (Porter & Rivinius, 2003). These lines originate from a circumstellar disk in the equatorial plane of the Be-star.

Since evolutionary scenarios, like these described in the previous Sections, cannot explain the existence of Be-stars, there is a controversy about the real origin of these stars. There are scenarios which assume that the stellar evolution of Be-type objects is separated from the evolution of B stars (Porter & Rivinius, 2003, and references cited therein). Other theories imply these these kinds of objects are an evolutionary stage of B stars (e.g., Mermilliod, 1982; Zorec & Briot, 1997; Fabregat & Torrejón, 2000).

Another mystery of Be-stars is the formation process of the circumstellar disk. Although Be-stars are very fast rotators with an angular speed which is close to the breakup velocity (e.g., Chauville et al., 2001; Townsend et al., 2004), rotation alone cannot explain the formation of the Be-disks. Rotation in combination with

non-radial pulsations, however, possibly provides an explanation for the formation of these disks (Frémat et al., 2006, and references cited therein). Typically, the ratio of the disk's and the stellar radius is ∼4.4 (Touhami et al., 2013), however, the disk can even exceed radii of more than 50 stellar radii (see, e.g., Slettebak, 1988, Štefl, 1999, or Porter & Rivinius, 2003, for reviews).

1.2 Stellar Remnants

P RODUCING a planetary nebula or exploding as a supernova does not imply that the matter of a star is ejected completely into interstellar space. After a star's death, there rather remains a stellar corpse, i.e., a white dwarf, a neutron star, or a black hole. The nature of the stellar remnant depends on its mass. In this Section, the nature of these objects is explained.

1.2.1 White Dwarfs

A White dwarf is the (semi) final state in stellar evolution for a star with $M \lesssim 9 M_\odot$ (Kepler et al., 2007), i.e., for the majority of stars. These objects are hot and dense gas balls with radii comparable to the radius of the Earth. A white dwarf is an onion-like structured object and consists of carbon and oxygen core, which is enclosed by a layer of helium. On the surface, there is a very thin hydrogen dominated atmosphere. A white dwarf is stabilized by a *Fermi-Dirac degenerated* electron gas, i.e., all energy levels up to a certain energy are occupied by two electrons which have, according to the Pauli exclusion principle, reverse spins (e.g., Unsöld & Baschek, 2001; Carroll & Ostlie, 2007). Fermi-Dirac statistic leads to a mass-radius relation for white dwarfs as

$$R \propto M^{-1/3}, \tag{1.4}$$

i.e., the radius of a white dwarf decreases with an increasing mass. Note that the pressure of the electrons in a white dwarf does not depend on the temperature. For dense white dwarfs, relativistic effects have to be taken into account, which leads to the constraint that white dwarfs can only exist for masses $M \lesssim 1.4 M_\odot$ (*Chandrasekhar limit*, Chandrasekhar, 1931). For higher masses, the radius of a white dwarf would behave as $R \to 0$. The fate of remnants with masses larger than the Chandrasekhar limit is discussed in Sects. 1.2.2 and 1.2.3. Looking at the measured mass distribution for white dwarfs obtained by the Palomar Green Survey (Green et al., 1986), Liebert et al. (2005) found that 75% of these stars have masses of about $0.6 M_\odot$, 15% above ∼$0.8 M_\odot$, and 10% have lower masses of about $0.4 M_\odot$. While the majority of white dwarfs which is characterized by $M \approx 0.6 M_\odot$ has evolved from planetary nebula ejection of single stars, Liebert et al. (2005) concluded that the low mass white dwarfs are generated via binary evolution. In contrast to this, Liebert et al. (2005) concluded that the high mass white dwarfs are produced via different channels, e.g., stellar merging processes.

From a spectroscopic point of view, white dwarfs can be basically separated into two groups. The most common spectral type of white dwarfs is called DA. This kind of white dwarf is characterized by a hydrogen enriched atmosphere and shows strongly broadened Balmer lines. The spectra of type DB white dwarfs are characterized by very broad Helium lines. In addition to these spectral types, there are more exotic white dwarfs, e.g., the DC white dwarfs, which exhibit no line features in their optical

spectra. This kind of white dwarf is sometimes used to correct for a wavelength dependent effective area of optical spectrographs.

In the course of time, white dwarfs will cool down and end up as black dwarfs. However, the time scale of this cooling process exceeds the age of the universe and black dwarfs are therefore hypothetical objects.

1.2.2 Neutron Stars

As described in Sect. 1.2.1, white dwarfs are only stable for masses $M \lesssim 1.4 \, M_\odot$. What is the fate of stellar remnants with masses which are larger than this limit? Supernova explosions of stars with $M \gtrsim 9 \, M_\odot$ are characterized by extremely high densities within the core, leading to an inverse β-decay of the matter (see Sect. 1.1.2.3). If the remaining mass is less than the *Oppenheimer-Volkoff limit* ($M \approx 3 \, M_\odot$), the resulting corpse has a radius of about $10 \, \text{km}$ and a density of $\rho \sim 10^{14} \, \text{g cm}^{-3}$, which is comparable to the density of heavy atomic nuclei ($\rho_0 = 2.8 \times 10^{14} \, \text{g cm}^{-3}$, Haensel et al., 2007). These objects are called *neutron stars*.

1.2.2.1 The Structure of Neutron Stars

Neutron stars exhibit a complex and in many aspects not well understood structure. Since the condition of the matter in neutron stars cannot be studied in terrestrial laboratories directly, we have to rely on theoretical descriptions including Quantum Chromo Dynamics (QCD), super-fluidity, etc. The resulting structure is discussed in the following (based on Haensel et al., 2007).

- **the atmosphere:** the thin, outermost layer at the surface of a neutron star consists of plasma. The thickness of this layer can be less than a few millimeters. The thermal radiation emitted from this layer can be used to gain information about the parameters of the atmosphere, e.g., effective temperature, gravity, chemical composition, and the configuration of the magnetic field. Furthermore, fundamental parameters like mass and radius of the neutron star can be determined studying this radiation.

- **the outer crust:** a largely solid layer with a thickness of about 200–500 m. The bottom of this layer is characterized by a density of about $4 \times 10^{11} \, \text{g cm}^{-3}$. It consists mainly of ions and electrons, which provide the pressure within this layer. At the higher densities at the bottom of this layer, inverse β-decay enriches the nuclei with neutrons. These neutrons can detach from the nuclei, which is called the "neutron drip", and produce a free neutron gas.

- **the inner crust:** in this layer with a thickness of about one kilometer, the density ranges from $4 \times 10^{11} \, \text{g cm}^{-3}$ to $\sim \frac{1}{2}\rho_0$ at the bottom. The matter in this layer is a mixture of atomic nuclei, free electrons, and neutrons. The free neutrons might be in a super-fluid state. At the bottom of this layer, nuclei cannot exist any more.

- **the outer core:** the density varies between $\frac{1}{2}\rho_0$ and $2\rho_0$. The thickness of the outer core is of the order of several kilometers. It consists of a degenerated neutron plasma with protons, electrons, and possibly muons. While the electrons and muons form an almost ideal Fermi gas, neutrons and protons are possibly in the state of a super-fluid Fermi liquid. For neutron stars with comparably low masses, this layer even extends to the center of the neutron star.
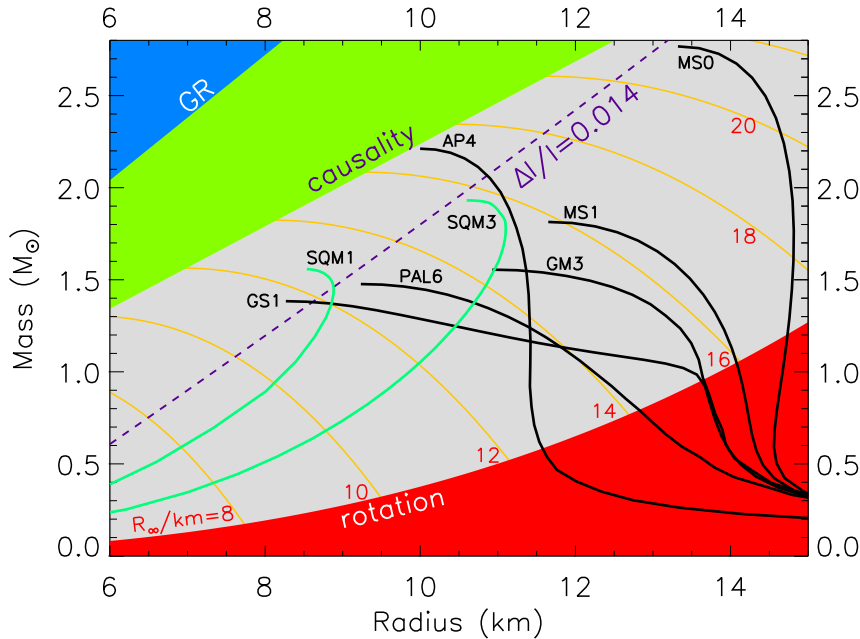
Figure 1.2: Mass-radius relation for neutron stars (adopted from Lattimer & Prakash, 2004). See text for details.

- **the inner core:** in the central region of neutron stars, the density can exceed values of of $10\rho_0$. This region has a radius up to several kilometers. The structure of the matter in the core leaves an open question and depends strongly on the theoretical model. In addition to the prediction of the hyperonization of the matter, there are more exotic models like pion or kaon condensation, or even the occurrence of quark matter.

1.2.2.2 Mass-Radius Relation of Neutron Stars

Since the structure of neutron stars is complex and by far not understood, deriving a well-defined mass-radius relation like for white dwarf stars (Eq. 1.4) is not possible. The numerous different models, which describe neutron stars, lead to different equations of state. However, some regions in the mass-radius diagram can be excluded a priori (Fig. 1.2). According to Lattimer & Prakash (2004), the blue region of Fig. 1.2 can be excluded by the Schwarzschild condition, $R \leq 2GM/c^2$. The green region can be excluded by the principle of causality, $R \lesssim 3GM/c^2$, i.e., the speed of sound has to be less than the speed of light (e.g., Glendenning, 1992). The red region can be excluded by rotational constraints, i.e., the rotational velocity on the surface has to be less than the speed of a hypothetical particle which orbits the neutron star at a distance equally to the stellar radius. Orange lines indicate radii of constant radiation, defined as

$$R_\infty := \frac{R}{\sqrt{1 - 2GM/(Rc^2)}}. \tag{1.5}$$

The dashed purple line indicates a radius limit which was estimated with glitches of the Vela pulsar (Lattimer & Prakash, 2001). The black and green curves correspond to equations of state for different models (for the definitions of the labels, see Lattimer & Prakash, 2001). Because these solutions are located within a wide range in the mass-radius diagram, precise measurements of the radius and the mass of neutron stars are required to test these models. This is, however, only possible when doing many different, more or less safe, assumptions, which challenges observers until today (e.g., Özel, 2006; Sala et al., 2012).

1.2.2.3 Magnetic Fields and Rotation of Neutron Stars

Assuming that the angular momentum and the magnetic flux are conserved when a star evolves towards a neutron star, these quantities can be expressed as

$$
\left.\begin{array}{c} \omega_{\mathrm{f}} \\ B_{\mathrm{f}} \end{array}\right\} = \left(\frac{R_{\mathrm{i}}}{R_{\mathrm{f}}}\right)^2 \times \left\{\begin{array}{c} \omega_{\mathrm{i}} \\ B_{\mathrm{i}} \end{array}\right., \tag{1.6}
$$

where ω denotes the angular frequency and B the magnetic field strength. The indices "i" and "f" indicate the initial (with respect to the progenitor star) and final (with respect to the neutron star) states, respectively. These simple equations lead to the result that neutron stars rotate very fast after their formation, even with rotational periods of the order of milliseconds. Following Carroll & Ostlie (2007) and using typical values for the pulse period of white dwarfs, Eq. 1.6 yields that neutron stars rotate with periods of the order of a few 10^{-3} s right after their formation. Furthermore, Carroll & Ostlie (2007) showed, if using the largest observed value for magnetic field strengths for white dwarfs, that the B-field of neutron stars results in 1.3×10^{14} G.

1.2.2.4 Pulsars

Bell & Hewish (1967) report on the discovery of a source of periodical radio pulses, which originate from the constellation Vulpecula. Today, this source is known as the object PSR B1919+21. To date, more than 1500 of these sources with pulses, mostly between $\sim 10^{-3}$ s and 10 s, have been detected (Manchester et al., 2005, and the respective web interface at `http://www.atnf.csiro.au/research/pulsar/psrcat`). Rotating neutron stars which interact with matter in their surroundings provide a possible explanation of these sources. If the magnetic field of a neutron star is tilted with respect to its rotational axis, charged particles in the surrounding of the neutron star are tied to the magnetic field and are forced to follow this rotation. Particles at a certain region, where the rotation gets close to the speed of light, emit synchrotron radiation in a narrow cone. Due to the neutron star's rotation, this cone acts like a lighthouse beam, thus explaining the pulsated radiation observed on Earth. The steady emission of electromagnetic radiation indicates a decrease of angular momentum of the neutron star or, in other words, a decrease of the pulse period. And indeed, for example, the Crab pulsar shows a spin down rate of $\dot{P} = 4.21 \times 10^{-13}$ s s^{-1} (Carroll & Ostlie, 2007). In addition to this permanent spin down, there are sometimes sudden jumps in the pulse period ephemeris visible, the so called "glitches" (e.g., the Vela pulsar, McCulloch et al., 1987). These glitches could be caused either by crust quakes (e.g., Ruderman, 1991), or by the transfer of angular momentum between certain layers of the neutron stars (e.g. Anderson & Itoh, 1975).

In addition to radio pulsars, neutron stars which pulsate in the X-rays are known. This type of neutron stars is the main topic of this thesis and is extensively discussed in Sect. 2.

1.2.3 Black Holes

In addition to white dwarfs and neutron stars, there is a third possibility for stars to finish their lives. As already mentioned in the previous Section, there is an upper limit for the mass of neutron stars, i.e., the Oppenheimer-Volkoff limit $M_{\mathrm{OV}} \approx 3\,M_\odot$. If the mass of a stellar remnant exceeds this limit, there is no stable state of the

matter known and the gravitational force dominates all other forces. This object collapses to a *black hole*.

For black holes, the *escape velocity* v_e, i.e., the velocity required to break free from the gravitational field, can be calculated with the use of the fact that the sum of kinetic and potential energy has to be zero in this case. The distance between the black hole and an object, for which v_e becomes c, is defined as the *Schwarzschild radius* R_S of the black hole. From classical mechanics as well as from the general theory of relativity follow that

$$R_S = \frac{2GM}{c^2}. \tag{1.7}$$

This radius is called the *event horizon*, from where no information can escape outwards.

In contrast to the popular belief that black holes are malicious monsters, which lurk in the deep space and guzzle other stars, planets, or even poor astronauts, black holes are rather quite simple objects. The *no hair theorem* (Carter, 1971) implies that black holes are characterized by only three parameters: mass, angular momentum, and charge. However, these parameters cannot be measured directly. One way is to analyze the orbital motion of the companion star, as described in Sect. 1.3, and draw conclusions about the mass of the unseen black hole (e.g., PG 1232−136, Müller, 2009). Another process providing us with information is accretion of mass from the companion star into the black hole. The emitted radiation, mainly X-rays, can be used to study the surroundings of black holes. For a detailed discussion of this topic and especially Cyg X-1, see, Hanke (2011). For example, spectral emission features are "deformed" by gravitational red-shift effects, allowing to study the spin of the black hole (see, e.g., Dauser, 2010).

In addition to stellar mass black holes, there are super-massive black holes with masses of $10^6 - 10^{10}\,M_\odot$ in the center of galaxies. In the case of accretion, these objects result in the brightest luminosities in the universe and are called *Active Galactic Nuclei* (AGNs). The origin of super-massive black holes, however, differs from the origin of stellar mass black holes and remains an open question. For a detailed multi-wavelength study of these objects, see, e.g., Böck (2012).

1.3 Binary Stars

S OMETIMES stars appear quite close to each other in the sky. Binary stars, with by a telescope resolvable components, are called *optical binary stars*. However, this does not necessarily mean that the distance between these stars is very short, but is in many cases caused by a projection effect. These pairs, which are not gravitationally bound and are located along the same line of sight, are called "optical doubles". An example for this kind of binary is the "Horse and Rider", or, in other words, the two stars Mizar (ζ UMa) and Alcor (80 UMa). This binary can, even without a telescope, be separated and is a famous test of eyesight.

In contrast to the sun, many stars spend their lives with one or more gravitationally bound companion stars. It has been shown that more than 50% of the stars in the milky way are a part of binary systems (e.g., Li & Han, 2008, and references cited therein). The classification of binary stars is based on the respective discovery method (based on Hilditch, 2001):

- **Visual binaries:** These binary stars can be resolved as two separate stars. For
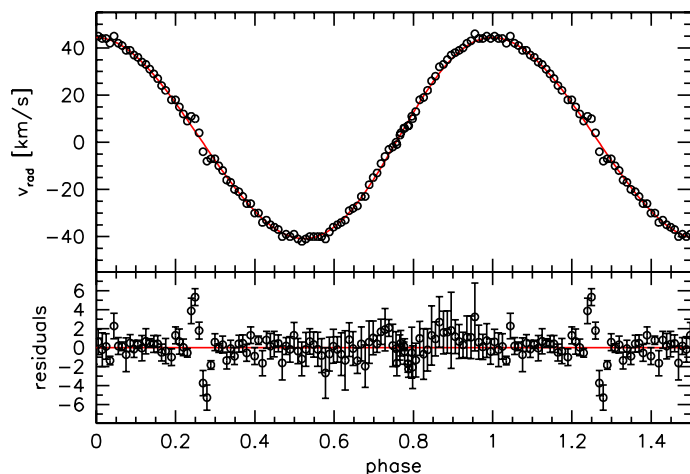
Figure 1.3: Radial velocity curve of a spectroscopic binary (AA Dor, Müller et al., 2010a). The upper panel shows the radial velocity $v_{\rm rad}$ versus the orbital phase (phase = 1, where $v_{\rm rad}$ is at maximum). The lower panel displays the residuals of a the best orbit fit when using a (almost) sinusoidal function. The wiggles at phase ~ 0.25 are caused by occultation effects, i.e., the Rossitter-McLaughlin effect.

some systems, the movement of visual binary stars can be observed directly. Using this orbital information together with the distance to the system, allows for the calculation of the separation of the binary components. The probably most prominent example for a visual binary is Albireo (β Cyg, e.g., ten Brummelaar et al., 2000).

- **Astrometric binaries:** In this type of binaries, only one component is visible. This could be caused by a relatively large difference between the brightness of the two components. The proper motion of the visible star can be used to draw conclusions about its companion. A famous example for an astrometric binary star is Procyon (α CMi, e.g., Liebert et al., 2013).

- **Spectroscopic binaries:** The identification of spectroscopic binaries happens via optical spectra showing periodically Doppler shifted emission or absorption features. Binaries with moving lines from one component are called single lined binaries. However, there are systems where inverse moving spectral lines from both stars are visible. These systems are called double lined binaries, respectively. A radial velocity curve of the spectroscopic binary AA Dor is shown in Fig. 1.3 (Müller et al., 2010a).

- **Photometric binaries:** Light curves with periodical dips, caused by occultations, are used to identify these binaries. This effect can occur, if the angle between the line of sight and the orbital plane of the binary is small enough. Practically, this method, together with the precise measurements of radial velocities, provides a powerful tool for the search of extra solar planets, as, e.g., performed in the Kepler mission (e.g., Kostov et al., 2013). An example for a binary star which was detected recently by its photometric variability is ASAS 102322−3737.0 (Schaffenroth et al., 2013).

Binary stars play an extraordinary role in Astronomy, because under certain conditions, the precise analysis of the orbital motion enable scientists to determine the most important quantity of these stars: their masses. This procedure as well as the orbital parameters of binary stars and the stellar evolution within binary systems are explained in the following Sections.
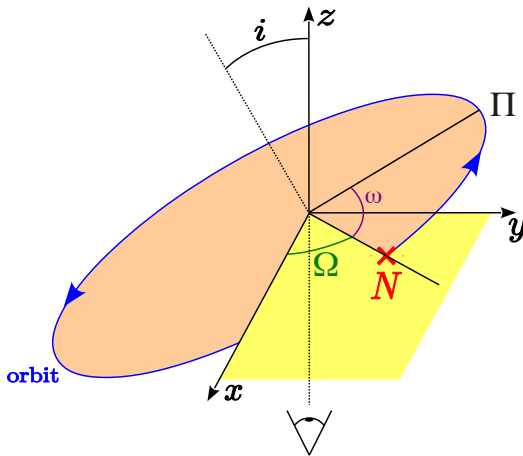
Figure 1.4: Orbital parameters for a relative orbit. The observer looks towards z direction. The x direction points towards the North Celestial pole. The origin of the coordinate system is located at the reference star of the binary system. N, the ascending node is defined as the point where the orbit intersects the tangent plane of the sky (yellow).

1.3.1 Orbits of Binary Stars

Using Newton's law of gravitation and the equations of motion, the orbits of binary stars with masses M_1 and M_2 can be calculated analytically (this calculation as well as a detailed description of the orbits of binaries can be found in Hilditch, 2001, on which this Section is based on). This two body problem yields three solutions, where the orbits are either hyperbolic, parabolic, or, in the case of closed orbits, ellipsoidal. In the latter case, which accounts for binary systems, both binary components follow an ellipsoidal orbit with the center of mass of the system in the focus. This rule is called *Kepler's first law*. Another consequence is that the binary components do not move with a constant velocity. They rather vary from the minimum velocity at the farest point on the ellipse to the center of mass (called apastron) to the maximum velocity at the closest point (periastron Π). This is called the *Kepler's second law*. Figure 1.4 illustrates the definitions of orbital parameters for a relative orbit, i.e., the orbit of the companion star as seen by one binary component. Basically, an orbit and its geometrical orientation with respect to the Earth's direction are characterized by the following quantities:

- the orbital period P, defined as the duration of one orbital cycle,
- the semi-major axis a of the ellipsoidal orbit,
- the eccentricity e, which defines the "squeeze" of the ellipse as $e = \sqrt{1 - (b/a)^2}$ (b: semi-minor axis),
- the inclination i, defined as the angle between the surface normal of the orbital plane and the line of sight,
- the longitude Ω of the ascending node N, as defined in Fig. 1.4,
- the longitude ω of periastron Π, as defined in Fig. 1.4, and
- the time of periastron T_0, where the binary components come closest to each other and reach their maximum velocities.

1.3.2 Determination of Masses in Stellar Binaries

For a review of mass determination for binaries, see, e.g., Geier (2009), and references cited therein. With data as displayed in Fig. 1.3 and the assumption of a circular orbit
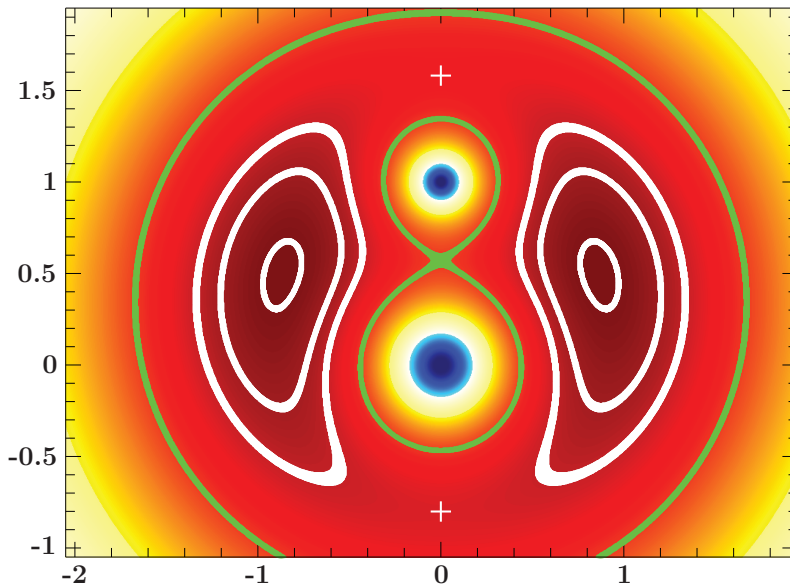
Figure 1.5: Cross section in the x-y-plane of a color coded Roche potential with $M_1/M_2 = \frac{1}{2}$. The white lines correspond to equipotential lines. Crosses show the two Lagrangian points L_2 and L_3. The more massive star is located at the origin of the coordinate system, while M_2 is located at (0,1,0).

($e = 0$), a sinusoidal function as

$$v_{\mathrm{rad}}(t) = \gamma + v_{1,2} \times \sin\left(\frac{2\pi}{P}(t - T_0)\right) \tag{1.8}$$

can be fitted to the radial velocity curve. Here, γ denotes the velocity of the system with respect to the Earth and $v_{1,2}$ the amplitude of the radial velocity of the two components. In contrast to eccentric orbits, for circular orbits, T_0 is defined as the time where $v_{\mathrm{rad}} = \gamma$ and $\dot{v}_{\mathrm{rad}} > 0$. Using the mass function

$$f(m) := \frac{P v_0^3}{2\pi G} = \frac{M_2^3 \sin^3 i}{(M_1 + M_2)^2}, \tag{1.9}$$

and the equation

$$M_1 v_1 = M_2 v_2, \tag{1.10}$$

yield constraints for the masses of the binary components. In many cases, only the radial velocities of one binary component can be achieved from the data. However, sometimes Doppler-shifted features from both component are visible in the spectra. For these rare double lined systems, the resulting velocity amplitude of both binary components can be calculated. The knowledge of the radial velocity amplitudes and and the orbital period allows for the determination of a lower mass limit for both stars, but not for a complete solution of Eqs. 1.8 and 1.9. The masses can be only calculated, when the inclination i of the system is known. For most systems, however, it is not possible to measure the inclination. Nonetheless, systems with relatively high inclinations sometimes show occultations of the binary components in their light curves, which can be used to determine i.

Using the Doppler shift of spectral lines is one possibility to study the orbits of binary systems. Another way to achieve information about the orbital motion is the use of pulsations from a binary component (Hulse & Taylor, 1975).

1.3.3 Evolution of Close Binary Stars

In Sect. 1.1.2 the stellar evolution for single stars has already been discussed. The evolution of binary stars, however, is, due to possible interactions between the binary
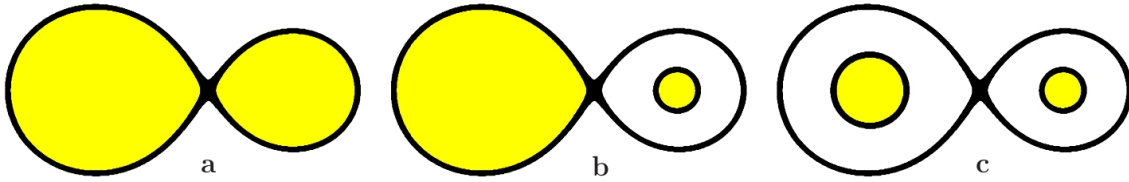
Figure 1.6: The three classes of close binary systems: Contact- (a), semi-detached- (b), and detached binaries (c).

components, much more complicated. These interactions can be explained by the gravitational potential, Φ, of a circularly rotating binary, which consists of the sum of the two point-mass potentials of the stars, and the rotational potential. This so called *Roche-potential* can be written as

$$\Phi = -\frac{GM_1}{r_1} - \frac{GM_2}{r_2} - \frac{\omega^2}{2}\left[\left(x - \frac{M_2}{M_1 + M_2}\right)^2 + y^2\right],\tag{1.11}$$

where $r_1 = \sqrt{x^2 + y^2 + z^2}$, $r_2 = \sqrt{(x-1)^2 + y^2 + z^2}$, and ω is the angular speed of the system. The origin of the respective coordinate system is located in the center of the more massive star M_1, while M_2 is located at a distance 1 from the origin. The vector of angular moment $\vec{J}$ points into z-direction. The resulting equipotential lines of the Roche potential are displayed in Fig. 1.5.

In this configuration, there are five points of equilibrium, i.e., points where the gravitational and centrifugal forces cancel each other. These points are called the *Lagrangian points* L_1–L_5. The saddle point L_1 is located between the two stars and is indicated in Fig. 1.5 by the touching point of the respective equipotential lines, which are plotted in green. These green lines belong to the so called *Roche surface*. The points L_2 and L_3 are located on the conjugation line of the two stars, as indicated by two crosses in Fig. 1.5. The two remaining Lagrangian points, L_4 and L_5, are located in the centers of the drused equipotential lines which are located symmetrically beside the conjugation line of the stars.

The shape and the size of the binary components, with respect to the Roche potential, allow for a further classification of binary stars. If both stars are large enough, they completely fill their Roche surface and are in contact at the inner Lagrangian point L_1 (see Fig. 1.6a). These systems are called *contact systems*. Another class of binary stars, where only one component completely fills up its Roche lobe, is called *semi-detached systems* (see Fig. 1.6b). Mass transfer within systems via L_1 is called *Roche lobe overflow*. Note that in these systems, the less massive star possibly leaves the MS before the more massive star. The reason for this so called *Algol paradox* is transfer of matter from one binary component to the other via L_1, which influences the lifetime of the binary components (see, e.g., Pustylnik, 2005, and references cited therein). If the stars are smaller than their respective Roche lobes, no mass transfer can happen via Roche lobe overflow and the stars evolve largely independent from each other (see Fig. 1.6c). These close binaries are called *detached systems*.

Mass transfer processes within binary systems and thus, the evolution of these stars, strongly depend on the Roche potential of the system. From Eq. 1.11 follows that this potential depends on the masses as well as on the orbital period of the system. Evolutionary scenarios for binaries often predict mass transfer from a core hydrogen burning star onto an evolved object as a white dwarf, a neutron star, or a

black hole resulting in the emission of X-ray radiation (e.g., Tutukov & Yungel'Son, 1993; Podsiadlowski et al., 2003). The explanation of all possible evolutionary scenarios goes far beyond the scope of this thesis. Since neutron star X-ray binaries are the central topic of this thesis, processes within these kind of systems are explained in Sect. 2.1 in more detail.

Chapter 2

Accreting X-ray Pulsars

ACCRETING X-ray binary pulsars occur in binaries where a neutron star orbits an optical companion star in a more or less eccentric orbit. Mass transfer processes from the optical companion onto the neutron star leads to violent X-ray outbursts, which can appear as the brightest X-ray sources in the sky. After the first discovery of such an object in the 1960s (Sco X-1, Giacconi et al., 1962; Gottlieb et al., 1975), until today, more than 220 of these objects have been detected (Liu et al., 2000, 2007).

There are fundamental differences between X-ray binary pulsars with respect to their observational characteristics as, e.g., X-ray luminosities, outburst behavior, pulse periods, etc. (see, e.g., Frank et al., 1992). Many of the X-ray characteristics are a direct consequence of the respective mass transfer mechanisms, which strongly depend on the properties of the optical companion star. For this reason, the mass of the optical companion allows for a rough classification of X-ray binaries: the *high mass X-ray binaries* (HMXBs) and the *low mass X-ray binaries* (LMXBs). Evolutionary scenarios for X-ray pulsars as well as the fundamental physics of mass transfer processes are described in more detail in the following Sections, with focus on HMXBs and especially Be-type systems, as they are the central part of this thesis. Note that the distinction between HMXBs and LMXBs can be applied for black hole X-ray binaries as well. However, black hole binaries are beyond the scope of this work and are therefore omitted in the following discussion.

2.1 Progenitor Systems of X-ray Binary Pulsars

PROGENITOR systems of X-ray binary pulsars undergo, depending on their masses, complex mass transfer processes when filling up their Roche lobes (for an example of a system consisting of a $8\,M_\odot$ and a $20\,M_\odot$ star, see Karttunen et al., 2007). The supernova explosion of one of the binary components results, in many cases, in the disruption of the system (e.g., Brandt & Podsiadlowski, 1995). In the other case, these authors found that the orbital parameters of the bound post-supernova system, which consists of a neutron star and an optical companion, are strongly affected by the supernova explosion. One possible consequence is a relatively large eccentricity, which was observed for many X-ray binary pulsars (e.g., Bildsten et al., 1997). Another interesting consequence is the theoretical prediction of different system velocities between HMXBs and LMXBs, caused by the natal kick of the supernova (Brandt & Podsiadlowski, 1995). These different velocities as well as the comparably long
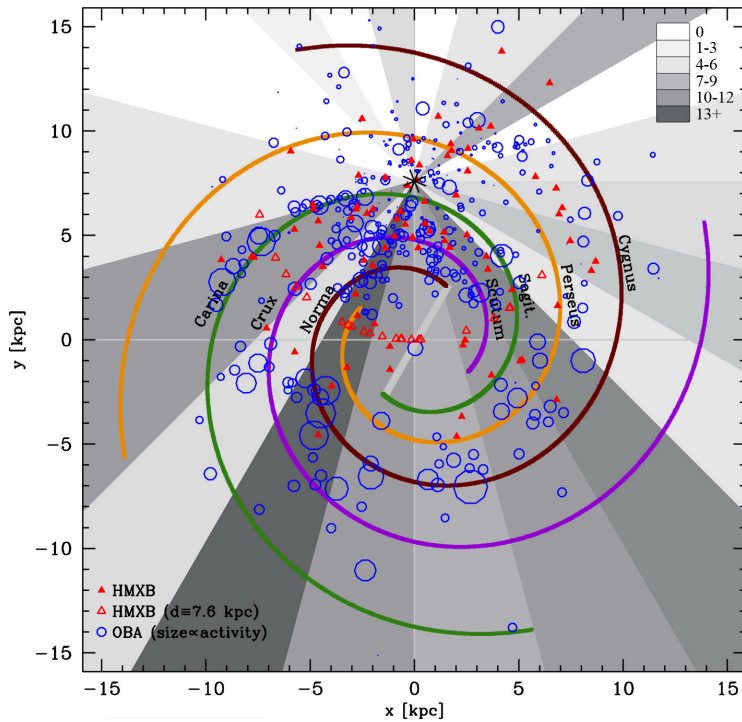
Figure 2.1: Location of HMXBs binaries in the Milky way (from Bodaghee et al., 2012). Filled red triangles correspond to systems with known distance d, while for the systems with unknown distances (red triangles), $d = 7.6\,\mathrm{kpc}$ has been assumed. Blue circles indicate OB-associations. The radii of these circles scale with the respective amount of activity. The spiral arms of the Milky Way are based on Vallée (2008). The position of the sun is marked by an asterisk $*$. The gray shaded regions correspond to the number of HMXBs in $15°$ sized bins of the galactic longitude.

lifetime of LMXMs lead to a different spatial distribution of HMXBs and LMXBs. This was already confirmed by observational data (Brandt & Podsiadlowski, 1995; Bodaghee et al., 2012; Zhang et al., 2013).

2.2 High Mass X-ray Binaries

IN HMXBs, the OB-type optical companion star exceeds masses of $\sim10\,M_\odot$. The mass transfer in these systems happens either by the Be-mechanism (see Sect. 2.2.1), stellar wind (see Sect. 2.2.2), or Roche lobe overflow. Kaper & van der Meer (2007) found that $\sim80\%$ of all HMXBs have Be-type optical companions.

Bodaghee et al. (2012) studied the spatial distribution of HMXBs in the Milky Way with respect to OB associations (Russeil, 2003). These are regions, where many young blue stars are located and progenitor binary systems of X-ray binary pulsars are expected. Figure 2.1 displays these positions together with the positions of HMXBs. Bodaghee et al. (2012) found a clear correlation between the position of HMXBs and the OB associations. They explain deviations by natal kicks during the supernova explosions in the formation state of HMXBs.

In addition to the galactic X-ray binaries, these systems were also discovered in other galaxies, e.g., in the Magellanic Clouds (for reviews, see, e.g., Yokogawa et al., 2003; Haberl & Pietsch, 2004). The known distance to these systems and the relatively high galactic latitude (leading to a weak obscuration by the interstellar medium) are perfect conditions to study these objects. A catalogue of these systems is given in Liu et al. (2005).
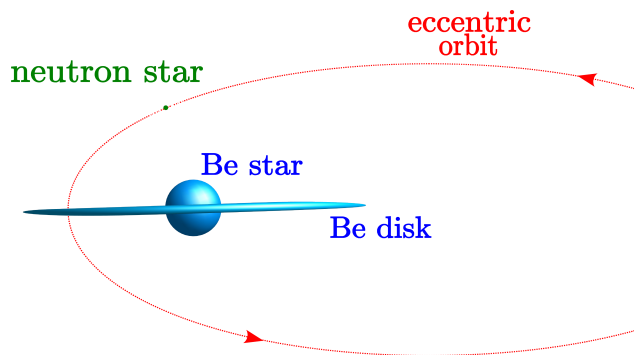
Figure 2.2: Simplified picture of the situation in a Be-X-ray binary. The neutron star (green) passes the Be-disk every orbital period at periastron passage. However, many observational results cannot be explained by this simple picture (Figure based on Kretschmar, 1996)

2.2.1 Be-X-ray Binaries

This type of X-ray binaries consists of a neutron star orbiting an Oe or Be-type optical companion (see Sect. 1.1.3) more or less elliptically (see, e.g., Coe, 2000, for a review). Mass transfer from the circumstellar disk onto the neutron star causes X-ray outbursts. The orbits of these so called "transient" systems can have relatively large eccentricities, typically of the order of a few 0.1 (Bildsten et al., 1997). The eccentricity of the orbit can be explained by the supernova explosion of the neutron star's remnant (see Sect. 2.1). As displayed in Fig. 2.2, this eccentricity possibly leads to the passage of the neutron star through the Be-disk every periastron passage, which causes an accumulation of material around the neutron star, or, in other words, an accretion disk is formed. Mass transfer from this disk onto the surface of the neutron star causes the emission of X-rays. Okazaki et al. (2013) showed that this picture in combination with the standard accretion disk modeling (Shakura & Sunyaev, 1973) is too simple to explain the outburst behavior of most of the Be-X-ray binaries. In the Shakura-model, accretion disks are geometrically thin, Keplerian, and stable because of centrifugal forces and gas pressure. This disk model leads to accretion timescales which are too long to explain typical observed outburst durations. Okazaki et al. (2013) suggested a more sophisticated accretion disk model and showed by 3d-simulations that the basic outburst properties can be explained by the truncation and/or the misalignment of the Be-disk with respect to the orbit of the neutron star. These outbursts are classified into type I and II outbursts (see Negueruela et al., 1998; Okazaki & Negueruela, 2001, and references cited therein). Based on Okazaki et al. (2013), the details of these types and the respective scenarios are discussed in the remainder of this Section.

2.2.1.1 Type I Outbursts

Type I outbursts show intermediate luminosities of the order of $L_X \approx 10^{36...37}\,\mathrm{erg\,s^{-1}}$. These periodical outbursts coincide with the epochs of periastron passages (Negueruela et al., 1998) and last typically $0.2 - 0.3\,P_{\mathrm{orb}}$ (Okazaki et al., 2013). An example of a source which undergoes relatively regular type I outbursts is EXO 2030+375 (Klochkov et al., 2011a). Furthermore, these authors analyzed an outburst in 2009, whose double peaked shape demonstrates the failure of the too simple picture of a steady Be-disk passed by the neutron star (Fig. 2.2).

Okazaki et al. (2013) presented simulations which are based on the Radiatively Inefficient Accretion Flows model (RIAF; Abramowicz et al., 1995). These simulations, which account for the misalignment between the orbital plane and the Be-disk, result in outbursts which are accompanied by the truncation of the Be-disk. The
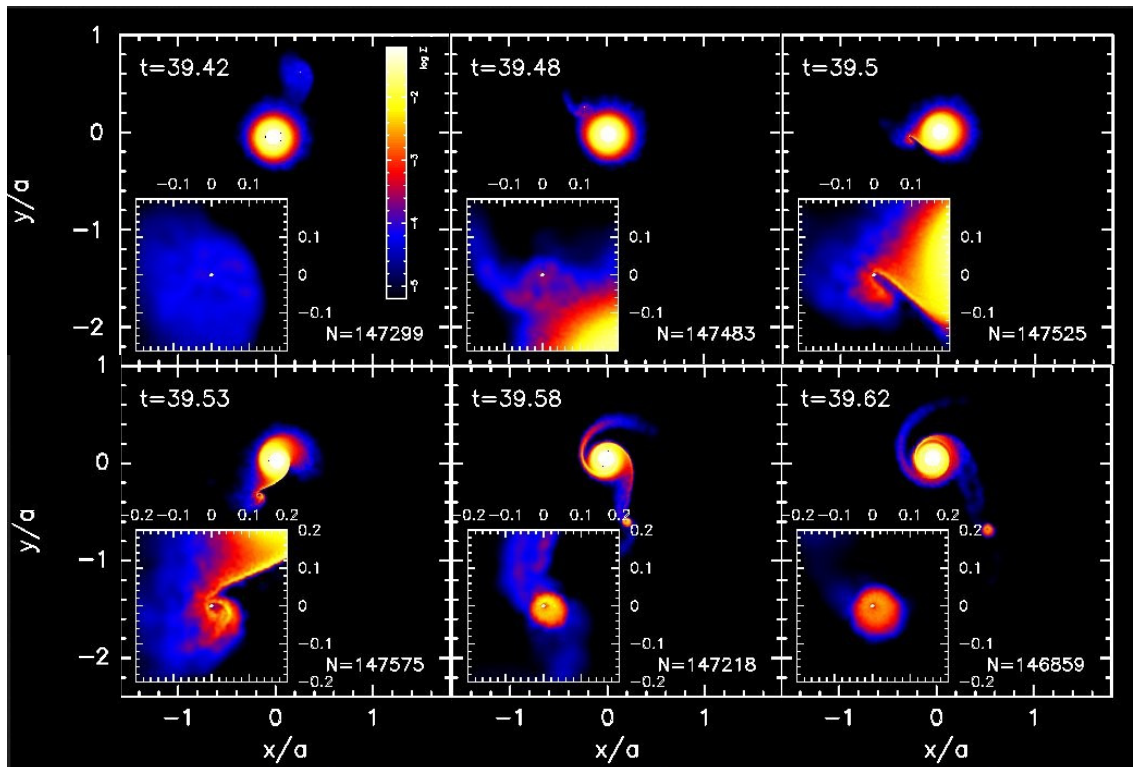
Figure 2.3: Coplanar 3d-simulation of the behaviour of the Be-disk in an X-ray binary (Okazaki et al., 2002). The simulation had been run with the parameters P_{orb} = 24.3 d and e = 0.68 for 40 orbital periods. The Figures, from top left to bottom right, show the 40th orbital period of the system (t in units of P_{orb}). The insets show a close-up view on the surroundings of the neutron star. The figure is shown by courtesy of Atsuo Okazaki. The complete movie can be found on his personal home page http:/www.lst.hokkai-s-u.ac.jp/~okazaki/astroinfo-e.html.

released matter from the Be-disk overrides the gap between the disk and the orbit of the neutron star and gets accreted. These simulations lead to luminosities and timescales of the outbursts which are consistent with the observational data.

Figure 2.3 shows snapshots of simulation from Okazaki et al. (2002) of the interaction between the Be-disk with the neutron star and its accretion disk. This Figure clearly demonstrates that the model, which is shown in Fig. 2.2, is far too simple to be able to explain real outburst mechanisms sufficiently. The deformation of the Be-disk and the formation of a spiral arm towards the neutron star show that the inset of an outburst must not neccessarily coincide with the periastron passage, which was observationally confirmed for, e.g., GRO J1008−57 (Kühnel et al., 2013) and 2S 1845−024 (Finger et al., 1999). Furthermore, these simulations are able to explain complex outburst shapes. By varying, e.g., the orbital parameters, multiple peaked outbursts, even during one orbital cycle, can be explained. For these cases, a second spiral arm, which is averted to the neutron star, separates from the Be-disk (see Fig. 2.3). This arm might hit the neutron star at a later orbital phase, which leads to another raise of the accretion rate.

2.2.1.2 Type II Outbursts

Type II or "giant" outbursts are characterized by significantly higher luminosities compared to Type I outbursts ($L_X \gtrsim 10^{37}\,\mathrm{erg\,s^{-1}}$, Negueruela et al., 1998). These outbursts can last several weeks or even months and start typically shortly after the periastron passage (Okazaki & Negueruela, 2001). However, these outbursts can be absent for even dozens of orbital cycles, as observed for, e.g., 4U 0115+634 (see Sect. 5).

The accretion scenario of type I outbursts cannot explain the high luminosities which are observed for giant type II outbursts. Following Okazaki et al. (2013), a misaligned Be-disk, which is warped towards the orbital plane, could explain these high values for L_X, when the warped edge happens to be close to the neutron star at periastron. These warped Be-disks are described theoretically by, e.g., Pringle (1996) and Martin et al. (2011), and are already observed for Be-X-ray transients undergoing type II outbursts (e.g., Moritani et al., 2011). Okazaki et al. (2013) modeled these outbursts, based on the *Bondi-Hoyle-Lyttleton Accretion* (Bondi & Hoyle, 1944) and, for reasons of simplification, rigidly tilted, isothermal Be-disks. Okazaki et al. (2013) showed that, because of tidal interactions, the accreted material can be accelerated to velocities which are larger than the Keplerian. This results into accretion timescales which are larger than the orbital period and luminosities which are in agreement with observations of type II outbursts (e.g., 4U 0115+634, Sect. 5). Furthermore, Okazaki et al. (2013) explained the occurence of the relatively long periods of quiescence by synchronization effects between the Be-disk and the orbital period.

Yan et al. (2012) suggested an alternative scenario for type II X-ray outbursts (based on Rivinius et al., 2001). For A 0535+26, Yan et al. (2012) detected a fading of the optical brightness during each giant outburst. This indicates mass ejection events of the Be-disk, which might trigger the giant type II outbursts of this system.

2.2.2 Wind Accretors

Optical companion stars in wind accretors are OB-type stars with high mass loss rates of the order of $10^{-6}-10^{-5}\,M_\odot\,\mathrm{yr^{-1}}$, which is caused by stellar winds with typical velocity profiles $v(r) \propto (1 - R_{OB}/r)^\beta$, where R_{OB} denotes the radius of the OB star and $\beta \approx \frac{1}{2}$ (Castor et al., 1975). Shapiro & Lightman (1976) showed for detached binaries with compact companions that these winds can be accreted onto the neutron stars, which leads to the emission of X-rays. Since the processes in these systems are very complicated, mainly numerical simulations of the accretion of stellar winds onto neutron stars are used (for an example, see Fig. 2.4). An estimate of the resulting fluxes leads to X-ray luminosities of the order of $10^{36}\,\mathrm{erg\,s^{-1}}$ (Mauche et al., 2008), which makes high mass wind accretors to the brightest X-ray sources in the sky. For a review for HMXB wind accretors, see, e.g., Sako et al. (2003). One of the most prominent examples of wind fed accreting pulsars is Vela X-1 (Odaka et al., 2013, and references cited therein).

2.3 Low Mass X-ray Binaries

Relatively low masses of the optical companions ($\lesssim 1\,M_\odot$) characterize LMXBs (e.g., Lewin et al., 1995, and references therein). One big observational difference between HMXBs and LMXBs is the lack of pulsations in many representants of
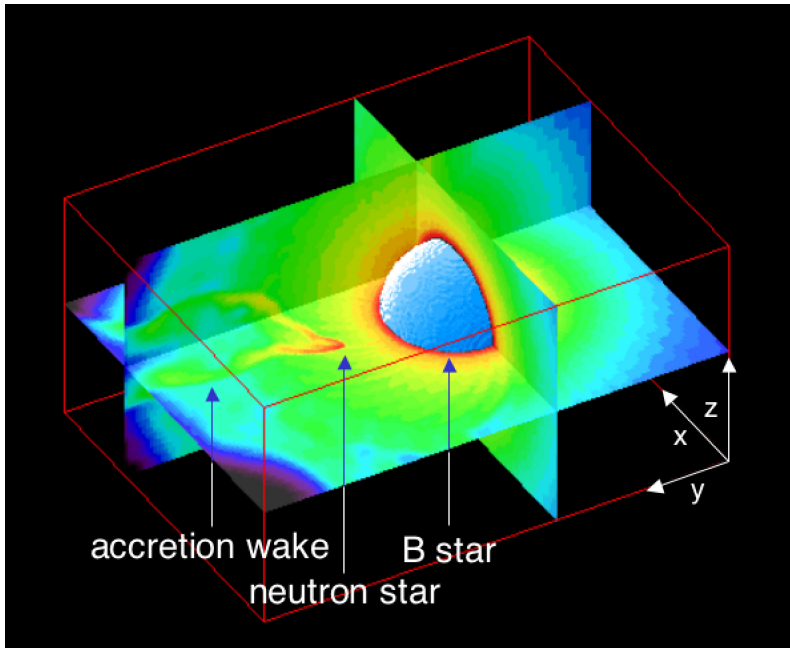
Figure 2.4: 3d-simulation of the stellar wind of the system Vela X-1 disturbed by the neutron star. The blue sphere displays the Be-star, while the colour map corresponds to the density of the wind (from reddish to bluish, corresponding to relatively high densities to low densities). As typically for this kind of source, an accretion wake has formed behind the neutron star. This Figure has been taken from Mauche et al. (2008).

the latter class. The reason for this remains still unclear (for a summary of this topic, see, e.g., Göğüş et al., 2007), however, the possibility that LMXBs are the progenitors of millisecond radio pulsars implies an explanation for these missing pulsations: the magnetic fields of evolved neutron stars in LMXBs might be so weak that the accreted matter cannot be channeled onto the poles of the neutron stars (see Sect. 2.4), which leads to the missing of pulsations (Alpar et al., 1982). Another possible scenario is the dilution of the pulsations by gravitational lensing effects (Mészáros et al., 1988). Furthermore, Brainerd & Lamb (1987) proposed another scenario, where the pulsated X-ray emission gets smeared by electron scattering processes within the surrounding cloud. Until today, these scenarios are discussed controversially and not one of the pictures is completely accepted yet.

For most of the LMXBs the mass accretion happens via Roche lobe overflow (Lasota, 2001, , and Sect. 2.3.1). Recently, a new class of LMXBs was proposed, i.e., the wind-fed *symbiotic X-ray binaries* (SyXBs; Masetti et al., 2006, , and Sect. 2.3.2). These two classes of systems are explained in the following.

2.3.1 Roche Lobe Overflow

In this subclass of LMXBs, the optical companion star exceeds its Roche lobe, which enables mass transfer onto the neutron star via the inner Lagrangian point L_1 (see Figs. 1.5 and 1.6). LMXBs typically undergo outbursts with luminosities of the order of $10^{36...39}\,\mathrm{erg\,s^{-1}}$ (Degenaar et al., 2012). Instabilities in the accretion disks surrounding neutron stars make LMXBs to become transient sources (see, e.g., Lasota, 2001, for a review).

2.3.2 Symbiotic X-ray Binaries

The name of this class of X-ray binaries originates from *symbiotic binaries*, where a white dwarf accretes material from the stellar wind of an M-type giant. In SyXBs, the compact object analogously accretes material from an evolved M-type giant (Masetti
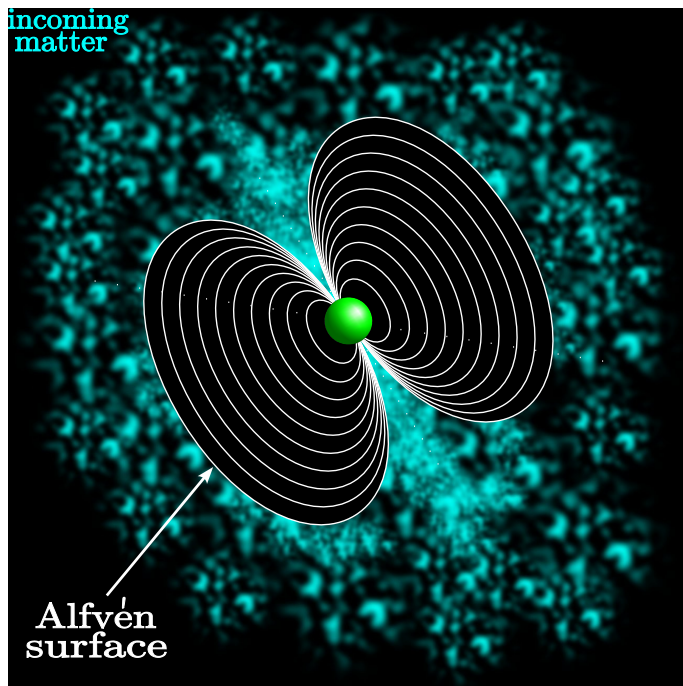
Figure 2.5: Schematic picture of the Alfvén surface of a neutron star (green sphere), from where the incoming matter (cyan clouds) gets channeled onto the magnetic poles following the magnetic field lines (white).

et al., 2006). Accretion via Roche lobe overflow is very unlikely for this type of systems, because they typically have large orbits (Chakrabarty et al., 1997). Typical X-ray luminosities of SyXBs vary between $10^{32}\,\mathrm{erg\,s^{-1}}$ and $10^{34}\,\mathrm{erg\,s^{-1}}$ (Masetti et al., 2007). Due to the short lifetime of M-type giants and the instable accretion process, SyXBs are supposed to be quite rare (Chakrabarty et al., 1997). As a consequence, till this day there are only eight known SyXBs (Nespoli et al., 2010).

In contrast to HMXB wind accretors, little is known about the properties and accretion processes of SyXBs. While the optical companions in HMXBs exhibit winds with velocities of the order of $\sim 1000\,\mathrm{km\,s^{-1}}$, the winds of M giants in the known SyXBs hardly exceed $\sim 100\,\mathrm{km\,s^{-1}}$ (e.g., Dupree, 1986). The only exception is GX 1+4 with wind velocities of $250 \pm 50\,\mathrm{km\,s^{-1}}$ (Chakrabarty et al., 1998). These slow winds in combination with relatively slow orbital motions of the neutron stars lead to large accretion radii for SyXBs (Paul et al., 2005). Under these conditions, complex accretion flows are expected, which lead to chaotic outburst behaviors of SyXBs.

2.4 Accretion Geometry

I N this Section, I set the focus on possible geometries and the respective physical processes in the direct surroundings of neutron stars accreting matter from optical companion stars. One of the most important quantities for accreting X-ray pulsars is the *Eddington luminosity*, L_{Edd}. Assuming spherical symmetric accretion, L_{Edd} is the highest possible X-ray luminosity, which is characterized by an equilibrium of the gravitational force and the radiation pressure (Frank et al., 1992). This luminosity is given by

$$L_{\mathrm{Edd}} = \frac{4\pi G M_{\mathrm{ns}} m_{\mathrm{p}} c}{\sigma_{\mathrm{T}}}, \qquad (2.1)$$

with the proton mass m_{p} and the Thomson scattering cross-section σ_{T}.

However, the naive picture that the accreted matter simply "rains" uniformly onto
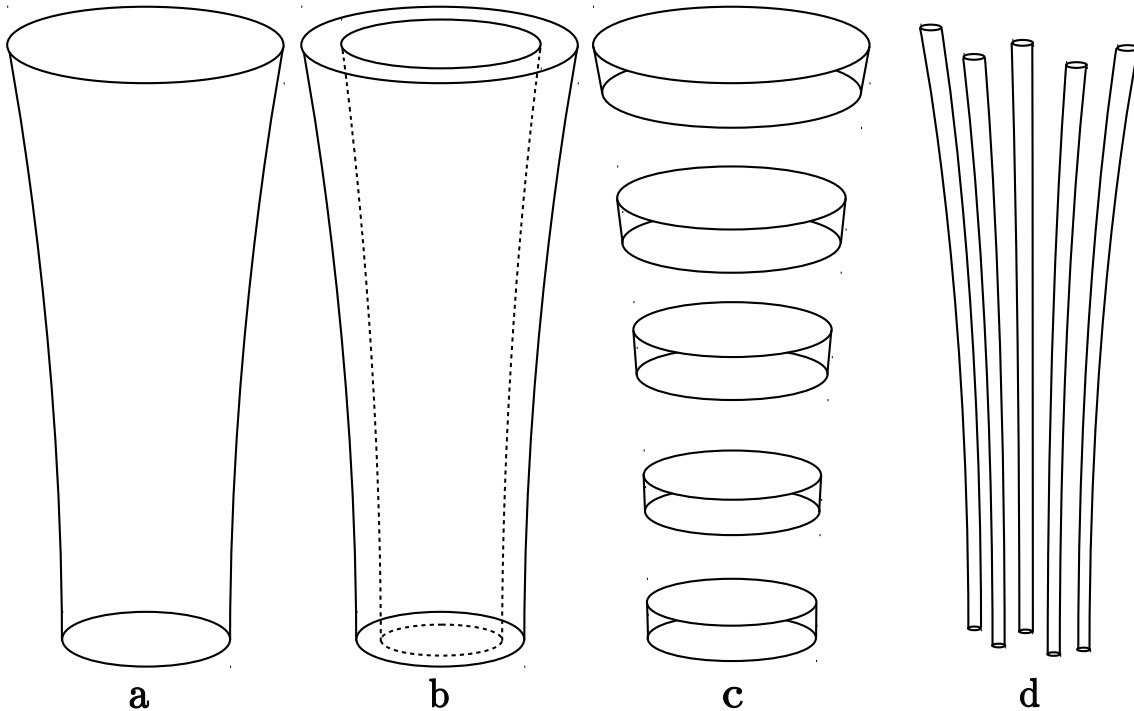
Figure 2.6: Possible accretion column geometries (Mészáros, 1984). See text for details.

the neutron star's surface or hits its crust on the circle, where the accretion disk cuts the stellar surface, is not able to explain typical characteristics of these systems sufficiently. One rather has to account for strong interactions between the magnetic fields of the neutron star and the accreted matter. The distance from the center of the neutron star to the position, where the magnetic energy density equals the kinetic energy density is called the *Alfvén radius*, r_A. At distances closer to the neutron star than r_A, the motion of the accreted material is not dominated by the gravitational forces of the neutron star, but by magnetic forces. Approximating the magnetic field of the neutron star with a dipole (magnetic field strength $B \propto r^{-3}$), the Alfvén radius can be calculated as

$$r_A = \left(\frac{B_s^4 R_{ns}^{12}}{2GM_{ns}\dot{M}^2} \right)^{1/7} , \qquad (2.2)$$

where B_s denotes the magnetic field strength on the surface of the neutron star, R_{ns} and M_{ns} the radius and the mass of the neutron star, and $\dot{M}$ the mass accretion rate. This relation yields typical values for r_A of $\sim 3 \times 10^8$ cm or $\sim 300\,R_{ns}$ (Carroll & Ostlie, 2007). As indicated in Fig. 2.5, an accretion disk which surrounds the neutron star or any other accretion flow gets disrupted at the Alfvén radius. The matter then follows the magnetic field lines forming accretion columns on the magnetic poles of the neutron star. The details of possible geometrical shapes of these columns depend on the exact coupling of matter and homogeneity of the accretion flow and still remain an open question (Mészáros, 1984). The most simple possible shape is a filled cylinder (Fig. 2.6a). However, more complicated shapes like hollow cylinders, several subsequent layers, or even multiple smaller cylinders are thinkable as well (Fig. 2.6b–d).

Assuming the accreted material to be channeled into accretion columns on the magnetic poles has an interesting consequence for the Eddington luminosity (e.g., Basko & Sunyaev, 1976; Becker et al., 2012). Following Becker et al. (2012), for the
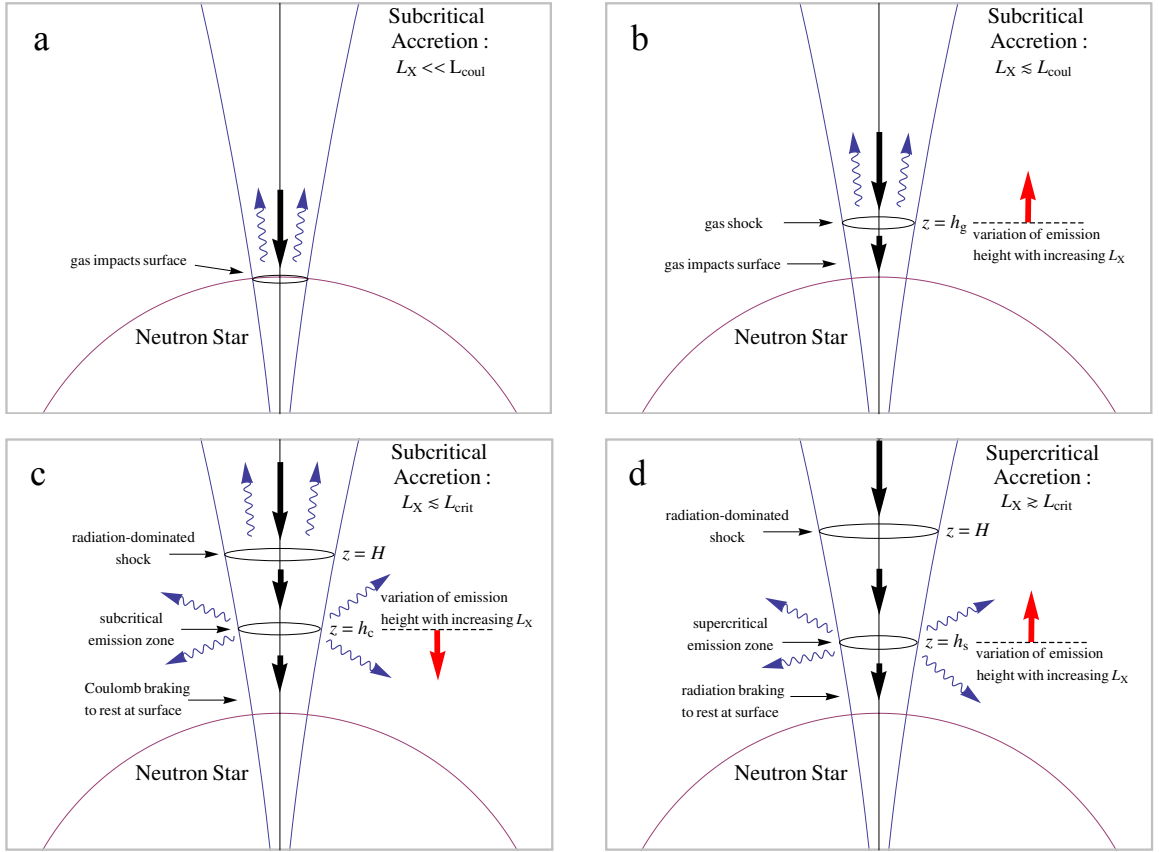
Figure 2.7: Schematic sketch of accretion columns depending on the luminosity (taken from Becker et al., 2012). See text for details.

case of the formation of accretion columns, two modifications have to be done when calculating the *modified Eddington luminosity*, L^*_{Edd}: a), scaling L_{Edd} down to the ratio of the neutron star's surface area and the cross-sectional area of the accretion column, and b), replacing σ_{T} by $\sigma_{\parallel}$, the mean cross section for photons propagating parallel to the magnetic field. This yields

$$L^*_{\mathrm{Edd}} = \frac{GM_{\mathrm{ns}}m_{\mathrm{p}}c}{\sigma_{\parallel}} \times \frac{\pi r^2_{\mathrm{a}}}{R^2_{\mathrm{ns}}}, \tag{2.3}$$

with the radius of the accretion column r_{a}. The Eddington luminosity can be exceeded locally. Depending on the luminosity regime, radiative dominated shock fronts can form in the accretion columns. These regimes are separated by the so called *critical luminosity*, L_{crit}. Becker et al. (2012) calculated an analytical expression for L_{crit} and modeled the physical processes within the accretion column, depending on the mass accretion rate or, in other words, the X-ray luminosity of the system.

- $L_{\mathrm{X}} \ll L_{\mathrm{crit}}$: "subcritical accretion"

  Whilst the luminosity is less than $\sim 10^{34-35}\,\mathrm{erg\,s^{-1}}$, a hot spot forms at the bottom of the accretion column, which moves higher up with increasing mass accretion rate (see Fig. 2.7a). With increasing luminosity, a gas mediated shock forms on top of this mound and the plasma is decelerated via Coulomb interactions before it reaches the surface of the neutron star (Langer & Rappaport,
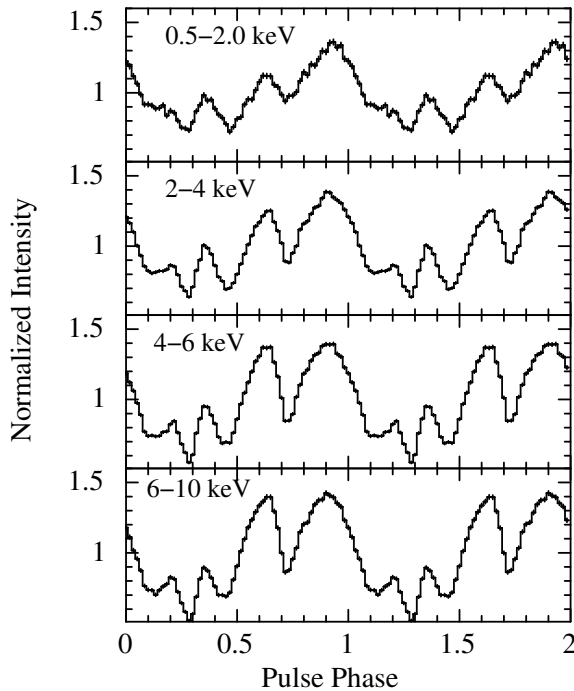
Figure 2.8:   Pulse profiles of EXO 2030+375 for different energy bands (Naik et al., 2013).

1982). The radiation is assumed to be emitted from the top of the accretion column and forms a so called *pencil beam* (e.g., Nelson et al., 1993). A schematic picture of this case is displayed in Fig. 2.7b.

- $L_X \lesssim L_{crit}$: "subcritical accretion"

  Once L_X reaches values of the order of L_{crit} (which is $\sim 10^{35-37}\,\mathrm{erg\,s^{-1}}$), a radiation dominated shock in the accretion column is formed. The thermal radiation, which is emitted by the accretion mound, gets up-scattered by inverse Compton scattering within the accretion column. These photons escape from the column below the shock via the walls and upwards from the top of the shock and form a mixture of *pencil* and *fan beam* (Blum & Kraus, 2000). In this luminosity regime, the radiation dominated shock front, which is coupled to the characteristic X-ray emission region, moves downwards with increasing L_X (see Fig. 2.7c). The final deceleration at the bottom of the accretion column happens via Coulomb interactions within a plasma cloud close to the surface of the neutron star (Nelson et al., 1993).

- $L_X \gtrsim L_{crit}$: "supercritical accretion"

  At very high luminosities ($L_X \approx 10^{37-38}\,\mathrm{erg\,s^{-1}}$), the plasma in the accretion column below the shock surface gets completely decelerated via the radiation field (Basko & Sunyaev, 1976). In this case, the typical emission region moves upwards with increasing L_X (see Fig. 2.7d). The radiation escapes mainly through the walls of the accretion column below the shock surface and leads to a *fan beam* (Davidson, 1973).

2.5   Pulse Profiles

SINCE in many cases the neutron star's rotational and magnetic axes are not aligned, the changing viewing angle onto the rotating accretion columns leads
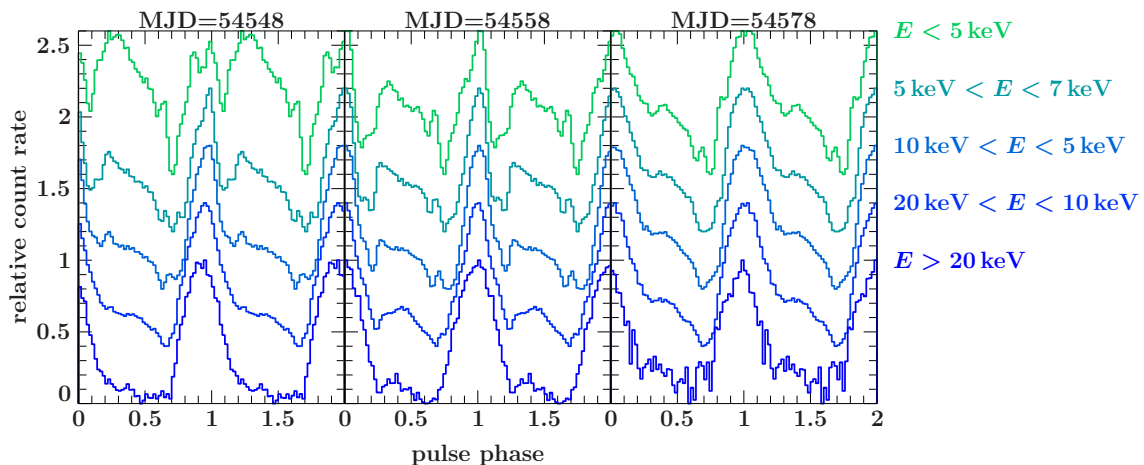
Figure 2.9: Pulse profiles of 4U 0115+634 for different energy bands and epochs during a giant outburst in 2008 (Müller et al., 2010).

to a periodical variation of the X-ray flux. The most common case, a two-peaked structure, could in principle be explained by the simplified picture of the seperate X-ray emission of the two accretion columns, which correspond to the two peaks in the pulse profile. Various theoretical efforts were made to model the shape of pulse profiles more realistically. Effects like gravitational light bending and halos caused by the illumination of the surface of the neutron star, etc., have to be taken into account for these models which makes them highly complex and geometry dependent (e.g., Kraus et al., 1995, 2003; Falkner, 2013). Because of relativistic light bending effects, the averted column should mostly be also visible and contributes to the flux of both peaks. Another effect is the asymmetry between the two pulse peaks, which is probably caused by an asymmetric and/or not antipodal magnetic field, which results in the occurrence of different accretion columns (see, e.g., Leahy, 1991).

In addition to two peaked pulse profiles, more complex shapes are observed. One of the most prominent examples is EXO 2030+375 (e.g., Sasaki et al., 2010). As shown in Fig. 2.8, the pulse profile of this source has multiple peaks. Sasaki et al. (2010) explained the complicated pulse shape of EXO 2030+375 and its variability by a certain change in geometry and by several occultations and light bending effects. Even more complicated pulse profiles can be produced taking more complicated geometries of the accretion columns (see Fig. 2.6) into account (Falkner, 2013).

Additionally, the pulse profile strongly depends on the energy band. For example, Raubenheimer (1990) reported that for Vela X-1, at low energies below $\sim$6–20 keV, the pulse profile shows five peaks and for higher energies a double peaked structure becomes apparent. These observational results can be explained by the visibility of different parts of the accretion column for different energy bands, which is caused by differences of the emitted photon spectra depending on the emission height of the accretion column (Becker & Wolff, 2007). Figure 2.9 shows the energy dependent pulse profiles of 4U 0115+634. As typical for these kinds of X-ray sources, the pulse profile looks more complicated for lower energies, while for higher energies only one pulse is present.

27
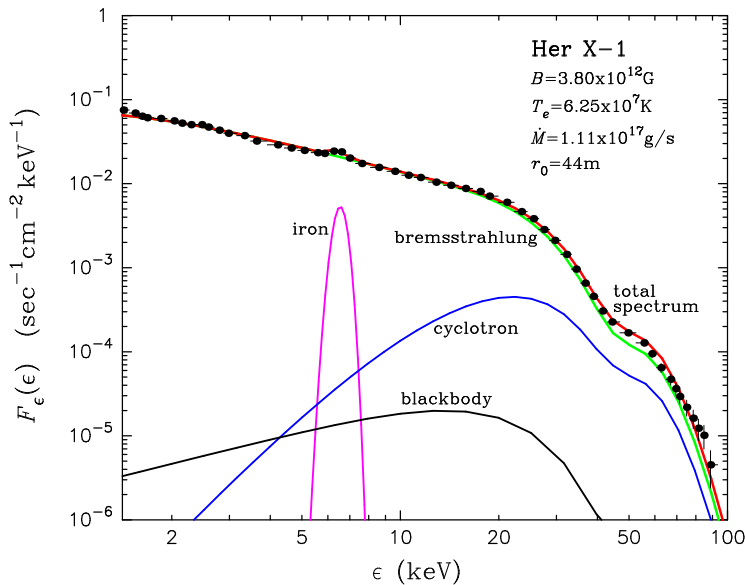
Figure 2.10: Column integrated, theoretical count rate spectrum of Her X-1, together with an observed *BeppoSAX* spectrum (black data points, dal Fiume et al., 1998). The red curve shows the total physical continuum model. The other curves display individual model components, i.e., bremsstrahlung radiation, cyclotron emission, black body emission, and the Fe Kα fluorescence line (see Sect. 2.6.2.2). The plot has been taken from Becker & Wolff (2007).

2.6 X-ray Spectra of Accreting Pulsars

THE processes described in Sect. 2.4 lead to the emission of X-rays. Radiation emitted by the accretion mound can be approximated by the spectrum of a black body. Typical temperatures of this mound result in a flux maximum at $\sim 10\,$keV (e.g., see the black body found in GRO J1008–57, Kühnel et al., 2013). However, not all X-ray pulsars require this model component to describe the broadband spectrum well (see, e.g., 4U 0115+634, Müller et al., 2013). Inverse Compton scattering of the thermal photons emitted by the accretion mound within the accretion column leads to a further broadening of the X-ray spectrum. Additionally, photons are emitted via bremsstrahlung, i.e., the interaction between the electrons and ions in the accretion column (Becker & Wolff, 2007). Cyclotron emission contributes to the total X-ray spectrum of accreting pulsars. Figure 2.10 shows an example for a deconvolved spectrum of the system Her X-1 together with the individual model components (Becker & Wolff, 2007), described by the physical parameters as given in the Figure. Comparing the total theoretical spectrum with a *BeppoSAX* spectrum of this source (data points in Fig. 2.10, dal Fiume et al., 1998) Becker & Wolff (2007) demonstrated that physical models are indeed able to describe observations well. However, with a large number of free fit parameters and the resulting need of fixing parameters, it is in many cases problematic to apply these models to observed spectra. As a consequence, X-ray spectra are mostly modeled by semi-physical models, i.e., some variant of a high energy exponential cutoff (Kreykenbohm et al., 2002, and references therein). However, not all spectral models can be successfully applied to every dataset. Finding a good description of a certain dataset is in many cases a long process, where many different models have to be tested and additional model components, as described in Sect. 2.6.2, have to be applied. Sometimes, different empirical models in combination with different additional model components even describe spectra equally well. In these cases, the experience of the scientist is important to decide which model leads to more meaningful results from a physical point of view and should therefore be the choice for the analysis. One example is 4U 0115+634, which is described extensively in Sect. 5. Based on Müller et al. (2013), and references therein, the most common models which are used to describe X-ray spectra of accreting pulsars, are described

in Sect. 2.6.1. Further model components which are sometimes needed to describe X-ray spectra of accreting X-ray pulsars, are described in Sect. 2.6.2.

2.6.1 Phenomenological Models

As described in the previous Section, a big problem of modeling X-ray spectra of neutron star pulsars are the complex physical processes within the accretion columns. In the following I describe the most common empirical continuum models for X-ray binary pulsars. In many cases, simple models with three fit parameters are not sufficient to give a reasonable description of the observed spectra. For these cases, other models with a higher number of free fit parameters are used. Within this thesis, I use the same notation for the continuum models consistently. However, note that the same model often does not have unique designations in the literature.

- **The Cutoff-Power-Law (`CutoffPL`):**
  The `CutoffPL` is the most basic exponential cutoff power-law model, given by

$$\texttt{CutoffPL}(E) \propto E^{-\Gamma} \exp\left(-\frac{E}{E_{\text{fold}}}\right). \tag{2.4}$$

  The photon index, Γ, describes the slope of the spectrum. A higher value for Γ corresponds to a steeper or, in other words, softer spectrum. The folding energy, E_{fold}, is a parameter which corresponds to the temperature of the electrons in the accreted plasma.

- **The Power-Law with a High Energy Cutoff (`PLCUT`):**
  An example for a model with one more free parameter is the so called `PLCUT` (e.g., White et al., 1983), given by[1]

$$\texttt{PLCUT}(E) \propto \begin{cases} E^{-\Gamma} & \text{for } E \leq E_{\text{break}} \\ E^{-\Gamma} \exp\left((E_{\text{break}} - E)/E_{\text{fold}}\right) & \text{for } E > E_{\text{break}} \end{cases}. \tag{2.5}$$

  The high energy rollover, E_{break}, is typically at energies around $10\,\text{keV}$. This model often results in an unphysical "kink" at E_{break}, which can possibly look like a line-like feature and can easily be misinterpreted (Kreykenbohm et al., 1999). In contrast to the blue curve of Fig. 2.11a, which corresponds to the `CutoffPL`, the red curve, which correspond to the `PLCUT`, gives an example for a kink at $15.5\,\text{keV}$. To avoid this problem, Klochkov et al. (2008) and Ferrigno et al. (2009) introduced a modified version of `PLCUT`, i.e., a model of the form

$$\texttt{PLINT}(E) \propto \begin{cases} E^{-\Gamma} & \text{for } E \leq E_{\text{break}} - \Delta E \\ AE^3 + BE^2 + CE + D & \text{for } |E - E_{\text{break}}| < \Delta E \\ E^{-\Gamma} \exp\left(-E/E_{\text{fold}}\right) & \text{for } E \geq E_{\text{break}} + \Delta E \end{cases} \tag{2.6}$$

  where the coefficients A, B, C, and D are chosen in a way that the respective kink vanishes at E_{break}. The conditions for these coefficients are that the model and its first derivative have to be continuous at $E = E_{\text{break}} \pm \Delta E$ with sufficient small ΔE.

---

[1]This relation is sometimes given by $E^{-\Gamma} \exp\left(-E/E_{\text{fold}}\right)$ for $E > E_{\text{break}}$. The "missing" E_{break} in the exponential factor can be compensated by the normalization. As a consequence, these two different expressions are analytically equivalent.
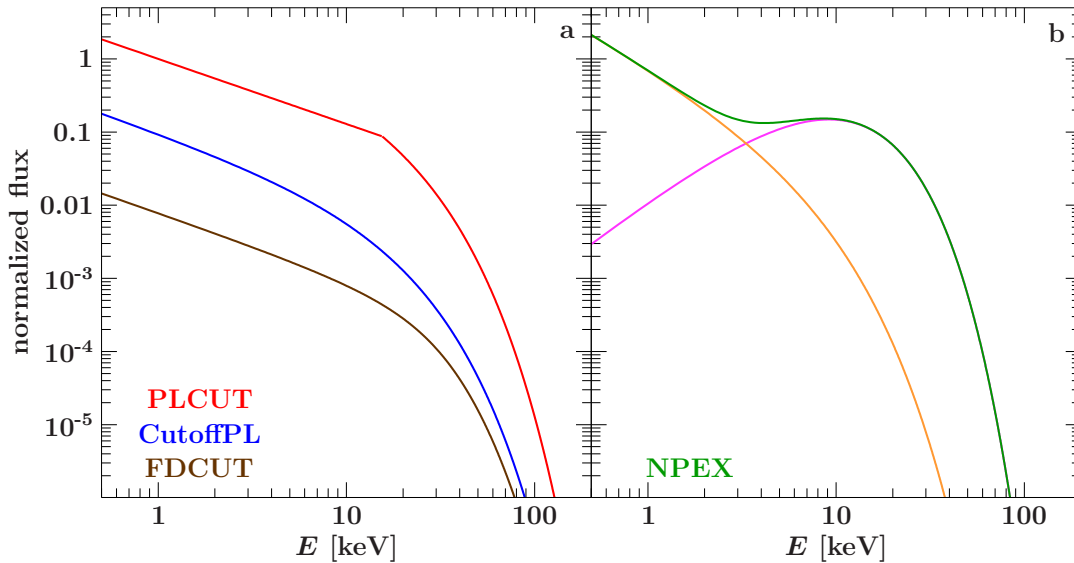
Figure 2.11: a: Model spectra, i.e., the `CutoffPL` (blue), the `PLCUT` (red), and the `FDCUT` (brown). For these curves, fit values for the source MXB 0656−072 (Γ = 0.89, E_{break} = 15.5 keV, and E_{fold} = 11.8 keV, McBride et al., 2006) are used. For clarity, the curves are shifted in y-direction. b: `NPEX` model spectrum (green), together with the negative (orange) and the positive (purple) power-law with an exponential cutoff factor. For `NPEX`, values typical for the source 4U 0115+634 (Γ_1 = 1.48, Γ_2 = 2, flux ratio α = 1.54 × 10^{-2}, and E_{fold} = 4.58 keV, Nakajima et al., 2006) are used.

- **The `NPEX` model:**
  The Negative and Positive power-laws with a common EXponential cutoff factor, which is called the `NPEX` model, is one of the models based on the idea of a physically meaningful description of the spectra (see, e.g., Makishima et al., 1999, and references therein). It is given by

  $$\textbf{NPEX}(E) \propto \left(E^{-\Gamma_1} + \alpha E^{+\Gamma_2}\right) \exp\left(-\frac{E}{E_{\text{fold}}}\right), \qquad (2.7)$$

  with positive photon indices, $\Gamma_{1/2}$. An example for the `NPEX` model is displayed in Fig. 2.11b. The idea behind `NPEX` is that besides the typical negative power law, the positive power law (Γ_2 is often fixed to 2, e.g., Nakajima et al., 2006) models a Wien hump, which is a result from inverse Comptonization on a hot electron gas. More elaborated models based on a theoretical description of inverse Comptonization of soft photons in an electron gas (e.g., Titarchuk, 1994) often fail to describe X-ray spectra (e.g., Vela X-1, Kreykenbohm, 1997), while for `NPEX` this kind of problem hardly occurs. This implies that, in reality, the processes within the accretion columns are too complicated to be described by this quite simple theory, but the relatively wide parameter range of `NPEX` allows for a de facto empirical description of the X-ray spectra.

- **The Fermi Dirac Cutoff (`FDCUT`):**
  Another empirical continuum model is the power-law, modified with the Fermi Dirac Cutoff (Tanaka, 1986), given by

  $$\textbf{FDCUT}(E) \propto E^{-\Gamma} \left(1 + \exp\left(\frac{E - E_{\text{break}}}{E_{\text{fold}}}\right)\right)^{-1}. \qquad (2.8)$$

  The brown curve in Fig. 2.11a displays a curve which corresponds to the `FDCUT`.
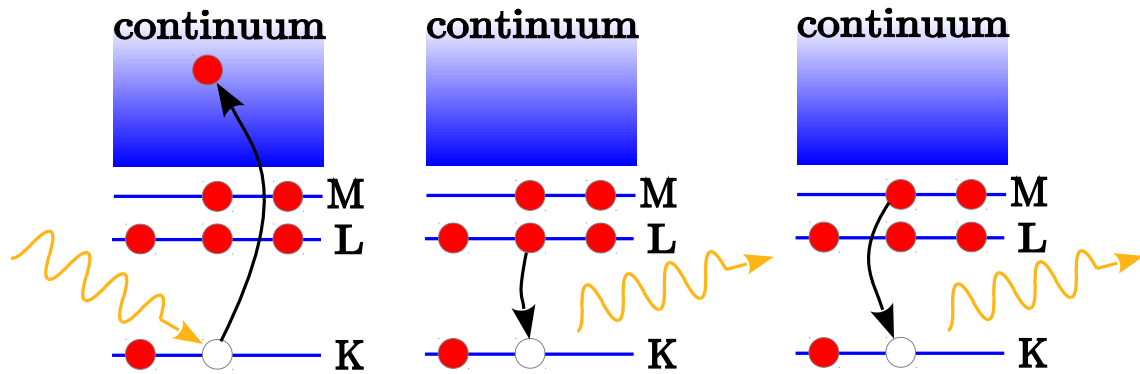
Figure 2.12: Basic processes of photoelectric ionization and fluorescence. Left: absorption of a photon, which leads to the ionization of the atom. Middle: Emission of Kα fluorescence. Right: Emission of Kβ fluorescence. This Figure is based on Als-Nielsen & McMorrow (2001).

2.6.2   Further Model Components

For many accreting X-ray pulsars, the models which are described in Sect. 2.6.1 alone do not give a sufficient description of observed spectra. For these cases, additional model components have to be used. Some of these components have a well known physical origin, e.g., scattering and absorption processes between the X-ray photons and the material located between the X-ray emitter and the observer. This material can be either interstellar, or part of the binary system (the subsequent Sects. 2.6.2.1 and 2.6.2.2 on these processes are based on the text books Als-Nielsen & McMorrow, 2001, Draine, 2011, and the Ph.D. thesis of Fürst, 2011). However, as I describe in Sect. 2.6.2.4, the physical background is not clear for all features. In this Section I explain the most important additional model components. Note that cyclotron resonance scattering features, which are also important spectral components, are explained in Sect. 2.7.2 extensively.

2.6.2.1   Photoelectric Absorption

One of the important processes which have influence on the shape of the X-ray continuum is photoelectric absorption, where X-ray photons are absorbed by atoms. The respective energy transfer leads to an excitation of the electron to a higher quantum level or even to an ionization of the atom ($X + h\nu \longrightarrow X^+ + e^-$, see Fig. 2.12, left). The cross section, σ, describes the probability that a photon is absorbed by an atom. Transitions between the discrete energies in the electron shells of atoms and the continuum lead to edges in the energy dependence of σ, which was observed in spectra of X-ray pulsars (e.g., GX 301$-$2, Swank et al., 1976). An important edge for X-ray astronomy is the iron K-edge at 7.1 keV. For the analyses presented in this work, I model the photoelectric absorption with **tbnew**[2], which is an updated version of **tbabs** (Wilms et al., 2000), and use element abundances by Verner & Yakovlev (1995). The only absorption parameter which is allowed to vary is the equivalent hydrogen column density, N_{H}.

These absorption processes of X-rays and the requirement of an additional model component complicate the analyses of X-ray spectra further. However, absorption allows for studying the material through which the X-rays are propagating. The

---

[2]http://pulsar.sternwarte.uni-erlangen.de/wilms/research/tbabs/

dynamics and material flows within the binary system lead to a variation of N_H over time, which can be studied (e.g., GX 301$-$2, Fürst et al., 2011b).

2.6.2.2 Fluorescence

Absorption of a photon by an inner shell electron leads to a vacancy in this shell. This vacancy in, e.g., the K shell, can be compensated by an electron from a higher shell, which leads to the emission of a photon with an energy equal to the energy difference between these levels. This process is called *fluorescence*. Important for X-ray spectra of accreting pulsar are the transitions L→K and M→K in iron, corresponding to the energies 6.4 keV and 7.1 keV. These transitions are called Kα and Kβ, respectively. Second order effects, which are caused by the quantum mechanical coupling between the orbital and the spin quantum number, are small enough to be neglected in this work.

Similar to photoelectric absorption, fluorescence lines allow for studying the material, interacting with the X-ray radiation. For example, stellar winds can be analyzed with the help of the behavior of the respective fluorescence lines and the column density (for an extensive discussion on this topic, see, Fürst, 2011, and references cited therein).

2.6.2.3 The Emission of the Galactic Ridge

The Galactic plane emits diffuse X-rays below ∼10 keV (e.g., Worrall et al., 1982; Warwick et al., 1985). Ebisawa et al. (2007) described the Galactic ridge emission (GRE) as the sum of two bremsstrahlung components, and an iron line complex, modeled by three Gaussian lines at 6.4 keV, 6.67 keV, and 7.0 keV, with ratios of the equivalent widths of 85:458:129, respectively. However, the question whether the GRE is emitted by many faint point-like sources or has a truly diffuse origin remained unanswered for a long time (see, Ebisawa et al., 2001, and references cited therein). Recently, Morihana et al. (2013) concluded that the real origin of the GRE are point sources like cataclysmic variables, symbiotic stars, and extragalactic sources.

When analyzing X-ray spectra of accreting pulsars which are located in the vicinity of the galactic plane this emission should be taken into account. Especially, when using observations of multiple instruments with simulated and measured background simultaneously, the GRE possibly leads to a disagreement between these instruments. For example, simultaneous *RXTE* (see Sect. 3.4) and *Swift* (see Sect. 3.6) observations of XTE J1946+274 lead to these problems (see Sect. 4).

The fundamental problem of modeling the GRE is the variation of its strength over the Galactic plane (Yamauchi et al., 2009). That means that the strength of this emission has to be measured for each source individually. This is only possible directly, if the source is in a state of quiescence, or if instruments with a measured background are used simultaneously to instruments with modeled background. On the other hand, the GRE's strength is assumed to be constant over time. Thus, for time resolved X-ray analyses with spectra contaminated by the GRE, one can assume that this additional feature is not affected by temporal variations.

2.6.2.4 The 10 keV Feature

Applying broadband X-ray spectral models often leads to remaining residuals around 10 keV. Primarily, this feature occurs for cyclotron sources (cyclotron resonance scat-

tering features are explained in Sect. 2.7), however, there is no evidence that this feature is connected to the magnetic field of the neutron star and its origin remains an open question (Coburn, 2001; Müller et al., 2012). The 10 keV feature could be caused by real physical processes like, e.g., absorption. However, this feature could be also caused by a fundamental problem of empirical continuum models around ~ 10 keV, which can be compensated by this additional Gaussian feature. One reason for this assumption is the energy of this feature, which is located in the band between the soft energies, emitted by hot material at the bottom of the accretion column, and the hard energies, emitted from higher regions of the column. The intersection region is quite hard to model and could possibly explain this, until today, mysterious feature.

In some cases, this feature might be caused by other effects. E.g., the spectra of 4U 0115+634 contain cyclotron resonance scattering features around 11 keV (see Sect. 5, and references quoted there). These features can be complex in shape and might sometimes show wings in emission (a detailed discussion about these features is given in Sect. 2.7). The failure of the classical cyclotron line modeling can, in these cases, be compensated with an additional Gaussian feature.

For some sources, the 10 keV feature appears in absorption (e.g., XTE J1946+274, Müller et al., 2012), for others in emission (e.g., 4U 0115+634, Müller et al., 2013). For the case of absorption, the 10 keV feature is often modeled by a multiplicative Gaussian optical depth profile $\exp(-\tau(E))$, with

$$\tau(E) = \tau \times \exp\left[-\frac{1}{2}\left(\frac{E - E_0}{\sigma}\right)^2\right], \tag{2.9}$$

with the optical depth, τ, the centroid energy, E_0, and width, σ. For the case of emission, this feature is often modeled by an additional Gaussian component, given by

$$G(E) \propto \exp\left[-\frac{1}{2}\left(\frac{E - E_0}{\sigma}\right)^2\right]. \tag{2.10}$$

2.7 Cyclotron Resonance Scattering Features

IN this Section, I set the focus on *cyclotron resonance scattering features* (cyclotron lines, or just CRSFs) from a theoretical, but also from an observational point of view. For detailed discussions on this topic, see, among many others, Schönherr et al. (2007), Schwarm (2010) and the papers cited therein. The theoretical part of the following Section is based on Mészáros (1992), Schwarm (2010), and references cited therein.

2.7.1 Larmor Radius & Landau Levels

From the classical point of view, the motion of a charged particle in a magnetic field (see, e.g., Daugherty & Harding, 1986, or the text book Mészáros, 1992) can be described by a helix (see Fig. 2.13). The radius of this trajectory is called the *Larmor radius*, R_L, given by

$$R_L = \frac{v_\perp m_e}{eB}, \tag{2.11}$$

in cgs units with $v_\perp$ denoting the velocity component of the electron perpendicular to the magnetic field vector, m_e the mass and e the charge of an electron. For relativistic
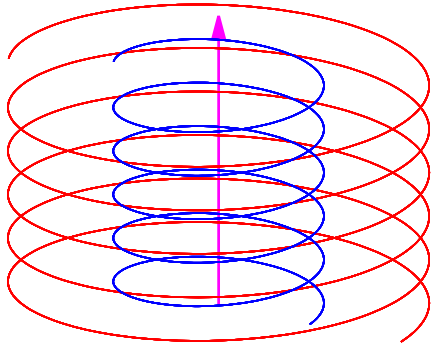
Figure 2.13: Sketch of possible trajectories of a charged particle corresponding to two Larmor radii. The arrow indicates the direction of the B-field.

electrons, the Larmor radius, given by Eq. 2.11, has to be multiplied with the Lorentz factor, $\gamma = 1/\sqrt{1 - (v/c)^2}$. This treatment is valid as long as the Larmor radius is much larger than the de Broglie-wavelength of an electron, i.e., if the magnetic field strength is much lower than the *critical magnetic field*

$$B_{\mathrm{crit}} = \frac{2\pi m_{\mathrm{e}}^2 c^3}{eh} \approx 4.4 \times 10^{13}\,\mathrm{G}. \tag{2.12}$$

As shown in Sect. 1.2.2.3, B-fields of neutron stars can get close to or even exceed B_{crit}, making a quantum electro dynamic (QED) treatment necessary to describe the motion of charged particles which move in the vicinity of these objects (e.g., Nagel, 1980; Araya-Góchez & Harding, 2000). From these calculations follow that electrons in these strong B-fields exhibit a quantization of the kinetic energy perpendicular to the B-field vector. The respective discrete energies are called *Landau levels*, and are given by

$$E_n = m_{\mathrm{e}} c^2 \frac{\sqrt{1 + 2(n+1)B^* \sin^2 \theta} - 1}{\sin^2 \theta}, \tag{2.13}$$

with $n \in \mathbb{N}_0$, $B^* := B/B_{\mathrm{crit}}$, and $\theta := \angle(\vec{v}, \vec{B})$. The special case $n = 0$ is called the *fundamental energy*. For sufficient small values of B, Eq. 2.13 is often approximated by the "12-B-12" rule

$$E_n\,[\mathrm{keV}] \approx 11.6(n+1) \times \left(\frac{B}{10^{12}\,\mathrm{G}}\right). \tag{2.14}$$

Figure 2.14 displays the energy as obtained from Eq. 2.13 and the percentage deviation of this energy and the result from the 12-B-12 rule (Eq. 2.14). This plot demonstrates that for B-field strengths which are typical for X-ray pulsars the 12-B-12 rule is valid within a few percent.

2.7.2 Cyclotron Lines in X-ray Spectra

Transitions of electrons between different Landau levels (Sect. 2.7.1) manifest themselves through the presence of cyclotron absorption-like features in the X-ray spectra of some accreting X-ray pulsars. The observed line energies are redshifted by $\frac{1}{1+z}$, where z denotes the gravitational redshift. According to the 12-B-12 rule (Eq. 2.14), the centroid energy of a CRSF allows for a direct measurement of the B-field strength close to a neutron star. The width of a CRSF is expected to vary with a changing centroid energy. As quantified by, e.g., Mészáros & Nagel (1985) and observationally confirmed by Coburn (2001), there is a correlation between the centroid energy
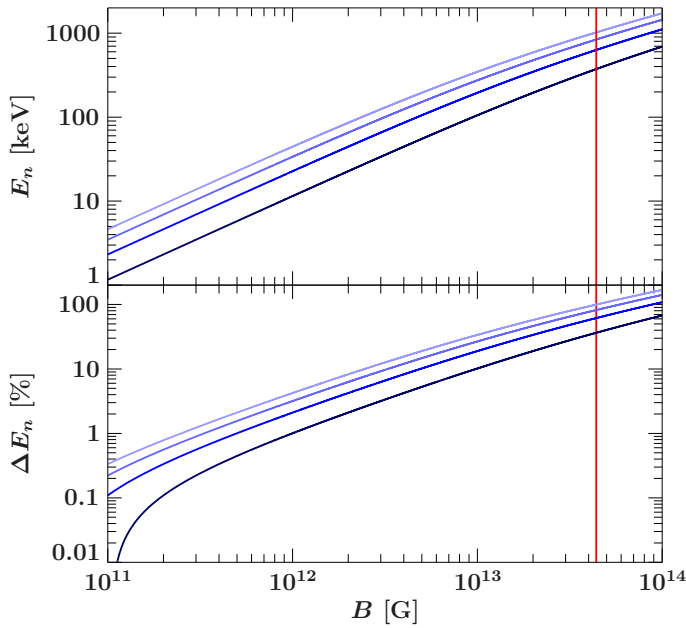
Figure 2.14: Top: *B*-field strength against Landau energy. For the calculation of E_n, I used Eq. 2.13 and set $\theta = \pi/2$ and $z = 0$. Bottom: percentage deviation of the result from the 12-*B*-12 rule (Eq. 2.14) from the exact value for E_n (Eq. 2.13), as $\Delta E_n = (E_n^{12B12} - E_n)/E_n$. The curves show the Landau levels for $n = 0$ to 3 (from dark blue to cyan, respectively). The vertical line shows the position of B_{crit}.

and the width of a CRSF. Coburn (2001) demonstrate that for typical cyclotron centroid energies between $\sim 10\,\mathrm{keV}$ and $\sim 50\,\mathrm{keV}$, the respective values for the Gaussian widths range between $\sim 1\,\mathrm{keV}$ and $\sim 10\,\mathrm{keV}$.

Time-consuming numerical simulations based on QED reveal complex shapes of CRSFs, which strongly depend on the viewing angle and on the physical properties of the plasma (e.g., Schönherr et al., 2007; Schwarm, 2010, and references cited therein). Figure 2.15 shows examples of these complex shaped cyclotron features which result from Monte Carlo simulations. These simulations show that even emission humps in the wings of cyclotron lines are possible. These humps are caused by electron spawning, i.e., the deexitation of an electron to a lower Landau level, which leads to the emission of a photon. Due to relativistic effects, the energy of this photon is slightly shifted, resulting in the appearance of these wings. Although the line shapes of CRSFs are a powerful tool to study the physical conditions in the cyclotron line forming region, in many cases, the instrumental resolution of X-ray spectra is not high enough to resolve the complicated shapes of CRSFs. As a consequence, CRSFs are often modeled by simple Gaussian absorption features (see Eq. 2.9). A more sophisticated yet phenomenological model for cyclotron lines was suggested by Mihara et al. (1990). Here, the broadband continuum is multiplied by a pseudo-Lorentzian profile, given by

$$\mathbf{CYCLABS}(E) = \exp\left(-\frac{\tau(WE/E_{\mathrm{cyc}})^2}{(E - E_{\mathrm{cyc}})^2 + W^2}\right), \tag{2.15}$$

with the centroid energy, E_{cyc}, the width of the feature, W, and the optical depth of the line, τ.

As discussed in Sect. 2.4 and illustrated in Fig. 2.7, the behavior of the X-ray emission height strongly depends on the X-ray luminosity with respect to the critical luminosity. Since different emission heights correspond to different magnetic field strengths, CRSFs are expected to show variations in their centroid energies. Corresponding to different luminosity regimes, as explained in Sect. 2.4, different groups of accreting X-ray pulsars regarding to the cyclotron line energy's behavior are expected(Becker et al., 2012, and references cited therein):
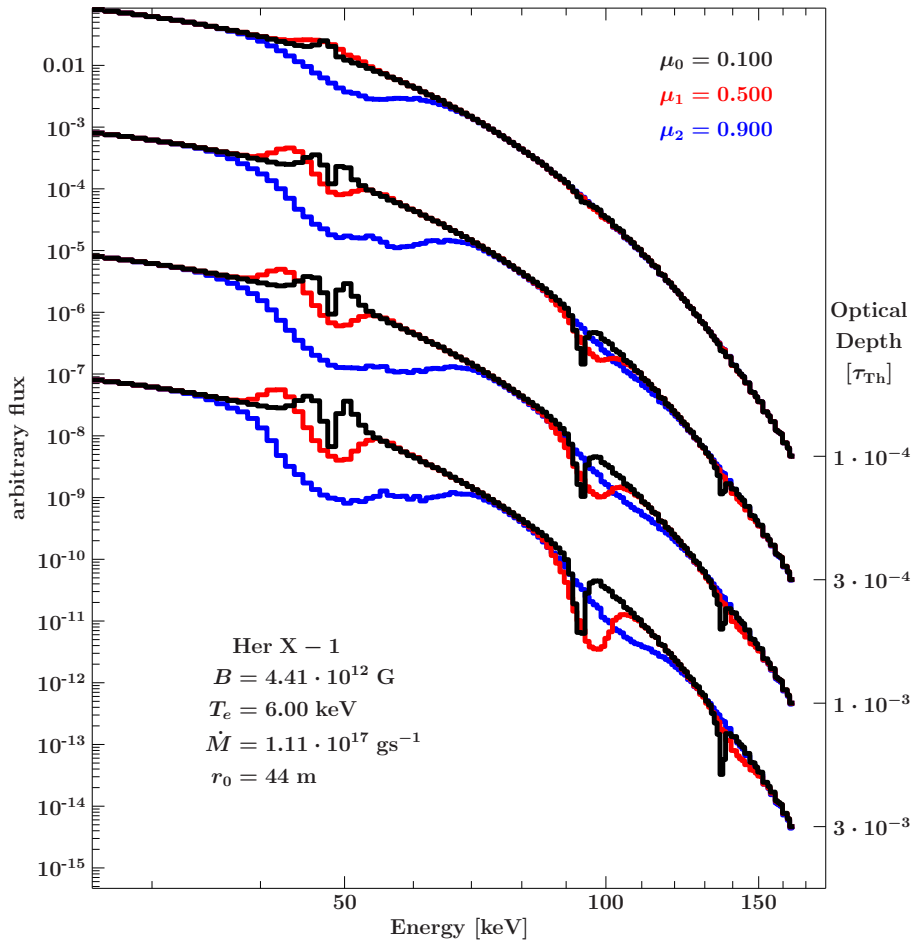
Figure 2.15: Monte Carlo simulated cyclotron-continuum hybrid model spectra with typical parameters (Becker & Wolff, 2007) for a comparison with the system Her X–1. The four sets of curves shifted in y-direction correspond to an optically thin plasma (upper curves) towards an optically thick plasma (lower curves). Different colors correspond to different viewing angles $\mu := \cos\theta$. The Figure was kindly provided by Fritz-Walter Schwarm.

- **Positive correlation between E_{cyc} and L_{X}**

  For certain luminosities, theory predicts an increase of the cyclotron emission height with increasing luminosity, i.e., a correlation between E_{cyc} and L_{X}. As suggested by Staubert et al. (2007) and verified by Becker et al. (2012), this is the case for X-ray pulsars which accrete within the subcritical luminosity regime. With Her X-1, Staubert et al. (2007) found a cyclotron source which shows this behavior.

- **Negative correlation between E_{cyc} and L_{X}**

  The opposite behavior, i.e., a decreasing cyclotron emission height with increasing luminosity, is expected to be observed for cyclotron sources which accrete in the supercritical luminosity regime. For example, V 0332+53 shows this behavior (Tsygankov et al., 2006; Klochkov et al., 2011b). Initially, 4U 0115+634 was assumed to be a further example of this class of sources (e.g., Nakajima et al., 2006; Müller et al., 2010). However, as I show in this thesis, this assumption is caused by an erroneous modeling of the broadband continuum and has to be revised.

- **Constant** E_{cyc}

  At intermediate luminosities, the emission height is assumed to be rather constant with changing luminosities. As a consequence, the respective sources are expected to show a relatively stable cyclotron line energies. For example, A 0535+26 shows a cyclotron line around 45 keV (Caballero et al., 2013), without evidence for variability.

Note that besides this picture there are alternative theories explaining the energy variation of cyclotron line. Recently, Mukherjee & Bhattacharya (2012) suggested that changes in the cyclotron line energy could be also due to the distortion of the local magnetic field of an accretion mound.

Given that the centroid energies of CRSFs, strongly depend on the luminosities of the sources, a time averaged analysis covering, e.g., a complete outburst of CRSFs might be problematic. The possibility of the variation of cyclotron energies could lead to the superposition of temporal varying features resulting in too broad and unphysical shapes in the time averaged spectra. Studying cyclotron line features should be therefore done time resolved and the spectra should be added only, if variations of the features can be excluded. Beyond the temporal variability of cyclotron line parameters, the strong viewing angle dependence of the cyclotron lines induces other variabilities on timescales of the order of the pulse periods of neutron stars. To account for this type of variability, spectra covering certain pulse phases should be analyzed separately. In many cases, the quality of the spectra is not sufficient to allow for such analyses (see, e.g., most spectral parameters of XTE J1946+274, as discussed in Sect. 4). For some other cases, significant variations over the pulse phase have been indeed detected (e.g., Cen X-3, Suchy et al., 2008).

2.8 Timing Properties of Accreting Pulsars

A NALYZING the pulsed emission of the radiation from X-ray pulsars, as described in Sect. 2.5, allows for studying the rotational period, P_{pulse}, of the neutron star as well as its temporal evolution. The physical processes behind these effects are described briefly in this Section.

2.8.1 Changes of the Rotational Period

The material from the optical companion couples to the magnetic field lines and corotates with the neutron star. The conservation of angular momentum implies a change of the rotation of the neutron star during this process. This change occurs either in a spin-up or in a spin-down of the neutron star, both on short timescales of the order of days, but also on larger timescales of the order of years. Additionally, there are sources which show a mixture of these behaviors. A summary of representatives of all of these types of P_{spin}-changes is given in the introduction of Lovelace et al. (1995).

Theoretical attempts to model the changes in the pulse period were performed by Ghosh et al. (1977), Ghosh & Lamb (1979), Lovelace et al. (1995), and others. Ghosh & Lamb (1979) found a relation between the pulse period of the neutron star P_{pulse}, its time derivative $\dot{P}_{\mathrm{pulse}}$, and the X-ray luminosity L_{X} for accretion from a disk. Shakura et al. (2012) presented a model for quasi-spherical accretion and apply this model to the systems GX 301–2, Vela X-1, and GX 1+4. This model successfully

describes the spin-up/spin-down measurements of these systems on long, but also on short timescales.

2.8.2   The Propeller Effect

Once the accreted matter within the Keplerian accretion disk approaches the Alfvén radius, the magnetic field becomes the dominant force, which determines the motion of the material. In the case that the Keplerian velocity of the matter exceeds the rotational velocity of the magnetic field lines, i.e.,

$$\frac{2\pi R}{P_\mathrm{spin}} < \sqrt{\frac{GM_\mathrm{ns}}{R}}, \tag{2.16}$$

the material is forced to co-rotate with the neutron star (see, e.g., Kreykenbohm, 2004, and references therein) and can be accreted onto the neutron star's poles. Otherwise, the material is expelled from the system and no accretion is possible (Illarionov & Sunyaev, 1975). This so called *Propeller Effect* prevents the formation of accretion columns and leads to the quiescence of X-ray binary pulsar candidates. White (1989) proposed that the total quiescence of some systems near periastron is caused by this effect and gave an expression for the lowest possible X-ray luminosity, where accretion can occur. These thresholds were observed for the sources GX 1+4 and GRO J1744–28 (Cui, 1997), and even the skip of one or more pulses in GX 301–2 might be caused by the propeller effect (Kreykenbohm et al., 2010).

2.8.3   Quasi-Periodic Oscillations

For the sake of completeness, I explain an interesting effect concerning mainly LMXBs with relatively low *B*-field strengths. For Sco X-1, van der Klis et al. (1996) found sub-millisecond oscillations ("quasi periodic oscillations", or simply QPOs) at frequencies around $\sim 800\,\mathrm{Hz}$ and $\sim 1100\,\mathrm{Hz}$. Furthermore, these authors found that these, in the power spectrum of Sco X-1 twin peaked frequencies, are linearly correlated with the already known low-frequency QPOs at 6–20 Hz (van der Klis, 1989), and showed a change of their strength with flux. Zhang et al. (1998) performed a long-term study of the X-ray light curve of 4U 1820–30 and found that the low-frequency QPO and the kHz QPO frequencies increase almost perfectly parallel with increasing flux, until a saturation effect sets in at a certain flux level. To date, there are several theoretical models to describe the phenomenon of QPOs (for a summary of these models and QPOs in general, see the lectures of Jörn Wilms[3], on which the discussion of QPOs in this thesis is based):

- **Beat Frequency Model**

  One possible explanation of QPOs are resonance effects between the Keplerian orbits of the material in the accretion disk, and the spin frequency of the neutron star (see, e.g., Strohmayer et al., 1996; Erkut & Alpar, 2004, and references cited therein). In this scenario, there are two preferred radii: the Alfvén radius and the radius where the Keplerian velocity exceeds the sonic speed. The spin frequency of a clump near the Alfvén radius can be modulated by the spin frequency of the neutron star. This explains the low-frequency QPOs. The high frequency QPOs are explained by the latter radius (Lamb & Miller, 2001). In

---

[3]http://pulsar.sternwarte.uni-erlangen.de/wilms/teach/index.html

this scenario, the faster frequency of the twin oscillations is caused by a bright footprint on the neutron star's surface, which is caused by a clump rotating close to the sonic speed with the frequency ν_{sonic}. This footprint irradiates further clumps in the disk with the frequency of the neutron star's rotation ν_{spin}, leading to the slower twin oscillation with the beat frequency between of ν_{spin} and ν_{sonic}.

- **Relativistic Precession Model**

  Stella & Vietri (1998) proposed another model, which is based on relativistic effects. In this model, the respective frequencies are caused by a wobble of the orbital plane caused by relativistic frame dragging (called *Lense-Thirring precession*, after Lense & Thirring, 1918).

QPOs are a promising tool to achieve a better insight into the nature of neutron stars, i.e., their fundamental parameters as mass, radius, B-field, as well as their equations of state. However, none of the theoretical models is able to describe all observed quantities of QPOs, which remain even today an open question. Nonetheless, even National Aeronautics and Space Administration (NASA) stated that "The kHz QPOs are the most important scientific result to date of *RXTE* [...].".

Chapter 3

X-ray Observatories and Instruments

S INCE the discovery of X-rays by Wilhelm Conrad Röntgen in the year 1895 in Würzburg, many practical applications using this radiation have been established. X-ray scattering techniques are used by, e.g., solid state physicists for structural analyses. In medicine, X-rays are an indispensable tool to look inside living bodies without opening them. Last, but not least, X-rays allow us to see into the hot universe, yielding new mysteries of the universe as well as their solutions. In this Section, I describe the basics of instruments which make X-rays from astronomical objects visible and the respective techniques. At the end of this Section, I give an introduction to the instruments used for the analyses in this work.

Observations of X-rays, especially from extraterrestrial sources, come along with many problems and difficulties. Compared to optical light, X-rays hardly interact with most materials. To focus this kind of radiation is not possible with common lenses or mirrors made out of glass or plastics. More elaborated techniques have to be used for this task. Another problem with observing the sky in X-rays is the high opacity of the Earth's atmosphere concerning this radiation. While for some wavelength ranges the atmosphere is transparent, e.g., for optical wavelengths or radio waves, X-ray photons are more or less completely absorbed before they can reach Earth bound observatories. To study this radiation, the respective telescopes have to be located above the atmosphere. Therefore, X-ray telescopes have to be aboard of satellites orbiting the Earth.

3.1   Observing X-rays in the Sky

I N this Section, I explain the basic technologies used for observations of astronomical X-ray sources, i.e., the methods to detect and to focus this radiation.

3.1.1   Collimators

The basic functionality of a collimator is quite easy: a set of tubes with opaque side walls, which are arranged side by side, allows incoming X-rays only from a narrow field of view (FoV), which is typically of the order of $1°$ (Fürst, 2011), to pass through.
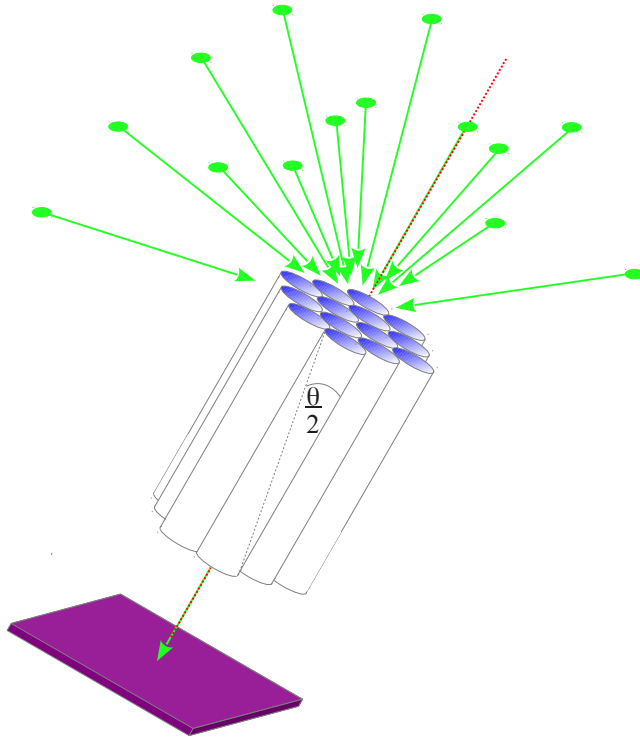
Figure 3.1: Schematic sketch of a collimator. Only the incoming X-rays (green) with an angle to the optical axis (red, dashed) less than $\theta/2$ can pass through the collimator and are detected by the CCD (purple).

These X-rays get detected by, e.g, a CCD or a proportional counter behind the collimator. As illustrated in Fig. 3.1, this field of view has an opening angle θ. An example for an instrument with a honeycomb structured collimator was the HEXTE aboard the *RXTE* (Rothschild et al., 1998).

One of the great advantages of collimators are the relatively low costs. On the other hand, however, collimators in combination with proportional counters cannot distinguish between several sources within their FoV, making such an instrument inapplicable for crowded fields.

3.1.2 Wolter Telescopes

As shown in, e.g., Fürst (2011), and references cited therein, ordinary lenses and mirrors, as applied for visible light, do not work for X-rays. X-rays rather get dispersed by materials as, e.g., gold, which are, for X-rays, even optically thinner than vacuum. This problem complicates the task of focussing X-rays the "traditional" way. However, Wolter (1952) had the innovative idea to use the threshold angle, θ_c, for total reflection

$$\theta_c = \arcsin\left(\frac{n_{\text{thin}}}{n_{\text{dense}}}\right), \tag{3.1}$$

if radiation propagates from an optical denser medium with the refractive index n_{dense} towards a thinner medium with n_{thin}, to focus X-rays (e.g., Aschenbach, 2009). Initially thought to be applied to microscopes, this idea means to use mostly two subsequent sets of nested mirror shells to focus a parallel incoming X-ray beam via two reflections. Giacconi & Rossi (1960) developed this idea further to construct telescopes for X-rays (the basic idea behind Wolter telescopes is displayed in Fig. 3.2).
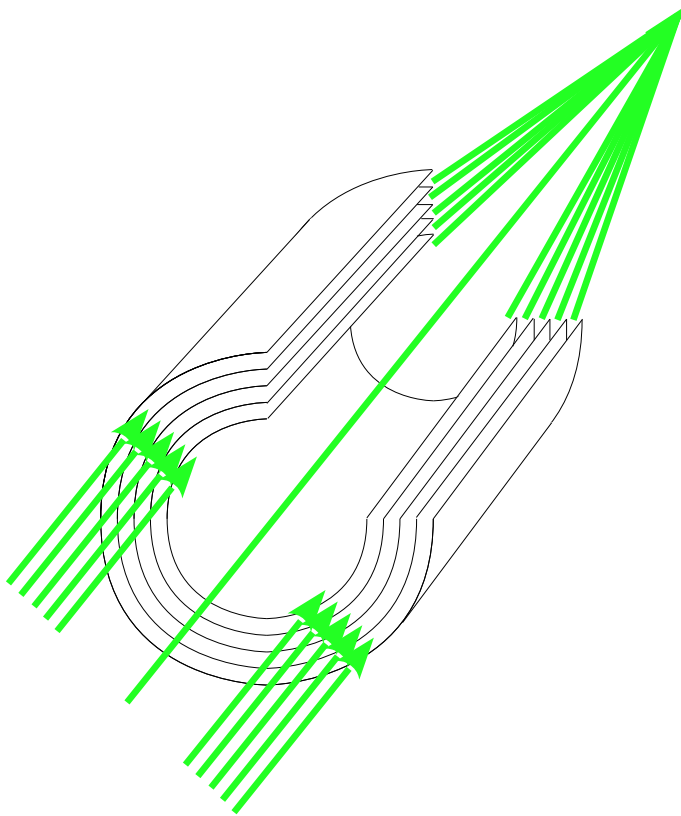
Figure 3.2: Schematic sketch of a Wolter telescope.

3.1.3 Coded Mask Instruments

Another way to observe the sky in X-rays, especially for higher energies, is using coded mask instruments. Here, a mask with opaque pixels is placed on top of a CCD detector. Incident X-rays lead to an X-ray shadow of the mask on the detector, allowing for the determination of the angular position of the respective X-ray source. In the case of many X-ray sources in the FoV with different luminosities, the situation is a bit more complicated. Then, the CCD detects a mixture of shadows from all X-ray sources. For two sources, this situation is schematically displayed in Fig. 3.3. The mathematical process to calculate the positions of the sources and their luminosities using the shadow-mixture is very complex and comes along with various problems and possible sources of errors. E.g., the "deconvolution" process could lead to fail-detections of sources ("ghosts"). The use of catalogues with the positions of well known sources is an opportunity to simplify the deconvolution. A great advantage of coded mask instruments is the large FoV compared to collimators or Wolter telescopes and the possibility to observe many sources simultaneously.

3.2 *The* Standard Candle for X-ray Astronomy: The Crab

C ONTRARY to optical astronomy, most sources in the X-ray sky are highly variable, even on timescales shorter than minutes and seconds. Therefore, it is problematic to find standard candles for high energy astronomy up to γ-rays, to be able to calibrate instruments and compare luminosities. However, the *Crab* has turned out to be a good candidate for this purpose (see, e.g., Kirsch et al., 2005, for a review). This source is the remnant of a supernova explosion, which was observed in the year
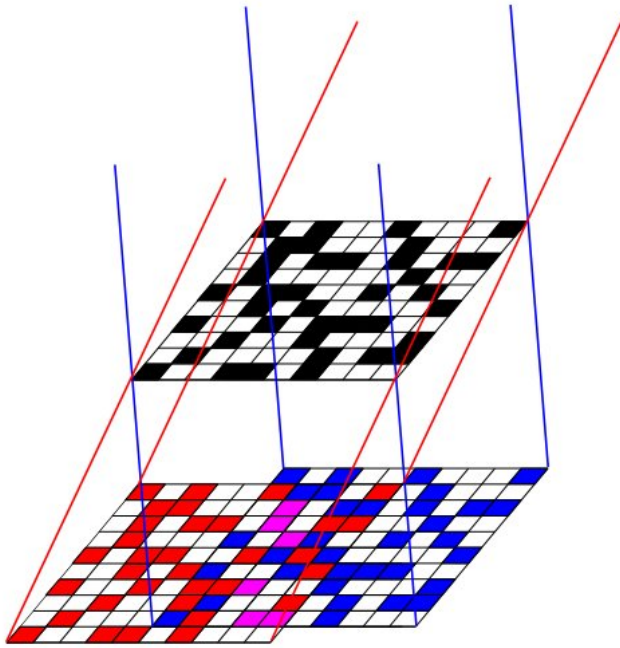
Figure 3.3: Schematic sketch of a coded mask instrument with the resulting shadow mixture of the incident X-rays of two sources.

1054 by Chinese astronomers. This supernova was visible for the naked eye even during daytime.

With a diameter of a few light years (e.g., Green et al., 2004), the Crab nebula's (see Fig. 3.4) X-ray flux, which is caused by synchrotron emission of electrons ejected from the pulsar into the nebula, should be constant on timescales of the order of years. The only possibility for short time variabilities is the pulsar NP 0532 centered in the planetary nebula. However, Toor & Seward (1977) excluded strong intensity variations and described the spectrum of the Crab as an absorbed (see Sect. 2.6.2.1) power-law

$$I(E) \propto E^{-\Gamma}, \tag{3.2}$$

where I denotes the differential energy flux and $\Gamma = 2.1$. Note that, even today, the details of the spectral shape are discussed controversely and Wilson-Hodge et al. (2011) showed that the flux of the Crab shows fluctuations over time.

The Crab is not only used for calibration issues, but also for comparing fluxes. Besides the standard cgs units, the "mCrab" was established as one of the most common unit for fluxes. If using this unit, it is very important to additionally give the respective energy band. This is often neglected, even by professional astronomers. Due to a possibly different spectral shape between the Crab and the source of interest, the flux compared to the Crab is strongly dependent on the energy band.

3.3 From Events to X-ray Spectra and Light Curves

THE basic tasks for X-ray observatories are, besides imaging, the recording of X-ray light curves and spectra, i.e., gaining the number of incident photons per time, area, and energy interval. In optical astronomy, spectra are recorded by the usage of dispersive elements like gratings or prisms, splitting a polychromatic light into its spectral colors, which are finally detected by a CCD chip. A calibration lamp with spectral emission peaks at well known energies is then used for the wavelength

Figure 3.4: Combined picture of an optical (*Hubble*, red) and X-ray (*Chandra*, blue) image of the Crab nebula (Credit: NASA, Hester et al.).

calibration of the measured spectrum. In X-ray astronomy, the way to gain the source spectrum from the measured count rates is, for many instruments, different and much more complicated. Good descriptions of this process, on which this Section is based, are given, among others, by Hanke (2007, 2011), Fürst et al. (2011a), the talk "X-ray spectral analysis" by Mike Nowak[1] and for a more mathematical treatment, Davis (2001).

An incident X-ray photon produces a charge cloud within the CCD, which is read out periodically, or within a proportional counter. The respective event is characterized by the pulse height amplitude (PHA) of the voltage signal from the read out charge. Tagging this signal with time allows for the generation of light curves. The range of the PHA is binned into discrete channels h with respective count numbers $C(h)$ and Poisson distributed uncertainties $\sqrt{C(h)}$. The relation between the resulting "channel-count rate spectrum" and the real source spectrum $S(E)$ in units of photons $\mathrm{s}^{-1}\,\mathrm{cm}^{-2}\,\mathrm{keV}^{-1}$ measured between the times T_1 and T_2 is given by the integral equation

$$C(h) = B(h) + \int_0^\infty dE \int_{T_0}^{T_1} dt\, R(h,E) \times A(E) \times S(E,t), \qquad (3.3)$$

with the following components:

- **Redistribution Matrix Function (RMF) $R(h,E)$:**

  Caused by instrumental issues, incident photons with the same energy do not necessary fall into the same PHA channel. For example, incident X-ray photons could be possibly absorbed by atoms of the detector gas which get ionized. Subsequent fluorescence photons with a certain energy cause so called "escape peaks" at lower energies than the incident photon in the detected spectrum. The unitless RMF gives the probability that an incident photon with an energy

---

[1]http://www.black-hole.eu/index.php/schools-workshops-and-conferences/
1st-school-on-multiwavelength-astronomy/schedule

E is detected by the data channel h. Note that the RMF is usually a non-linear function and is, due to detector degradation (e.g., because of high energy particle bombardment), changing with time. These temporal changes can be studied through observations of standard candles, as for example, the Crab nebula (see Sect. 3.2).

- **Ancillary Response Function (ARF)** $A(E)$**:**

  Differences in the reaction between incident photons with the detector material and/or the mirror shells lead to an energy dependent effective area. This information, in units of cm^2, is stored within the ARF. Since the effective area depends furthermore on the off-axis angle, the ARF has to be calculated separately for each observation.

- **Background counts** $B(h)$**:**

  Observed X-ray spectra are affected by instrumental background. This background, $B(h)$, is caused by the instrument or by cosmic rays and not always accounts for the X-ray background in the sky from, e.g., emission from hot gas, diffuse emission by interstellar gas, or the emission of the galactic ridge (see Sect. 2.6.2.3). For a correct analysis of the data, these background contributions should be added to the source spectrum model. There are two possible ways to handle the background $B(h)$. One possibility is to measure the background directly. The other way is to use satellite specific background models. As described in the following Sections, both ways are realized in several X-ray observatories. Sometimes, background models are not sufficient to describe observations. In these cases, a background scaling constant, c_b, is often introduced to solve this problem.

3.3.1 Problems with X-ray Spectra

Even though all X-ray observatories provide up-to-date RMF files, ARF generation tools, and background models, some further effects possibly cause trouble when analyzing X-ray spectra. Some examples of these effects are discussed in this Section.

One possible problem is the so-called *pile-up* effect. Given that the count rate of an observed X-ray source is large enough that the mean time between two events becomes comparably to the read out time, two or more incident photons within one read out process and spatial segment of the CCD are mis-interpreted as one photon with a PHA that is roughly the sum of the incident photons (see, e.g., Davis, 2003; Schmid, 2012, and references cited therein). The consequences are a systematic decrease of the number of total counts and a shift of the spectrum towards higher energies. To correct for this effect, satellite specific models can be used or affected regions on the CCD with high count rates can be excluded from the data extraction process.

Another problem, which often occurs, is the *gain shift* (see, e.g., Duro et al., 2011, and references cited therein). Here, charge clouds in the CCD-detector are not read out completely and remain in the CCD until subsequent read outs. This effect leads to a systematic shift of the spectrum towards higher energies. Alternatively, because of impurities of the CCD-detector, charge could possibly get lost, which leads to a systematic shift of the energies towards lower values. To identify this problem, spectral features at well known energies can be used to modify the RMF of the observation, respectively.

3.3.2 ISIS: The Tool to Analyze X-ray Data

Most of the data analyses presented in this work have been performed with the *Interactive Spectral Interpretation System* (ISIS; Houck & Denicola, 2000). This is an *S-Lang* based package and besides *XSPEC* (Arnaud, 1996) one of the most commonly used software developed for the analysis of X-ray spectra, light curves, as well as for other scientific data sets.

Since Eq. 3.3 cannot easily be solved for the source spectrum, spectral fits performed with ISIS are based on the minimization of the model $M(E)$ dependent χ^2 with

$$\chi^2 = \sum_h \left(\frac{[C(h) - B(h)] - C_M(h)}{\sqrt{C(h) + B(h)}} \right)^2 , \qquad (3.4)$$

where $C_M(h)$ denotes the forward folded model spectrum, mostly defined as $C_M(h) = t_{\exp} \int_0^\infty dE \ R(h, E) A(E) M(E)$. The expression $[C(h) - B(h)]$ represents the background corrected measured spectrum, $\sqrt{C(h) + B(h)}$ the Poisson error of the background corrected measured spectrum, and $t_{\exp}$ the exposure time. For a detailed discussion about ISIS, the fitting process, and χ^2 statistics, see, e.g., Hanke (2007), and references therein.

3.4 The *Rossi X-ray Timing Explorer*

THE introduction of the instruments given in this and the subsequent Sections are mainly based on Kühnel (2011), Fürst et al. (2011a), and references cited therein. From its launch on 1995 December 30 from Cape Canaveral (Florida), until its decommission in 2012 January, NASA's *Rossi X-ray Timing Explorer* (*RXTE*; named after the Italian Astronomer Bruno Rossi) was one of the most successful X-ray missions with great outcomes for science. The satellite orbited the Earth every ∼90 min at an altitude of 580 km with an inclination of 23° (see Goddard Space Flight Center's, or short, GSFC's, web page[2]). The main goal of the *RXTE* mission was the study of the variability of the X-ray sky down to scales of a thousandth of a second simultaneously with spectral properties in the energy range between 2 keV and 250 keV. For example, millisecond pulsars (e.g., Chakrabarty et al., 2003) were studied with the *RXTE* as well as black hole X-ray binaries (e.g., Grinberg et al., 2013) and even faint sources such as Seyfert galaxies (e.g., Markowitz et al., 2009). The three main instruments aboard the *RXTE* are described in the next Sections. A schematic sketch of the *RXTE* is displayed in Fig. 3.5. The *RXTE* will re-enter the Earth's atmosphere some day between 2014 and 2023[3].

3.4.1 The All-Sky Monitor

The *All-Sky Monitor* (ASM) regularly monitored the highly variable X-ray sky to detect the inset of outbursts of transient sources. Furthermore, the ASM allowed for long-term studies of various X-ray sources. As described by Levine et al. (1996) and on the web page of the GSFC[4], the ASM consisted of three Scanning Shadow Cameras (SSCs), which were mounted on a rotation drive and moved every 90 s. Two of the three SSCs looked into the same direction with an angular difference of ±12°. The

---

[2]http://heasarc.gsfc.nasa.gov/docs/xte/XTE.html
[3]http://www.spaceflightnow.com/news/n1201/09rxte/
[4]http://heasarc.gsfc.nasa.gov/docs/xte/asm_products_guide.html
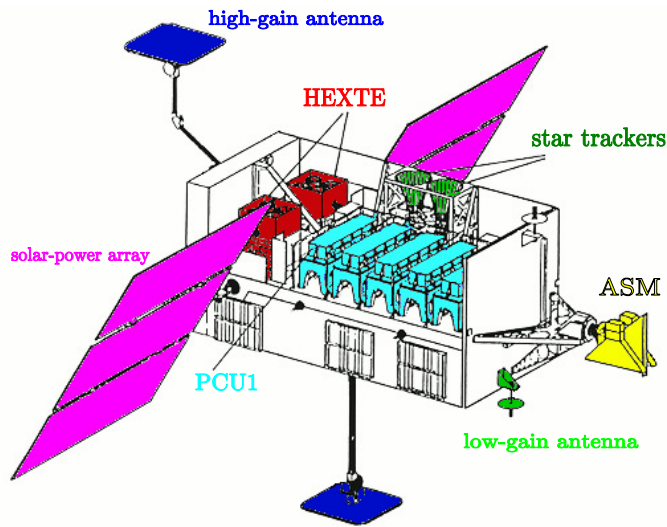
Figure 3.5: Sketch of the *RXTE* with its main scientific instruments. The picture has been taken from the web page of the GSFC and modified.

third camera looked into the direction of the ASM drive-axis. Each SSC was provided with a slit mask with a FoV of about $6° \times 90°$. The SSCs were sensitive at energies between 1.5 keV and 12 keV and provided data of three energy bands (1.5–3 keV, 3–5 keV, and 5–12 keV). The effective area of each SSC was 30 cm^2 at 5 keV. The X-rays were absorbed in a Xe-CO$_2$-gas mixture and detected by carbon-coated quartz fiber anodes. Note that ASM data which were collected after 2010 January might be affected by an erroneous calibration (Grinberg et al., 2013; Vrtilek & Boroson, 2013).

3.4.2 The Proportional Counter Array

The Proportional Counter Array (PCA) was an instrument which covered the spectral energy range between 3 and 50 keV and a timing accuracy of the order of microseconds (Jahoda et al., 2006, and references cited therein). In contrast to many other instruments, the PCA was not an imaging, but a photon counting instrument. The $1°$ FoV of the PCA was defined by the full width at half maximum of the diffraction pattern of the collimator. The PCA consisted of five identical large-area proportional counter units (PCUs, labeled with the numbers 0–4), each with an effective area of about 1300 cm^2 (Glasser et al., 1994). An incoming X-ray photon induced a current of electrons towards anodes within the gas chamber, which was filled with a gas mixture of xenon and methane. The Xe/methane-chamber was divided into three layers with independent anode chains with a voltage of ~ 2000 V (Jahoda et al., 2006). The released electrons ionized gas molecules on their way to the anode and produced a cascade of electrons, proportional to the energy of the incident X-ray photon. However, in some cases, the gas molecule got not completely ionized by the electron, but only excited. Since the subsequently produced fluorescence photon would have been led to another cascade, the detector gas was mixed with methane, absorbing these fluorescence photons without getting ionized. The timescales of these processes were of the order of μs, defining the high time resolution of this instrument (Knoll, 2010). The energy calibration of the PCA was performed with the α-emitter ^{241}Am with a characteristic line at 59.6 keV (Jahoda et al., 2006).

As common for X-ray instruments, the PCA was affected by background problems. This noise originated from cosmic rays, particles, and from the activation of heavy elements in the housing of the detector. These effects became strongest when the satellite passed the South Atlantic Anomaly (SAA; Fürst et al., 2009, and references

cited therein), which is a region above the Atlantic ocean close to the coast of Brazil, where the cosmic particle rate is above average. The high voltage of the anodes was lowered or was even turned off during and after the passage of the SAA. Data taken during the passage are often excluded from analyses. Far away from the SAA, where the background is relatively low and predictable, the background of the PCA was modeled. Regular comparisons between the modeled and the measured background verified the background model (Jahoda et al., 2006).

Due to technical issues of the detector it is sometimes necessary to extract data from individual PCUs, because the PCUs were shut down periodically. In many cases only PCU2 is used, because this PCU is known to be the best calibrated one (Jahoda et al., 2006). Impact events in 2000 May and 2006 December[5] led to problems with the propane layers on top of the xenon layers of PCU0 and PCU1. Since these propane layers were used to identify background events, the background values of the affected PCUs were higher after these impacts.

Besides the exclusive extraction of single PCUs, one can furthermore choose between data from all three layers of the PCU, or from the top layer. Since for soft photons, about 90% of the counts are detected by the top layer, it can be useful for dim and soft sources to reduce the background rate[6].

3.4.3 The High Energy X-ray Timing Experiment

The High Energy X-ray Timing Experiment (HEXTE; Rothschild et al., 1998) was the other main instrument aboard the *RXTE* and sensitive between 15 and 250 keV. Its FoV was, similar to the PCA, defined by a collimator with an opening angle of $1°$. To allow for simultaneous observations, PCA's and HEXTE's FoVs were congruent. The HEXTE consisted of two clusters, A and B, each with four phoswich scintillation detectors. These consisted of a sodium iodine crystal doped with thallium (NaI(Tl)), located between two layers of sodium-doped cesium-iodine (CsI(Na)) crystals. An X-ray photon entering the NaI(Tl) crystal excited a certain number of electrons which was proportional to the energy of the photon. These electrons induced the emission of fluorescence photons entering a photo multiplier tube, where they were amplified and finally resulted in a measurable current. The two CsI(Na) layers which covered the NaI(Tl) crystal had two functions: 1.), the lower one acted as a guide to transfer the scintillation photons from the NaI(Tl) crystal into the photo multiplier and 2.), using the different decay times of the scintillation pulses in the NaI(Tl) and CsI(Na) layers, they acted as an anti-coincidence shielding identifying background photons which did not originate from the FoV. The energy calibration was, similar to the PCA, performed with an ^{241}Am source, located in the FoV of the HEXTE.

A fundamental difference between the HEXTE and the PCA was the background determination process. For the HEXTE, the background was measured directly via the so called "rocking mechanism": while the zero positions of cluster A and B were co-aligned, each cluster rocked every 16 s between the zero position and an off-center position $3°$ away from the source. The off source positions of the two clusters were perpendicular to each other and allowed for an almost real-time measurement of the X-ray background. According to GSFC's homepage[7], technical problems led to the stop of the rocking mechanisms of cluster A in 2006 October. Since then, cluster A

---

[5]http://heasarc.gsfc.nasa.gov/docs/xte/whatsnew/big.html
[6]http://heasarc.gsfc.nasa.gov/docs/xte/recipes/layers.html
[7]http://heasarc.gsfc.nasa.gov/docs/xte/whatsnew/newsarchive_2006.html#_hexteA-norock
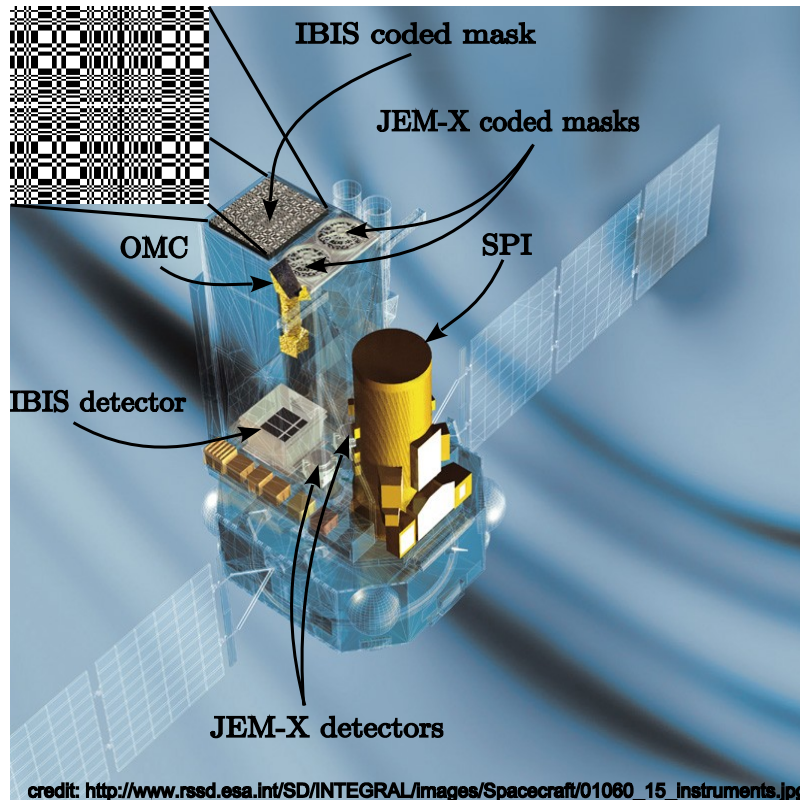
Figure 3.6: Sketch of the *INTEGRAL* satellite with its main scientific instruments. The picture as well as the inset which shows the coded mask of IBIS have been taken from ESA's web page and were modified after Winkler et al. (2003).

of the HEXTE resided within zero position collecting data as usual, however, with no background measurement any more. Since cluster B underwent similar problems in 2009 December, it had been fixed into off-source position since then[8]. The simultaneous source-background-observation of the clusters A and B basically allowed for recording and background-correcting spectra, however, the differences of the two clusters implied uncertainties of the background up to 10% (Pottschmidt et al., 2006), making studies of weak spectral features in the HEXTE band very problematic and, in some cases, even impossible.

3.5 The *International Gamma-Ray Astrophysics Laboratory*

ANOTHER observatory for X-rays is European Space Agency's (ESA's) *International Gamma-Ray Astrophysics Laboratory* (*INTEGRAL*; for overviews of the mission, see, Winkler et al., 2003; Winkler, 2012). *INTEGRAL* observations are performed using a coded mask (see Sect. 3.1.3). The main scientific instruments aboard *INTEGRAL* are the spectrometer aboard *INTEGRAL* (SPI; Vedrenne et al., 2003), for γ-ray spectroscopy between 15 keV and 10 MeV, and the Imager onboard the *INTEGRAL* Satellite (IBIS; Ubertini et al., 2003), for mainly high resolution imaging between 15 keV and 10 MeV. Furthermore, *INTEGRAL* is equipped with two monitors: JEM-X (Lund et al., 2003), for the X-ray band between 3 keV and 35 keV, and the OMC (Mas-Hesse et al., 2003), for the *V*-band. Figure 3.6 shows an artist's view of the *INTEGRAL* satellite and its instruments.

---

[8]http://heasarc.gsfc.nasa.gov/docs/xte/whatsnew/newsarchive_2010.html#hexteb.1

Since its launch on 2002 October 17 from Baikonur (Kazakhstan), *INTEGRAL* orbits the Earth with a period of 72 hrs and an inclination of 52.2°. The high eccentricity of the satellite leads to a change in the distance to Earth between 9000 km and 154 000 km (Winkler et al., 2003). This orbit allows for long monitoring observations without large changes in background or other disturbing factors as, e.g., the passage of the SAA. Even though *INTEGRAL* has originally been planned to work for only two years with a possible extension to five years, the satellite is, even today, more than ten years after launch, in orbit and provides data.

In this Section, I set the focus on IBIS, the instrument aboard *INTEGRAL*, which is used for the analyses presented in this work.

3.5.1   Imager on-board the *INTEGRAL* Satellite

The description of IBIS in this Section is based on Ubertini et al. (2003) and Fürst (2011). As displayed in Fig. 3.6, this instrument consists of a coded mask above two detectors, the *INTEGRAL* Soft Gamma-Ray Imager (ISGRI; Lebrun et al., 2003), for the energy band between 15 keV and 1 MeV, and the PIxelated Cesium Iodide Telescope (PICsIT; Labanti et al., 2003), for energies between 170 keV and 10 MeV.

ISGRI is a CdTe camera with eight independent modules with an energy resolution of about 8% at 60 keV and an effective area of $\sim$2621 cm^2. Since each pixel of ISGRI is connected to the read-out electronics, this detector can act comparably fast in the order of tenth of microseconds.

3.6   *Swift*

THE main scientific task for NASA's *Swift* satellite is the detection and follow-up observations of the enigmatic gamma-ray bursts (GRBs; e.g., Costa et al., 1997). A summary of *Swift* and its instruments is given in Gehrels et al. (2004), Barthelmy et al. (2005), and Krauß (2013), on which this Section is based. An artist's view of *Swift* is displayed in Fig. 3.7.

Swift was launched on 2004 November 20 from Cape Canaveral (Florida) and orbits the Earth circularly at an altitude of $\sim$600 km and an inclination of $\sim$20°. *Swift* has three main instruments: the Burst Alert Telescope (BAT; Gehrels et al., 2004; Barthelmy et al., 2005), the X-ray Telescope (XRT; Gehrels et al., 2004; Burrows et al., 2005), and the ultraviolet and optical telescope (UVOT; Gehrels et al., 2004). BAT is sensitive between 15 keV and 150 keV and searches for the onsets of GRBs. Besides the gamma-ray related science, BAT performs a complete monitoring of the hard X-ray sky regularly. Once BAT has detected the inset of a GRB, follow-up observations with the XRT are triggered. This instrument is a Wolter telescope which is sensitive in the energy band between 0.2 keV and 10 keV. The optical telescope aboard the *Swift* satellite, the UVOT, is co-aligned with the XRT and has six bandpass filters covering the wavelength range between 1700 Å and 6500 Å.

In this Section, I focus the discussion on BAT and the XRT, the two instruments, which have been used in this work.

3.6.1   The Burst Alert Telescope

A detailed discription of the BAT, on which this Section is based on, is given in Gehrels et al. (2004). BAT's detector with an area of 5240 cm^2 consists of 32 768 pieces
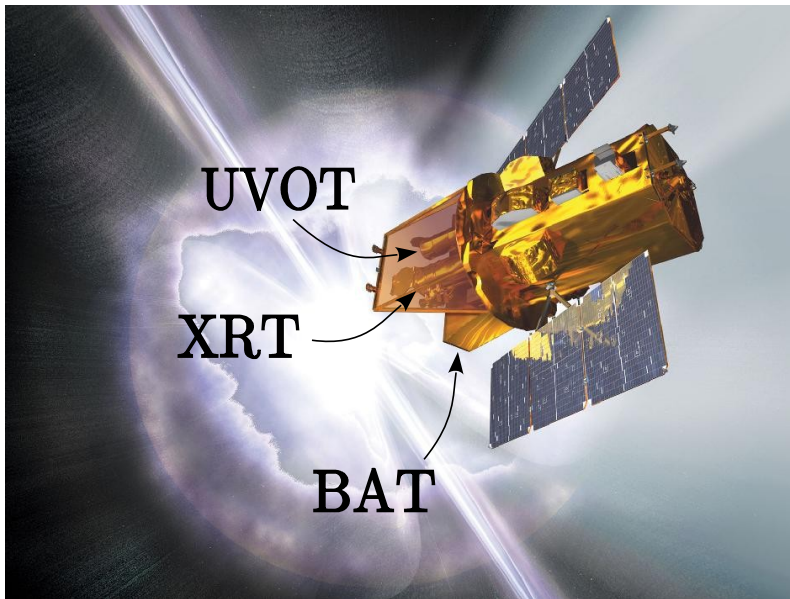
Figure 3.7: Artist's view of the *Swift* satellite catching a GRB with its main scientific instruments. The picture has been taken from NASA's web page and was modified after Gehrels et al. (2004).

of CdZnTe and is located 1 m behind a coded mask and covers a FoV of $100° × 60°$. Detector calibration is performed by a tagged ^{241}Am source. The background is minimized by a shield which surrounds the coded mask and the detector. This shield consists of multiple layers of lead, tantalum, tin, and copper.

The primary scientific task of BAT is the detection and observation of GRBs. Once the BAT has detected the inset of a GRB, software decides whether this event is worth to interupt the currently ongoing observation. This software accounts for many criteria as, e.g., the time interval of the increase of the countrate or the respective energy range. Furthermore, it checks whether the flux increase is caused by a point source, as expected for a GRB. The threshold for triggering a GRB is typically $8σ$ above background noise. If this is the case, position and intensity of the GRB candidate is immediately sent to Earth and the satellite slews towards the GRB.

Besides the detection of GRBs, BAT provides a hard X-ray all sky survey[9]. Comparing these real time data with an onboard source catalogue allows for the detection of the insets of outbursts of X-ray transients as, e.g., X-ray binary pulsars.

3.6.2 The X-ray Telescope

The XRT has an effective area of $110 \, cm^2$, a FoV of $23'$, a resolution of $18''$, and is sensitive in the 0.2 keV–10 keV energy band. It is a focusing Wolter telescope, designed for the observation of GRBs. More detailed descriptions of the XRT can be found in Gehrels et al. (2004), Burrows et al. (2005), and Krauß (2013). Besides providing light curves, this instrument measures also fluxes and X-ray spectra.

3.7 *Suzaku*

L AUNCHED on 2005 July 10, Japan Aerospace eXploration Agency's (JAXA's) Astro-EII was successfully brought into orbit, after its progenitor, Astro-E, was lost about five years earlier (Mitsuda et al., 2007). Astro-EII was renamed *Suzaku*, which

---

[9]http://heasarc.nasa.gov/docs/swift/results/transients/
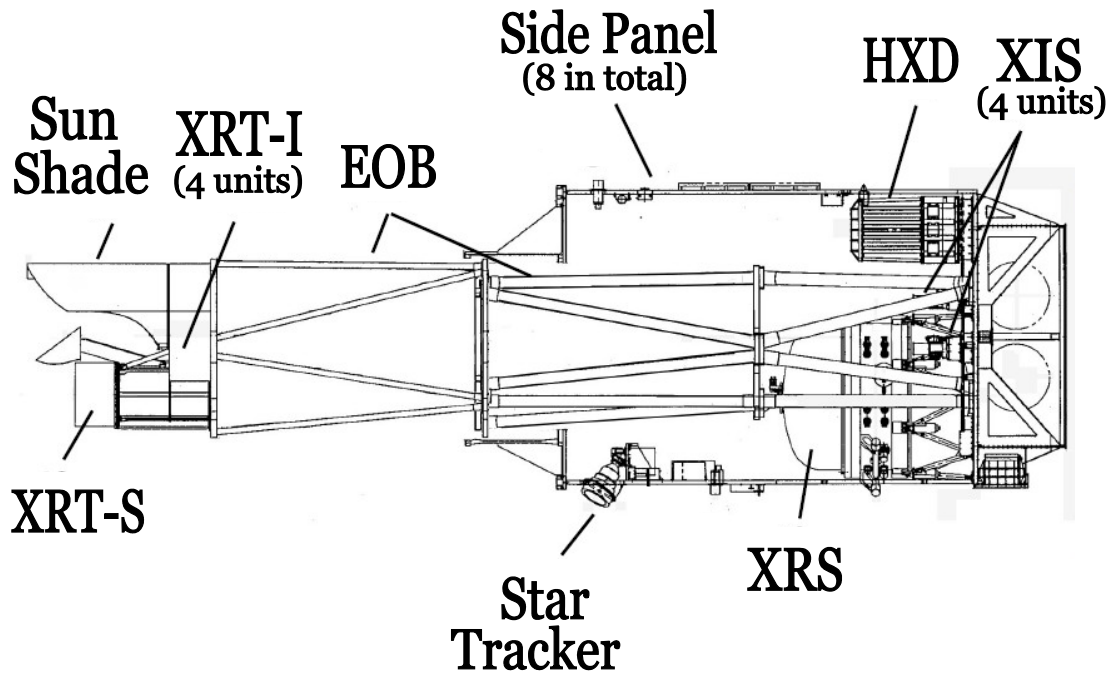
Figure 3.8: Schematic sketch of the *Suzaku* satellite with its main instruments. The picture has been taken from Mitsuda et al. (2007) and modified.

is in Japan's mythology one of the four guardian animals, a red bird, protecting the southern skies. It is a joint mission between JAXA and NASA. *Suzaku* is in a circular orbit around the Earth, with 570 km altitude, 31° inclination, and an orbital period of about 96 min (Mitsuda et al., 2007).

A main scientific instrument aboard *Suzaku* is the X-ray Imaging Spectrometer (XIS; Koyama et al., 2007), for soft X-rays below $\sim$12 keV. The XIS is located at the focal plane of the X-ray Telescope (XRT; Serlemitsos et al., 2007). Another instrument is the Hard X-ray Detector (HXD; Takahashi et al., 2007), for the hard energy band up to $\sim$600 keV. A schematic picture of *Suzaku* and its main instruments is displayed in Fig. 3.8.

3.7.1   The X-ray Telescope and the X-ray Imaging Spectrometer

Aboard *Suzaku*, five XRTs are installed (Mitsuda et al., 2007; Serlemitsos et al., 2007). These Wolter-type telescopes are focussing X-rays in the 0.2 keV–12 keV energy band and have a FoV of up to 17'. Each XRT's effective area is typically 440 cm^2 at 1.5 keV, and 250 cm^2 at 8 keV. The XIS (Mitsuda et al., 2007; Koyama et al., 2007) is a silicon CCD detector, which is located at the focal plane of the XRT and operates in a photon-counting mode. A charge clouds produced by an incident X-ray photon leads to a detectable voltage level which is proportional to the energy of this photon. There are four sets of XIS aboard the satellite, which are labelled with numbers 0–3. While one of the four sets is working with a back-illuminated CCD (XIS1), the other three sets use front-illuminated CCDs. Because of calibration problems around the Si- and Au-edges, Nowak et al. (2011) suggested to omit the energy bands 1.72 keV–1.88 keV and 2.19 keV–2.37 keV.

"Catastrophic damage on 2006 November 9", as GSFC's homepage[10] states, led to the failure of XIS2. This homepage also reports on further anomalies concerning XIS0 and XIS1, probably caused by micrometeorite impacts.

3.7.2 The Hard X-ray Detector

The HXD (Mitsuda et al., 2007; Takahashi et al., 2007) is the instrument aboard *Suzaku* for the hard X-ray band between $\sim 10\,\mathrm{keV}$ and $\sim 600\,\mathrm{keV}$. This non-imaging instrument uses a collimator, consists of 16 main detectors and is surrounded by 20 scintillators for active shielding. The effective area of this instrument is about $\sim 160\,\mathrm{cm}^2$ at $20\,\mathrm{keV}$, and $\sim 260\,\mathrm{cm}^2$ at $100\,\mathrm{keV}$. The HXD consists of two types of detectors. One is the PIN, sensitive below $\sim 60\,\mathrm{keV}$. The other detector is the GSO, a phoswich counter which is sensitive above $\sim 30\,\mathrm{keV}$. Due to an insufficient signal-to-noise ratio (S/N), I omit the GSO from the analysis presented in this thesis.

---

[10]http://heasarc.gsfc.nasa.gov/docs/suzaku/analysis/abc/node8.html

Chapter 4

The Reawakening of the Transient X-ray Pulsar XTE J1946+274

I N this Section I report on a series of outbursts of the high-mass X-ray binary XTE J1946+274 in 2010/2011 observed with *INTEGRAL*, *RXTE*, and *Swift*. This work has already been published in the journal *Astronomy & Astrophysics* (Müller et al., 2012) and the text of this Section, as well as the Figures, and parts of Sect. 7 are mainly based on this publication (partly literally, partly analogously). Almost all parts of the work presented within this Section have been performed by myself. One exception is the data extraction of the *INTEGRAL* data, which was performed by Isabel Caballero (CEA Saclay, France). The epoch folding, yielding the pulse period, on which the pulse phase resolved spectra are based on, was performed by Matthias Kühnel. I use the "We"-style in the next Sections (the same holds for Sects. 5 and 6).

4.1 Introduction

T HE 15.8 s pulsar XTE J1946+274 was first detected in 1998 (Smith & Takeshima, 1998; Wilson et al., 1998). It is a transient X-ray source with a Be-type companion (Verrecchia et al., 2002). The initial outburst of XTE J1946+274 in 1998 lasted for about three months. Heindl et al. (2001) reported on the discovery of a CRSF at an energy near 35 keV during this outburst, which was followed by several fainter outbursts separated by $\sim$80 d (Campana et al., 1999). This separation was later established by Wilson et al. (2003) as half of the $\sim$170 d orbital period. The occurrence of two outbursts per orbit could be related to the misalignment of the Be-star's angular momentum and the orbital plane of the neutron star. While we look nearly onto the pole of the Be-star, the orbital inclination is $\gtrsim$46° (Wilson et al., 2003).

After a phase of nearly periodic flaring between 1998 and 2001, XTE J1946+274 went into quiescence until 2010 June, when a new sequence of outbursts started (see, e.g., Müller et al., 2010b). The principal outburst behavior in 2010 was the same as that observed in the 1990s, with two outbursts per orbit. However, the five outbursts seen during 2010 are neither clearly connected to the times of periastron and apastron passages (based on the orbital ephemeris from Wilson et al., 2003), nor to any other specific orbital phase. This new outburst episode ended in 2011 June
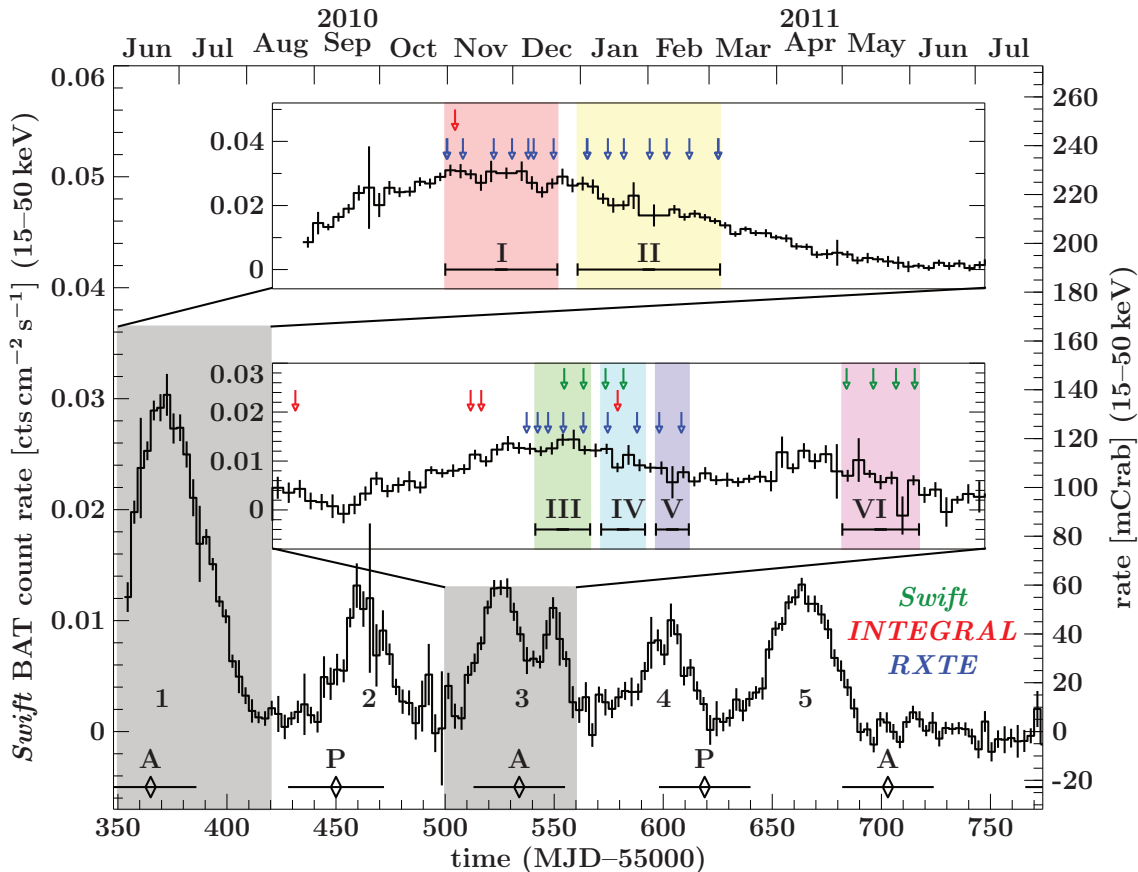
Figure 4.1: 15–50 keV *Swift*/BAT light curve of the 2010/2011 outburst series. The times of periastron and apastron passages are marked by P and A, respectively. These epochs and the corresponding uncertainties were calculated using the orbital solution from Wilson et al. (2003). The insets provide a closer view on the first (Jun/Jul) and the third (Nov/Dec) outburst. The blue, red, and green arrows in these insets indicate the observations times for PCA, ISGRI, and XRT, respectively. Epochs over which data were summed for the time resolved spectral analysis are indicated with I to VI.

and the source was back in quiescence at the time of writing.

In this work, we report on *INTEGRAL*, *Swift*, and *RXTE* observations of the first and the third outburst of this series in 2010 June/July and 2010 November/December, respectively.

4.2 Observations and Data Reduction

THE 2010/2011 outburst series started on 2010 June 4, when *Swift*/BAT detected an increase of the X-ray flux of XTE J1946+274, rising to 40 mCrab (15–50 keV) within three days (Krimm et al., 2010). This first outburst lasted about 60 d and reached a flux of ~140 mCrab (see Fig. 4.1). The subsequent four outbursts lasted between 30 and 50 d each, reaching almost the same maximum flux level between 40 and 60 mCrab. The separation of the outbursts is between 60 and 90 d. A peculiar behavior was observed during the third outburst where the primary maximum was followed by another brightening, reaching again luminosities of up to ~50 mCrab (Fig. 4.1, inset).

We present data from the *RXTE*'s PCA, *INTEGRAL*'s ISGRI, and *Swift*'s XRT. Data were reduced with our standard analysis pipelines, based on HEASOFT (v. 6.10 and 6.11) and *INTEGRAL* OSA v. 9.0. XTE J1946+274 was monitored by *RXTE* regularly during the first and the third outburst. The source was also sporadically in the field of view of *INTEGRAL* during the first and the third outburst. *Swift* pointings were available only during the main and secondary peak of the third outburst. Table 4.1 contains a log of the observations with these satellites, which are also indicated in Fig. 4.1.

Since PCU2 is known to be the best-calibrated one (Jahoda et al., 2006), only data from the top layer of this PCU were used (see Sect. 3.4.2). We obtained 2–60 keV light curves with 0.125 s resolution, spectra in the **standard2f** mode, and pulse-phase-resolved spectra using **GoodXenon** data. The light curves were corrected to the barycenter of the solar system using **faxbary**[1]. The PCA background model **SkyVLE** was used for PCA background subtraction. Due to large uncertainties in the orbital parameters (Wilson et al., 2003) no correction could be performed for the neutron star's orbital motion. The lack of sufficient statistics prevented us from improving the existing orbital solution. Data from the High Energy X-ray Timing Experiment (HEXTE, Rothschild et al., 1998) onboard *RXTE* were excluded from our analysis since both HEXTE clusters were not rocking at the time of the observations. The resulting uncertainties in the background determination are too large for the purposes of this work.

The CdTe detector of *INTEGRAL*/ISGRI (see Sect. 3.5.1) covers the energy range from $\sim$18 keV to 1 MeV (Lebrun et al., 2003). Thanks to the large field of view of *INTEGRAL*, XTE J1946+274 was detected several times during its recent outbursts between 2010 June and 2011 April in observations pointed at Cyg X-1. We extracted ISGRI pulse-phase-averaged spectra for all observations of XTE J1946+274 using the standard spectral extraction method of OSA 9 described in the *INTEGRAL* documentation[2]. We selected those observations of XTE J1946+274 for which it was less than $12°$ off-axis.

To cover the soft X-ray band we used data from *Swift*/XRT, a 600×600 pixel CCD covering a field of view of $23\overset{\prime}{.}6 \times 23\overset{\prime}{.}6$ in the energy range 0.2–10 keV (see Sect. 3.6.2). We extracted the data in windowed timing mode. For the source region we chose a circle around the source with a radius of $\sim 1'$. The background was extracted using circles of the same radius at two off-source positions about $2\overset{\prime}{.}5$ away from the source.

In the spectral analysis, we used data between 1.5 keV and 7.0 keV for XRT. We binned the XRT and PCA data to a S/N of ten. Due to calibration problems of the PCA at the Xe L-edge, we excluded PCA data below 4.5 keV from our analysis. Discarding bins with S/N<10 results in an upper energy limit of typically 40 keV for the PCA. ISGRI covers the high-energy band between 20 keV and 100 keV. We added a systematic error in quadrature to the PCA and the ISGRI spectra using canonical values of 0.5% and 2.0%, respectively (see Jahoda et al., 2006, and the IBIS analysis user manual)

---

[1] http://heasarc.gsfc.nasa.gov/lheasoft/ftools/fhelp/faxbary.txt
[2] http://www.isdc.unige.ch/integral/analysis#Documentation

Table 4.1: Summary of all observations used.

ID[a]	start date (2010)	MJD	t_{exp} [s]	cts[b] [10^5]	epoch[c]
01-00	Jun 20	55367.12–55367.14	1584	2.92	I
01-01	Jun 20	55367.18–55367.20	1408	2.52	I
01-02	Jun 21	55368.69–55368.77	4080	7.69	I
01-03	Jun 24	55371.74–55371.78	2880	5.37	I
02-00	Jun 26	55373.50–55373.61	5776	10.51	I
02-03	Jun 28	55375.14–55375.17	2800	5.04	I
02-01	Jun 28	55375.66–55375.70	3184	5.62	I
02-02	Jun 30	55377.62–55377.66	3200	5.36	I
03-00	Jul 03	55380.89–55380.92	2000	3.06	II
03-01	Jul 03	55380.96–55380.99	3056	4.61	II
03-02	Jul 05	55382.92–55383.02	6368	8.96	II
03-03	Jul 07	55384.48–55384.59	5872	7.82	II
04-00	Jul 10	55387.03–55387.13	6144	7.46	II
04-01	Jul 11	55388.73–55388.77	3184	3.65	II
04-02	Jul 13	55390.95–55390.99	3200	3.37	II
05-00	Jul 16	55393.77–55393.80	3248	3.08	II
05-01	Jul 16	55393.83–55393.85	1392	1.28	II
06-02	Nov 23	55523.19–55523.23	2640	2.35	—
06-01	Nov 24	55524.17–55524.24	3200	2.65	III
06-00	Nov 25	55525.15–55525.17	1392	1.21	III
07-00	Nov 26	55526.54–55526.56	2000	1.76	III
07-01	Nov 28	55528.36–55528.39	2656	2.35	III
07-02	Nov 30	55530.58–55530.62	2928	2.29	IV
08-00	Dec 03	55533.26–55533.30	3168	2.38	IV
08-01	Dec 05	55535.28–55535.31	2432	1.64	V
08-02	Dec 07	55537.31–55537.34	2624	1.60	V
938	Jun 20	55367.46–55368.44	45174	16.98	I
983	Oct 31	55500.76–55503.45	35224	−0.20	—
988	Nov 18	55518.04–55518.16	4125	0.13	—
989	Nov 18	55518.71–55519.42	10940	1.83	—
993	Nov 30	55530.67–55532.35	54470	6.94	IV
001	Nov 26	55526.60–55526.66	2475	0.13	IV
002	Nov 28	55528.39–55528.47	2630	0.12	IV
003	Nov 30	55530.39–55530.48	2424	0.12	V
004	Dec 02	55532.00–55532.08	1442	0.07	V
005	Dec 22	55552.49–55552.57	2600	0.10	VI
006	Dec 24	55554.77–55554.98	1838	0.05	VI
007	Dec 26	55556.90–55556.97	663	0.01	VI
008	Dec 28	55558.31–55558.99	2110	0.05	VI

[a] For PCA (blue), the first column contains the number of the Obs-ID after 95032-12- and for XRT (green) after 0031888. For ISGRI (red) the revolution number is listed. [b] Total background corrected counts. [c] Epoch for data grouping, see text for details. ObsIDs without assignment in this column are different enough to other spectra during the same epoch that they cannot be combined with the other data or they were recorded without simultaneous low-energy measurements. We therefore excluded these data from our analysis.

4.3 Spectral Analysis

W E performed all fits using the *Interactive Spectral Interpretation System* (ISIS, Houck & Denicola, 2000). To improve the S/N of individual spectra, we averaged the data over six data blocks in time, taking into account the flux level and instrument availability. These epochs I–VI are defined in Table 4.2 and shown in Fig. 4.1. The spectra in epochs I and II cover the first outburst at the maximum and fading phase, respectively. Epochs III–V follow the maximum and the fading phase of the third outburst. The flux in the maximum level of this outburst (epoch III) is comparable to the fading phase of the first outburst (epoch II). The last set of observations is summarized in epoch VI. These XRT data cover the fading phase of the flare immediately after the third outburst. Before defining these epochs we confirmed that the spectral variability during these epochs is negligible.

4.3.1 Spectral Model

As shown in Sect. 2.6.1 and by, e.g., Becker & Wolff (2007), the X-ray spectra of accretion-powered X-ray pulsars can be roughly described by a power-law with a high energy cutoff. In practical data modeling, this continuum has been approximated by several different continuum models (see, e.g., Kreykenbohm et al., 2002, and Sect. 2.6.1, for a summary). Here we describe the data using the so called Fermi-Dirac cutoff (**FDCUT**, Tanaka, 1986), given by Eq. 2.8. This continuum is modified by the CRSF, modeled as a line with a Gaussian optical depth profile $G = \exp(-\tau(E))$, with $\tau(E)$ as defined in Eq. 2.9. The equivalent width of this feature is denoted with W_{CRSF} in the following. The spectra of some X-ray pulsars, including XTE J1946+274, also contain an absorption- or emission-like feature in the range 8–12 keV (Coburn, 2001). The origin of this so-called 10 keV feature is still unclear; however, since it appears always at about the same energy, it is probably not related to the magnetic field strength of the neutron star. We modeled this feature as a broad Gaussian absorption feature, which we also did for the CRSF (Eq. 2.9) with the centroid energy, E_{G}, the width, σ_{G}, optical depth, τ_{G}, and equivalent width, W_{G}. Finally, interstellar absorption was modeled with as described in Sect. 2.6.2.1.

In modeling the data, we took into account that the cross-normalization of the different instruments used is not entirely known and the source might also slightly change in flux between the different observations. These effects were taken into account by cross calibration constants c_{XRT} and c_{ISGRI}, using the PCA as the reference instrument. Furthermore, the PCA background was allowed to vary slightly in count rate. To account for these imperfections in modeling the background, we introduced the constant c_{b}.

Finally, the data modeling was affected by the proximity of the source to the plane of the Galaxy. Galactic ridge emission (see Sect. 2.6.2.3) manifests itself through an emission feature at $\sim$6–7 keV in the PCA spectrum caused by unresolved Fe Kα fluorescence lines. These lines are not present in the XRT data in epochs III and IV and therefore must be caused by diffuse emission that is picked up by the PCA only, owing to its larger field of view. In our modeling of the PCA data we therefore introduced a model for the Galactic ridge emission based on that of Ebisawa et al. (2007), who described the ridge emission as the sum of two bremsstrahlung components and an iron line complex modeled by three Gaussian lines at 6.4 keV, 6.67 keV, and 7.0 keV, with equivalent width ratios of 85:458:129, respectively. Since we used the PCA data down to 4.5 keV only, we did not account for the two soft bremsstrahlung components and

modeled the Galactic ridge emission as the sum of three narrow Gaussians, with fixed energies and equivalent-width ratios according to Ebisawa et al. (2007). This component was applied only to the PCA data and absorbed by the interstellar medium using the Galactic N_H as determined from the Leiden/Argentine/Bonn (LAB) Survey of Galactic H I, $N_H = 9.4 \times 10^{21}$ cm^{-2} (Kalberla et al., 2005). We determined the flux of the Galactic ridge emission from simultaneous fits to the XRT and PCA data from epochs III and IV. In epoch IV, residuals around 6–7 keV are only visible in the PCA, while in XRT neither residuals from this emission, nor from a source-intrinsic iron Kα line are detected. Thus, the residuals in the epoch IV PCA spectrum must be caused by Galactic ridge emission. In epoch III, on the other hand, we find weak evidence for the presence of a source intrinsic iron Kα line in the XRT spectrum. The unabsorbed flux of the 6.4 keV iron line of the Galactic ridge emission in both spectra is consistent with each other (($7.2 \pm 2.0) \times 10^{-5}$ photons s^{-1} cm^{-2}, and $(6.6 \pm 2.0) \times 10^{-5}$ photons s^{-1} cm^{-2} for epoch III and IV, respectively). While these values are slightly higher than the 1.22×10^{-5} photons s^{-1} cm^{-2} reported by Ebisawa et al. (2007), the difference is still within the typical variation of the Galactic ridge emission over the Galactic plane (Yamauchi et al., 2009). Since the flux of the Galactic ridge emission is constant over time, we added this model component with parameters fixed to the mean value as obtained from epochs III and IV to the PCA spectra of all epochs. We find that for the late part of the outburst, the ridge contributes 1.5% of the 3–10 keV flux and 8% in the Fe band (6–7 keV). To estimate the significance of the Galactic ridge emission, we performed Monte Carlo simulations of the best-fit model without this feature to create a set of 1000 synthetic spectra. We then performed the fit allowing all model parameters, including the Galactic ridge emission, to vary. For the two epochs III and IV none of these simulations led to a fake spectrum for which the improvement in χ^2 was as high as in the real data, i.e., the probability that the Galactic ridge emission is real is greater than 99.9 % ($>3.3\sigma$). The remaining residuals at 6.4 keV can be explained by a narrow source intrinsic iron Kα fluorescence line. We modeled this feature by a thin Gaussian emission line with fixed centroid energy $E_{Fe} = 6.4$ keV and width $\sigma_{Fe} = 10^{-4}$ keV. The flux, A_{Fe}, (and thus equivalent width, W_{Fe}) were allowed to vary.

In summary, the model can be written as

$$M = \texttt{tbabs} \times (\texttt{FDCUT} + \text{Fe}_{6.4\,\text{keV}}) \times G_{10\,\text{keV}} \times G_{\text{CRSF}} + \text{GRE}. \qquad (4.1)$$

4.3.2 Time-resolved Spectroscopy

In this Section we describe the time-resolved behavior of the spectral parameters. For each of the six epochs we fitted the respective spectra separately, including the Galactic ridge emission as a constant component as discussed above. Example spectra of two epochs together with the best model fit are shown in Fig. 4.2. The free fit parameters are summarized in Table 4.2 and are displayed in Fig. 4.3. We calculated fluxes in the energy band 10–20 keV for the epochs I–V. In order to be able to compare the source fluxes of all epochs, but avoid excessive extrapolation of the models, we also derived the fluxes in the energy band 7–15 keV. We excluded the contribution from the Galactic ridge emission from this flux.

The resulting χ^2_{red} for all fits does not exceed 1.3 (see Table 4.2). For epoch I, the value of χ^2_{red} is rather high. Here, the highest contribution to χ^2_{red} comes from residuals of the ISGRI data, which are caused by calibration problems, therefore we accept this fit. Not all model components are necessary to describe the data in the

spectra with low statistics, e.g., epoch V provides a statistically too low χ^2_{red} of 0.78. The reason for including these components in these fits even though the components overdetermine the fit model, is that this way it can be shown that these spectra are at least consistent with the full model. In addition, we note that an overestimation of the systematic error would also yield a χ_{red} that is too low. In epoch VI only XRT data are available and the continuum parameters are poorly constrained from these data alone. We therefore fixed E_{fold} and E_{break} to the value obtained from epoch I because a change of these parameters mainly affects energies not covered by XRT. However, possible influences of these fixed parameters to the free fit parameters N_{H} and Γ might affect the results.

The behavior of the photon index, Γ, the cutoff energy, E_{break}, and the folding energy, E_{fold}, yields information about the evolution of the spectral continuum. In most cases there are no or only slight variations of these parameters apparent. However, we know from previous observations that these parameters can also be significantly correlated to each other. We therefore also derived a model-independent illustration of the spectral changes by dividing the background-subtracted PCA spectra from epochs II–V by the spectrum from epoch I (see Fig. 4.4). The ratios II/I, III/I, and IV/I appear to be mainly constants, meaning that the variations of the continuum parameters in epochs I–IV are probably artificial and caused by cross correlations. In contrast to this, ratio V/I shows a spectral softening for epoch V, caused by a real change of the continuum parameters.

Except for epochs covered by XRT, the hydrogen column density N_{H} is poorly determined and the best-fit parameters are consistent with constant N_{H}. In addition to the line caused by Galactic ridge emission, an Fe Kα fluorescence line at 6.4 keV is required during the first outburst and the maximum phase of the third outburst (epochs I–III). The flux of this line is correlated with the X-ray flux of the source, as expected for a fluorescent line. Furthermore, for these epochs at highest luminosities (I–III), the equivalent width W_{Fe} stays roughly constant. In the fading phase of the third outburst and its subsequent flare (epochs IV–VI), this feature is consistent with zero, meaning that the additional emission at these energies can be explained by the Galactic ridge emission. To estimate the significance of the Fe Kα line, we performed similar Monte Carlo simulations as those done for the Galactic ridge emission. For epochs I and II, the probability that there is a source-intrinsic Fe Kα line is greater than 99.9 % ($>3.3\sigma$). During epochs III and IV, where the source was much fainter, these simulations show that the probability for Fe line emission from the source is 98.5% (2.4σ) and 62.0% (0.9σ), i.e., here the Fe line region is dominated by Galactic ridge emission.

We found no evidence for the centroid energy, the width, and the optical depth of the 10 keV feature to be variable over time. Owing to the lack of statistics, the width of the feature, σ_{G}, in epoch III and IV cannot be constrained and was therefore fixed to the mean value obtained from epochs I and II, i.e., $\sigma_{\mathrm{G}} = 2.0$ keV. In epoch V, also owing to the lack of statistics, this feature is not required to describe the data. We therefore omitted it from our model in this epoch, and also from epoch VI, where our coverage reaches only below 7 keV.

One of the most interesting questions is whether there is a cyclotron line as in the 1998 outburst (Heindl et al., 2001). We found a possible CRSF at $\sim$25 keV during epochs I–IV, i.e., the epochs where good coverage exists above 10 keV. The statistics during the maximum of the first outburst (epoch I) are sufficient to obtain CRSF parameters that are well constrained. As is fairly common for CRSF fits (Coburn,
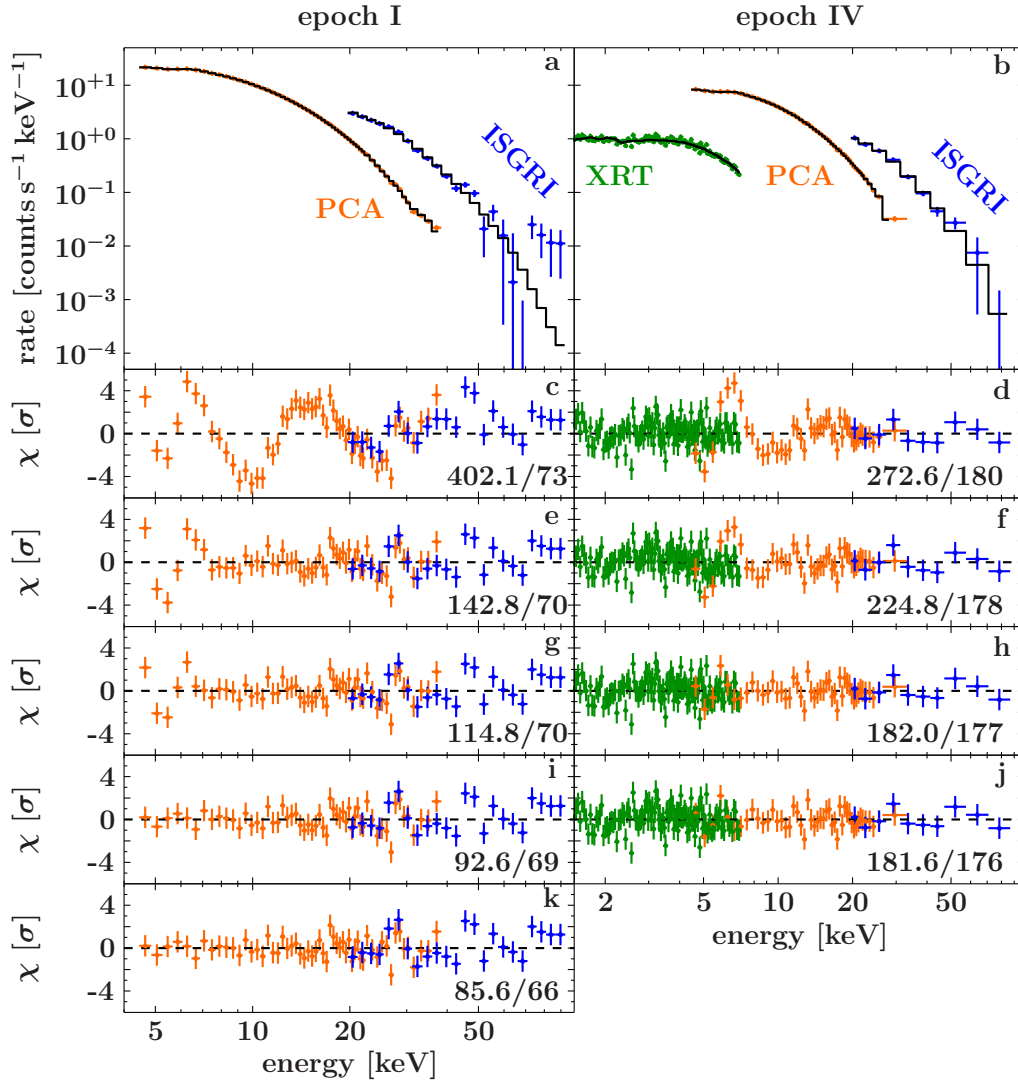
Figure 4.2: Panels a and b show two example spectra of XTE J1946+274. Epoch I is the spectrum with the highest count rate while epoch IV is the only data set for which all instruments are available. Histograms show the best-fit continuum. Panels c–k show the behavior of the residuals when the additional components of the spectral model are added one by one. Numbers at the bottom right of each panel indicate the best-fit statistics, χ^2/dof. c and d: best fit using the Fermi-Dirac cutoff only. e and f: residuals after adding the 10 keV feature to the continuum model. g and h: residuals after adding the Galactic ridge emission to the PCA (for epoch I the flux of this model component was fixed to the result obtained from epochs III and IV). i and j: residuals after adding the Fe Kα line to the model. Since in the model fit of epoch IV the depth of the CRSF is zero, panel j displays the final result for epoch IV. In panel k, the CRSF was added to the data for epoch I. See also text for a discussion of the statistical significances of the Galactic ridge emission, the 10 keV feature, and the CRSF.

Table 4.2: Results of the time resolved spectral analysis.

epoch	start[a]	stop[a]	cts[b]	$F_{10-20\,\mathrm{keV}}$[c]	$F_{7-15\,\mathrm{keV}}$[c]	c_b[d]	χ^2_red/dof
I	367	378	17.20	6.91(2)	8.40(2)	0.943(20)	1.30/66
II	380	394	16.46	4.71(3)	5.72(2)	1.00(7)	1.03/45
III	524	529	2.93	3.03(3)	3.70(2)	0.97(6)	1.17/202
IV	530	534	1.68	2.54(3)	3.17(2)	0.97(4)	1.03/176
V	535	538	1.12	1.88(2)	2.46(2)	1	0.78/32
VI	552	559	—	—	1.69(10)	—	1.21/135

epoch	N_H[e]	Γ	E_fold [keV]	E_break [keV]	c_PCA[d]	c_ISGRI[d]	c_XRT[d]
I	$2.1^{+2.2}_{-2.1}$	$0.75^{+0.09}_{-0.04}$	$7.25^{+0.31}_{-0.30}$	$16.7^{+1.8}_{-2.4}$	1	0.97(3)	—
II	$2.6^{+2.4}_{-2.5}$	$0.82^{+0.14}_{-0.32}$	$6.1^{+1.9}_{-1.0}$	$19.4^{+2.1}_{-9.7}$	1	—	—
III	$1.77^{+0.25}_{-0.29}$	$0.74^{+0.12}_{-0.17}$	$8.0^{+2.4}_{-1.7}$	16^{+4}_{-10}	1	—	0.88(2)
IV	$1.84^{+0.22}_{-0.24}$	$0.74^{+0.09}_{-0.10}$	$8.1^{+0.7}_{-0.6}$	14 ± 4	1	0.88(7)	0.92(2)
V	$5.1^{+2.5}_{-3.3}$	$1.04^{+0.13}_{-0.18}$	$6.0^{+2.6}_{-1.6}$	$19.0^{+1.8}_{-5.6}$	1	—	—
VI	$2.14^{+0.25}_{-0.24}$	0.84 ± 0.08	7.25	16.7	—	—	1

epoch	E_G [keV]	τ_G	σ_G [keV]	E_CRSF [keV]	τ_CRSF	σ_CRSF [keV]	A_Fe[f]
I	$9.85^{+0.20}_{-0.25}$	$0.069^{+0.027}_{-0.016}$	$2.2^{+0.8}_{-0.5}$	$25.3^{+0.9}_{-1.0}$	$0.09^{+0.10}_{-0.07}$	$0.65^{+1.46}_{-0.15}$	10 ± 4
II	$9.9^{+0.4}_{-0.6}$	$0.039^{+0.048}_{-0.018}$	$1.8^{+1.6}_{-1.0}$	25.3	$0.03^{+0.08}_{-0.03}$	0.65	$5.9^{+2.4}_{-2.4}$
III	$9.8^{+0.9}_{-0.7}$	$0.039^{+0.020}_{-0.020}$	2	25.3	≤ 0.23	0.65	1.5 ± 1.0
IV	9.8 ± 0.9	$0.037^{+0.023}_{-0.023}$	2	25.3	≤ 0.40	0.65	$0.4^{+1.0}_{-0.4}$
V	—	—	—	—	—	—	≤ 1.5
VI	—	—	—	—	—	—	≤ 1.0

Uncertainties and upper limits are at the 90% confidence level. Numbers without error bars were held fixed at the values listed. [a]MJD-55000. [b]Total background corrected PCA counts between 7 and 15 keV, in multiples of 10^5. [c]Absorbed flux, in units of 10^{-2} photons s^{-1} cm^{-2}. In epoch VI, the 10–20 keV band is not fully covered by the data and no flux value can be listed. [d]c_PCA, c_ISGRI and c_XRT are defined as the cross calibration and normalization constants for PCA, ISGRI, and XRT, respectively. [e]In units of 10^{22} cm^{-2}. [f]In units of 10^{-4} photons s^{-1} cm^{-2}. The centroid energy has been fixed to 6.4 keV, and the width to 10^{-4} keV.
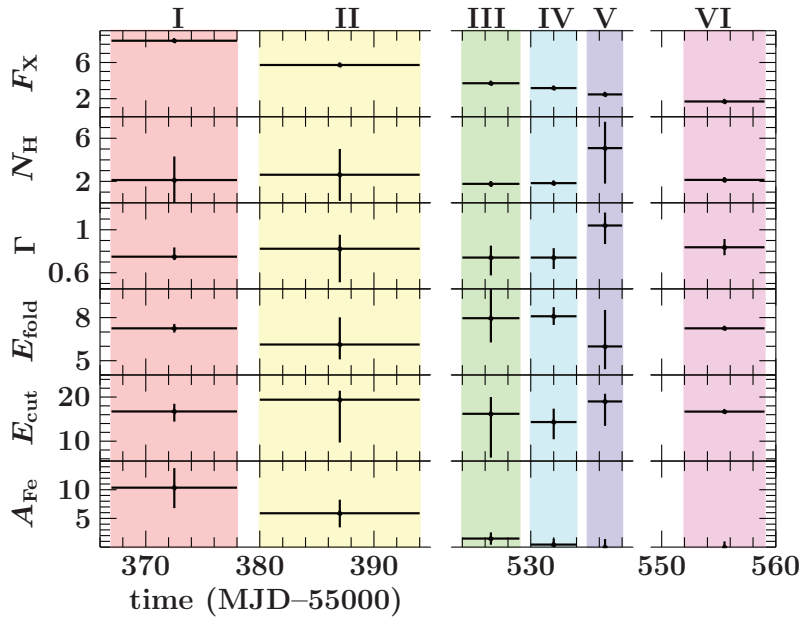
Figure 4.3: Results of time-resolved spectroscopy. The units are as follows: F_X in $10^{-2}\,\mathrm{photons\,s^{-1}\,cm^{-2}}$ in the 7–15 keV energy band, N_H in $10^{22}\,\mathrm{cm^{-2}}$, E_fold and E_cut in keV, and A_Fe in $10^{-4}\,\mathrm{photons\,s^{-1}\,cm^{-2}}$.
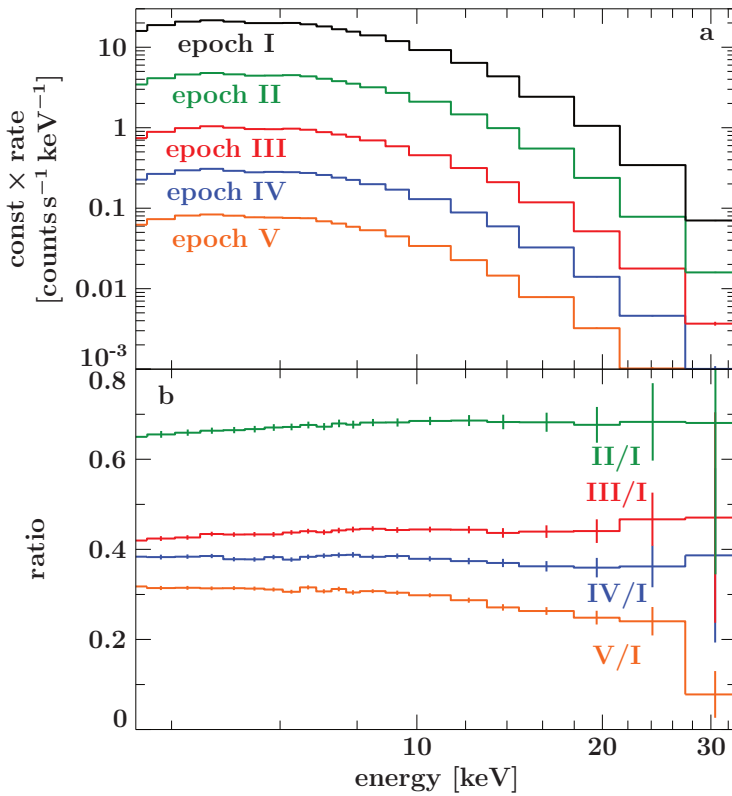
Figure 4.4: a: PCA spectra of time bins I–V (shifted in y-direction for clarity). b: Ratio of the background-corrected time-resolved spectra.
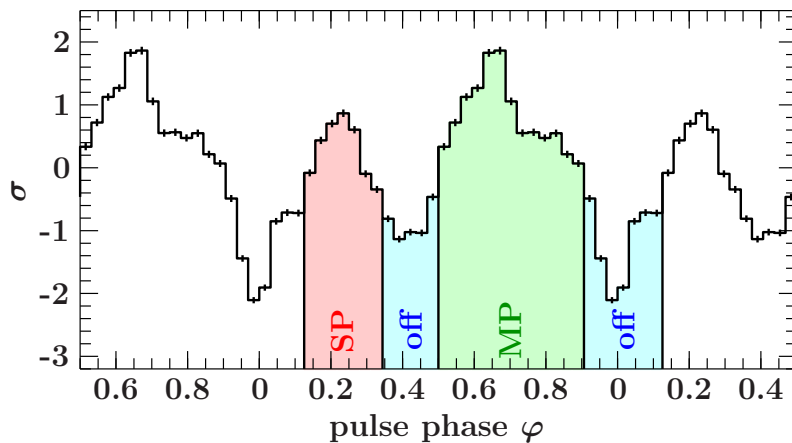
Figure 4.5: PCA-pulse profile of epoch I (in the full PCA energy band, i.e., 2–60 keV), shown twice for clarity. The count rate in each bin is normalized to its variance relative to the mean pulse profile count rate. The phase bins are marked as follows. MP: main peak, SP: secondary peak, off: off state.

2001), the width and depth of the line are strongly correlated. We therefore set a lower limit of 0.5 keV for the width, which is comparable to the resolution of the PCA at these energies. Monte Carlo simulations as described above lead to a 93% (1.81σ) probability that the CRSF found in epoch I is real.

The dependence of the CRSF's parameters to the choice of the approach of modeling the continuum is an important point that has to be discussed as well. The results presented here were obtained by first adding the 10 keV feature to the model, and then accounting for the CRSF. Reversing this procedure for epoch I, we find another minimum of χ^2_{red}, leading to different cyclotron line parameters, i.e., $E_{\mathrm{CRSF}} = 29.6^{+1.6}_{-1.3}$ keV, $\tau_{\mathrm{CRSF}} = 0.34^{+0.12}_{-0.09}$, and $\sigma_{\mathrm{CRSF}} = 6.8^{+1.2}_{-1.7}$ keV. The main problem for this alternative approach is the need of fixing parameters to certain values for the final fit. For example, allowing σ_{CRSF} for the final fit to vary leads to an unrealistically broad CRSF that effectively models part of the exponential rollover and not the line. Furthermore, the quality of this fit is slightly worse ($\chi^2 \approx 97$ vs. $\chi^2 \approx 86$). We note that there is a third solution in which the centroid energy of the CRSF agrees with Heindl et al. (2001). However, in contrast to Heindl et al. (2001), this third solution has an unphysically broad and shallow shape and is thus not physically meaningful. All results presented in this paper are based on the approach of first adding the 10 keV feature, and then the CRSF. Finally, we note that there are two other solutions, in which the CRSF is located at 30 keV and 40 keV and a line width of less than 1 keV. These two solutions are indeed physically meaningful, but a Monte Carlo estimation of the significances of these features yields probabilities of 85% (1.44σ) and 86% (1.48σ), respectively, much lower than for the solution with the CRSF at 25 keV. Furthermore, these two solutions are supported only by about three data bins per instrument (the 40 keV solution even only by ISGRI), while the 25 keV solution is based on a much larger number of spectral bins.

Including a CRSF in the fainter observations in epochs II–IV does not significantly improve the fits. All observations are in principle consistent with the presence of a weak line as that seen in epoch I. Including such a feature in the spectral modeling for consistency, fixing the centroid energy and width, and leaving the optical depth/the equivalent width of the line as a free parameter effectively gives an upper limit for the depth of the line in these observations. As expected, the limit for τ_{CRSF} increases for the fainter phases of the outburst (Table 4.2). We found no evidence for the equivalent width W_{CRSF} to be variable over time.

Table 4.3: Results of the pulse phase resolved spectral analysis.

parameter	MP	SP	off
‚	0.50–0.91	0.13–0.34	0.34–0.50 and 0.91–0.13
Γ	0.87 ± 0.05	$0.49^{+0.10}_{-0.13}$	$0.71^{+0.07}_{-0.09}$
E_{fold} [keV]	6.7 ± 0.4	$7.9^{+0.4}_{-0.5}$	7.8 ± 0.5
E_{break} [keV]	$19.2^{+1.2}_{-1.5}$	11^{+4}_{-5}	$15.0^{+2.4}_{-3.1}$
A^{a}_{Fe} [10^{-4}]	11.9 ± 2.5	$8.7^{+2.8}_{-2.9}$	9.3 ± 2.2
E_{G} [keV]	$9.7^{+0.6}_{-0.7}$	9.5 ± 0.3	9.9 ± 0.2
τ_{G}	$0.034^{+0.015}_{-0.014}$	$0.080^{+0.022}_{-0.020}$	0.114 ± 0.018
τ_{CRSF}	0.12 ± 0.08	$0.04^{+0.09}_{-0.04}$	0.13 ± 0.09
χ^{2}_{red}/dof	0.92/56	1.10/55	0.93/56

Uncertainties and upper limits correspond to the 90% confidence level for one parameter of interest. ^{a}In units of photons $\mathrm{s}^{-1}\,\mathrm{cm}^{-2}$. The centroid energy has been fixed to 6.4 keV, and the width to 10^{-4} keV.

4.3.3 Pulse phase-resolved Spectroscopy

Spectral parameters are known to be variable as a function of pulse phase, e.g., the parameters of cyclotron lines (e.g., 1A 1118−61; Suchy et al., 2011). To investigate these changes, we performed pulse-phase-resolved spectroscopy on epoch I with the PCA, based on a pulse period ephemeris found by epoch folding. Epoch I provides the best statistics for this analysis. The ephemeris can be described with a constant spin-up, $\dot{P}_{\mathrm{pulse}} = (-3.0 \pm 0.3) \times 10^{-9}\,\mathrm{s\,s}^{-1}$ with pulse period between 15.755 s and 15.767 s. The uncertainties of the pulse periods were typically less than 0.003 s. Since it was not possible to correct the light curve for the orbital motion of the system, this spin-up trend might be caused by orbital effects and not by transfer of angular momentum of the accreted matter onto the neutron star. We extracted pulse-phase-resolved spectra using individual pulse periods following this ephemeris. The resulting pulse profile (Fig. 4.5) shows a double-peaked structure typical for these sources (see, e.g., Bildsten et al., 1997).

As in the time-resolved case, we used the **FDCUT** model to fit the phase-resolved spectra using three phase bins as indicated in Fig. 4.5: The main peak (MP), the secondary peak (SP), and the off state (off). The pulse phases of the bins are summarized in Table 4.3. Constant Galactic ridge emission is taken into account in the same way as for the pulse-averaged analysis. The background scaling factor for the PCA c_{b} is assumed to be equal to the result from the pulse-averaged analysis and was therefore frozen to this value. Initial fits of the pulse-phase-resolved spectra lead to large unconstraints in N_{H} and the width of the 10 keV feature σ_{G}. These values were therefore frozen to the results form the phase-averaged analysis. The S/N in the spectra from the individual pulse phases is too low to allow us to study the behavior of the CRSF. Similar to the flux-dependent analysis, we froze the CRSF centroid energy and width to the result from the pulse-averaged analysis and allowed only the optical depth/the equivalent width to vary (because of the marginal significance of the CRSF no other attempt was made to study a phase dependence of the cyclotron line).

Figure 4.6 shows the ratios of background-corrected pulse-phase-resolved spectra. The ratio MP/off appears to be mainly constant, while the other two ratios reveal more complex shapes. This constant ratio agrees with the spectral parameters of
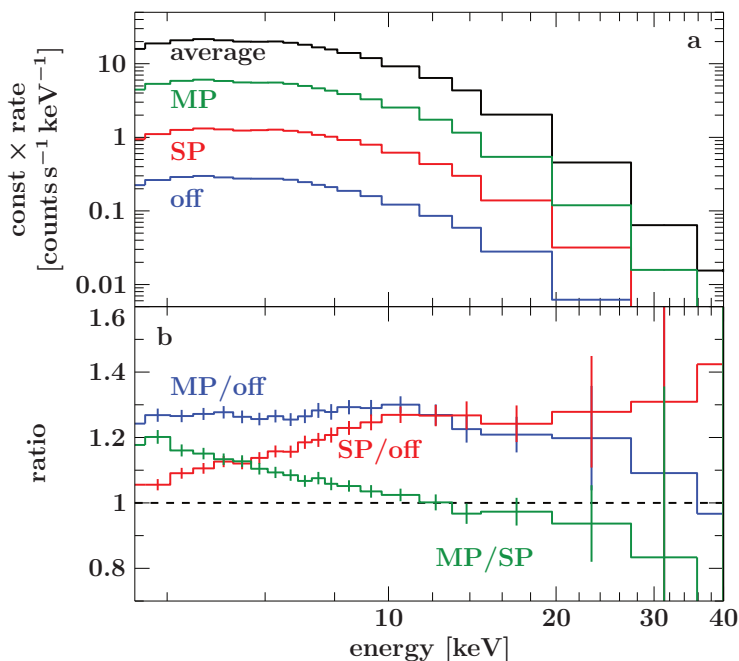
Figure 4.6: a: PCA spectra of the three phase bins together with the pulse-phase-averaged spectrum (shifted in y-direction for clarity). b: Ratio of the background-corrected pulse-phase-resolved spectra.

the main peak and the off state. These parameters show almost no or only slight differences to each other. The ratio MP/SP, a falling line, can be explained by a change in photon index. This explanation is confirmed from the spectral analysis. While E_{break} and E_{fold} show only small differences, the photon index Γ is significantly lower in the secondary peak, i.e., the spectrum in this phase bin is harder than in the other phase bins. The centroid energy of the $10\,\mathrm{keV}$ feature does not vary with pulse phase while its depth weakens during the main peak. The equivalent width remains constant in the main and the secondary peak, while it shows a higher value in the off state. Finally, there is neither evidence for changes of the Fe line flux nor for the equivalent width over the pulse phase.

4.4 Results and Conclusions

4.4.1 Outburst Series

We analyzed quasi-simultaneous XRT, ISGRI, and PCA observations of two outbursts of XTE J1946+274 during a series in the second half of 2010.

Before the onset of this outburst series, XTE J1946+274 was in a state of quiescence for almost one decade, i.e., about 20 orbits of the neutron star. Even though the formation, structure, and dynamics of Be-disks are even today far from being completely understood (see, e.g., Draper et al., 2011, and references therein), the missing mass accretion onto the neutron star during that time is probably due to the absence of a sufficiently large Be-disk during that time. A new outburst was only possible once the disk had been replenished and accretion could be triggered.

This series shows similar behavior as the one observed in 1998, e.g., two outbursts are observed per orbital period. The outbursts of XTE J1946+274 could also be similar to those seen in GX 301−2, which have been extensively modeled by Leahy (2002). These authors suggested that an additional stream of matter is flowing from the primary, and that a second outburst per orbit could be caused by the passage of the neutron star through this stream. These flux peaks of GX 301−2 occur near the

apsides of this system.

However, the outbursts of XTE J1946+274 do not clearly coincide with the times of periastron and apastron passages of the neutron star (Fig. 4.1). This could be explained by 3D simulations, which show that the disturbance of the Be-disk by the gravitational field of the neutron star could lead to a strong asymmetric structure of the circumstellar material, which could also lead to multiple X-ray outbursts during one orbital period (see, e.g., Okazaki et al., 2011).

Alternatively, the outbursts can be triggered by the neutron star passing through the Be-disk owing to a misalignment of the orbit and the Be-star's equatorial plane (Wilson et al., 2003).

Another possible explanation for the irregularity of the outbursts is that they are triggered by density variations in the Be-disk and not by orbital effects alone. This assumption could be verified by regular optical monitoring of the Balmer Hα line, which is an indicator for the presence of such a disk (see, e.g., Grundstrom et al., 2007, and references therein).

4.4.2 Spectroscopic Results

An absorbed Fermi-Dirac cutoff power-law together with an iron Kα fluorescence line, an iron line complex between 6 and 7 keV caused by Galactic ridge emission, a Gaussian-like absorption feature around 10 keV, and a cyclotron line at $\sim$25 keV reproduce the observations well in terms of χ^2_{red}. We found time- as well as pulse-phase-dependent variability of the continuum parameters of XTE J1946+274. In the time-resolved case, these changes might be caused by different accreting mechanisms depending on the mass transfer onto the neutron star. The periodically changing line of sight with respect to the X-ray emitting region, caused by the rotation of the neutron star, is likely responsible for the variabilities observed in the pulse-phase-resolved analysis. Furthermore, this rotation together with differences in the accretion geometries at the two magnetic poles of the neutron star might lead to the asymmetric pulse profile of the X-ray pulsar (see Fig. 4.5).

Studying the behavior of the spectral shape is problematic because the spectral parameters photon index Γ, folding energy E_{fold}, and the cutoff energy E_{break}, which describe the broadband shape of the X-ray spectrum, show strong cross correlations. To account for this, we calculated ratios of the spectra for the time-resolved and the pulse-phase-resolved studies. In the time-resolved case, we found clear deviations from a constant ratio for epoch V. During epochs I–IV, the overall spectral shape seems to remain relatively constant. In the pulse-phase-resolved analysis, the spectrum of the secondary peak turns out to be significantly harder than those from the main peak and the off state. These properties of X-ray spectra are caused for instance by the temperature of the visible part of the X-ray emitting region, in particular the accretion column.

Another feature required to achieve a good fit is a source-intrinsic Gaussian iron Kα emission line at 6.4 keV. The disagreement in the strength of the required emission in this energy range between PCA and XRT in initial fits can be solved by inducing the emission of the Galactic ridge. The strength of the Galactic ridge emission is about four times larger than found in other regions of the Galaxy (Ebisawa et al., 2007). This difference is consistent, however, with the typical spatial variations of the ridge emission (Yamauchi et al., 2009). Furthermore, Kühnel et al. (2013) found an emission strength consistent with our result for GRO J1008$-$57.
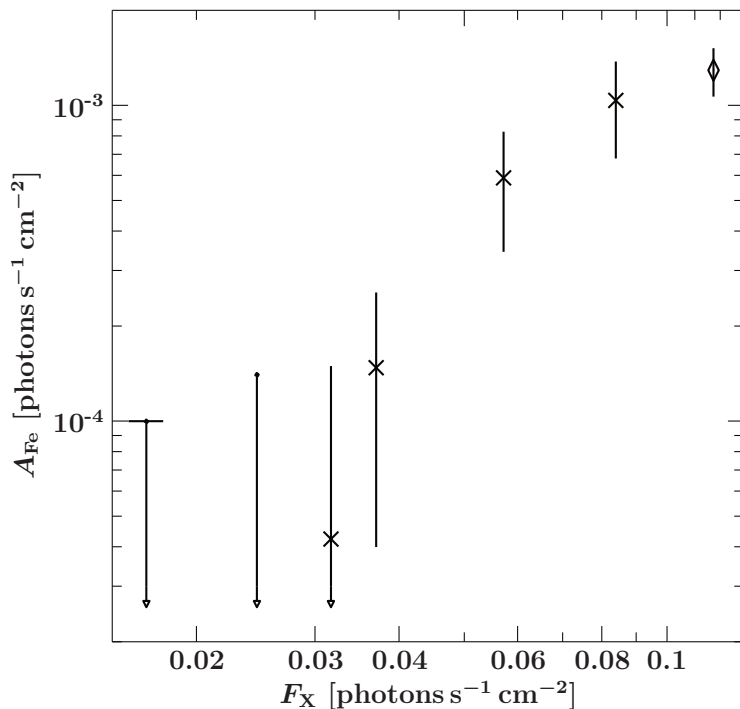
Figure 4.7: Flux of the iron $K\alpha$ fluorescence line against the $7-15\,\mathrm{keV}$ flux. The crosses correspond to the data from the 2010 outburst, and the diamond to the average spectrum of the 1998 outburst, obtained by reextracting and analyzing the old PCA and HEXTE data from 1998.

After taking into account the contribution from the Galactic ridge emission, the flux of the source intrinsic Fe $K\alpha$ emission line was correlated with the X-ray flux F_{X} (see Fig. 4.7), as also observed in other X-ray transients (see, e.g., Inoue, 1985). The Fe $K\alpha$ line is significantly detected at source fluxes (7–$15\,\mathrm{keV}$) greater than about $0.035\,\mathrm{photons\,s^{-1}\,cm^{-2}}$. At fluxes below this value, the source intrinsic line is consistent with zero. The equivalent width W_{Fe} stays constant for high luminosities, i.e., epochs I–III. Reanalyzing the earlier *RXTE* data (Heindl et al., 2001) with the continuum model employed here yielded an equivalent width that also agrees with the result from the 1998 outburst ($W_{\mathrm{Fe}}^{1998} = 59 \pm 10\,\mathrm{eV}$). The different values for W_{Fe} for the fainter observations, where the Fe $K\alpha$ line is only marginally detected, can be caused by the uncertainties of the Galactic ridge emission, which significantly contributes to the data at these energies. In the pulse-phase-resolved analysis we found no evidence for variability of the line flux. This result indicates that it is emitted in a region that is quite extended compared to the distance traveled by light during one pulse period. The equivalent width shows no variation either, while rather a variation is expected for this parameter when the respective model component remains constant at varying flux levels. However, this can be explained by the quite large relative uncertainty of W_{Fe}, which is on the same order of magnitude as the respective variations.

The $10\,\mathrm{keV}$ feature is present during all epochs and pulse phases. It shows relatively constant results for line energy, width, and depth in the time-resolved case. The reanalysis of the 1998 data yields an equivalent width of $W_{\mathrm{G}}^{1998} = -250_{-270}^{+120}\,\mathrm{eV}$, which also equals the results for the current outburst. While we found almost no connection of the parameters of this feature with the luminosity, its optical depth and equivalent width varies with pulse phase. W_{G} is constant during the main and the secondary peak, but it strongly increases during the off state. This behavior indicates that the fractional amount of absorbed flux related to the continuum level is constant for the main and the secondary peak and changes in the off state. This behavior of

the 10 keV feature could give rise to speculations about possible physical processes as, e.g., pulse-phase-dependent absorbing processes, which could produce such a feature. On the other hand, the residuals around 10 keV could also be caused by the failing of the spectral broadband continuum models, which in turn would result in a wrong description of the data around these energies. More quantitative analyses of this feature, also from other sources where it occours in emission, are urgently needed to reveal the true nature of this enigmatic feature.

4.4.3 Cyclotron Resonance Scattering Feature

We found weak evidence for the presence of the CRSF, first discovered by Heindl et al. (2001) during the 1998 outburst series. The cyclotron line improved the model fit for the high S/N epoch I spectrum, where PCA and ISGRI data are available. Later spectra are consistent with the presence of a CRSF with unchanged parameters, but the line is not formally detected in these observations because of their lower S/N. We stress that due to its relative weakness, including the CRSF in our fits does not affect our results for the continuum parameters or for the pulse-phase-resolved analysis.

If the identification of the line is correct, its depth in 2010 was significantly lower than that measured in the 1998 outburst ($\tau_{\mathrm{CRSF}}^{2010} = 0.09^{+0.10}_{-0.07}$ vs. $\tau_{\mathrm{CRSF}}^{1998} = 0.33^{+0.07}_{-0.06}$, Heindl et al., 2001). Furthermore, the centroid energy of the CRSF in 2010 ($E_{\mathrm{CRSF}}^{2010} = 25.3^{+0.9}_{-1.0}$ keV) is significantly lower than in 1998 ($E_{\mathrm{CRSF}}^{1998} = 36.2^{+0.5}_{-0.7}$ keV, Heindl et al., 2001). Reanalyzing the earlier *RXTE* data as described above yields CRSF parameters that are consistent with those found by Heindl et al. (2001). Furthermore, the equivalent width in 1998 was also significantly larger than in the current data ($W_{\mathrm{CRSF}}^{1998} = (-2.1^{+0.6}_{-1.0}) \times 10^3$ eV).

One reason why constraining the CRSF is so much easier in the 1998 data is because while the exposure times of the 1998 and the 2010 data are comparable, the 10–20 keV X-ray flux of the 1998 observation is ~40% higher than in the 2010 observation (~9.6×10^{-2} vs. ~6.9×10^{-2} photons s^{-1} cm^{-2}). However, fits to the 2010 data in which we fixed the CRSF parameters to their 1998 values did not yield a satisfactory description of the data (χ^2_{red}/dof = 1.55/69). Could this indicate that the energy of the line has varied? Assuming that the CRSF width and depth remained the same, we searched for a line similar to that found in the 1998 data. Varying the CRSF energy in steps of a 1 keV and refitting the continuum parameters did not yield any satisfactory results, with best-fit $\chi^2_{\mathrm{red}} > 1.5$ over the 20 to 60 keV band (see Fig. 4.8, red curve). This result indicates that irrespective of the difference in the S/N between both data sets, the CRSF must have varied between both outbursts, and a strong line as that seen in 1998 is not consistent with the data analyzed here.

Taking the 2010 CRSF values at face value, a possible explanation for the difference between the 1998 and 2010 outbursts could be the flux dependence that is seen in some other CRSF sources (see, e.g., Caballero & Wilms, 2012, for a recent discussion). XTE J1946+274 could therefore be a cyclotron source with an overall positive correlation between the X-ray flux and the CRSF energy, similar to Her X-1 (Staubert et al., 2007). In models for the change in cyclotron line energy in neutron stars this change is generally interpreted as a change in height of the line-producing region because the accretion column changes with mass accretion rate (and thus luminosity).

Using the dipole approximation for the magnetic field strength

$$B \propto \frac{1}{r^3}, \tag{4.2}$$
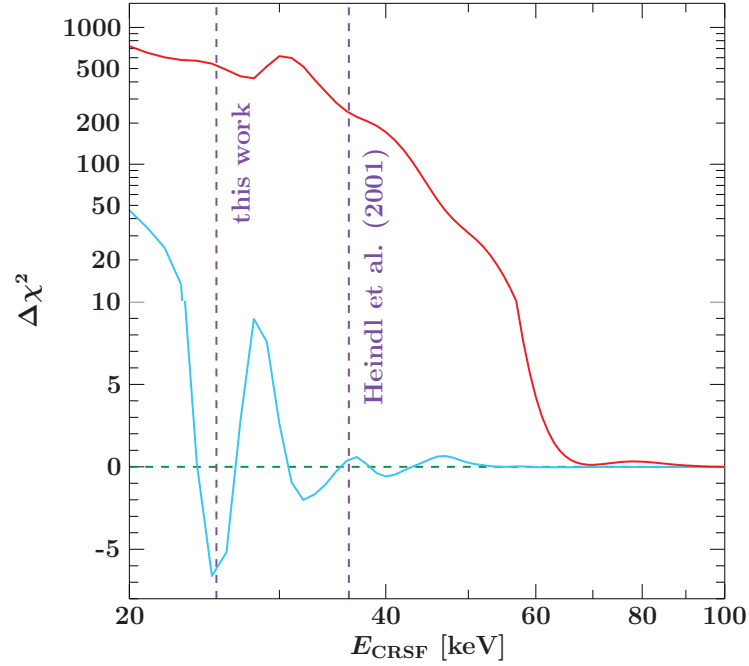
Figure 4.8: a: Difference of χ^2 of the best fit of epoch I with frozen CRSF parameters (Fig. 4.2k) and the χ^2 of the best fit without CRSF. The centroid energy was varied in steps of 1 keV. The red dashed-dotted curve displays the χ^2 of the best fit when using τ_{CRSF} and σ_{CRSF} from Heindl et al. (2001). For the light blue solid curve the parameters from this work were used. The dark blue dashed-double-dotted curve shows this difference when the width as well as the depth (the upper limit has been set to 3) of the CRSF are allowed to vary, i.e., the same situation as in Fig. 4.2. The two additional minima in χ^2 are discussed in Sect. 4.3.2. The horizontal dashed line indicates $\Delta\chi^2 = 0$, and the horizontal dotted line seperates the logarithmic and linear scaling in y-direction. The vertical dashed lines shows the position of the CRSF derived in Heindl et al. (2001) and this work. b and c: results for the optical depth and width of the CRSF, respectively, when these parameters were allowed to vary. The plateau of the curve displayed in panel b at $\sim$60–70 keV is caused by the upper limit for τ_{CRSF} of 3.

where r denotes the distance to the dipole center, yields an expression for the ratio of the magnetic field strength:

$$\frac{B_1}{B_2} = \left(\frac{r_2}{r_1}\right)^3 \tag{4.3}$$

Together with the 12-B-12-rule (Eq. 2.14) and the gravitational red shift

$$z_{\mathrm{g}} = -\frac{GM_{\mathrm{NS}}}{rc^2}, \tag{4.4}$$

this relation leads to a cubic equation as

$$\underbrace{\left(\frac{c}{r_1}\right)^2}_{=:a} r_2^3 - \underbrace{\left(\frac{GM_{\mathrm{NS}}}{r_1^2}\right)}_{=:b} r_2^2 - \underbrace{\frac{E_1}{E_2}\left(r_1 c^2 - GM_{\mathrm{NS}}\right)}_{=:c} = 0. \tag{4.5}$$

This equation can be solved using Cardano's method, i.e.,

$$r_2 = \sqrt[3]{-\frac{q}{2} + \sqrt{D}} + \sqrt[3]{-\frac{q}{2} - \sqrt{D}} - \frac{b}{3a}, \tag{4.6}$$

where

$$p := -\left(\frac{b}{3a}\right)^2, \quad q := \frac{1}{2}\left(\frac{2b^3}{27a^3} + \frac{c}{a}\right), \quad \text{and } D := q^2 + p^3. \tag{4.7}$$

With the assumption that in 1998 the CRSF was emitted from the neutron star's surface ($r_1 = 10\,\text{km}$) and the neutron star has a mass of $M_{\text{NS}} = 1.4\,\text{M}_\odot$ follows a height difference of $1.2\,\text{km}$ for the regions where the CRSF is generated. This result is in agreement with typical estimates of several kilometers for the height of the accretion columns (see, e.g., Basko & Sunyaev, 1976). Becker et al. (2012) showed that a positive correlation between flux and energy is possible in the luminosity range where the stopping in the accretion column is dominated by Coulomb braking. For cyclotron line energies around $30\,\text{keV}$ Coulomb braking is the dominating braking process in the luminosity range 1–$5 \times 10^{37}\,\text{erg s}^{-1}$. For higher luminosities, radiation braking dominates. XTE J1946+274's peak outburst luminosity of $4.5 \times 10^{37}\,\text{erg s}^{-1}$ is barely consistent with this range, but because the source seems to be located at the transition between Coulomb and radiation braking and was brighter in 1998, the very strong change in CRSF energy seems unlikely to be due to a pure mass accretion rate effect.

In conclusion, while the possibility of a luminosity dependent CRSF is intriguing, the poor S/N of the 2010 data does not allow a definitive answer concerning the luminosity dependence of the CRSF. Additional longer monitoring observations of XTE J1946+274 during its next outburst episode are urgently needed to resolve this question.

Chapter 5

No Anticorrelation between Cyclotron Line Energy and X-ray Flux in 4U 0115+634

L IKE in Sect. 4, the analysis of *RXTE* and *INTEGRAL* data of a giant type II outburst in 2008 March/April of the high mass X-ray binary 4U 0115+63 has already been published in *Astronomy & Astrophysics* (Müller et al., 2013), on which this Section and parts of Sect. 7 are based on. Section 5.5 on the analysis of *Suzaku* data of 4U 0115+634 and some other small parts of the *Suzaku* analysis within Sect. 5 gives the current state of a paper draft which will be submitted to the journal A&A in the near future. Almost all parts of the work presented in this Section have been done by myself, apart from the data reduction of the *Suzaku* spectra, which was performed by Dominik Hertel as a part of his Diploma thesis. The data extraction of the *INTEGRAL* data was performed by Victoria Grinberg and Felix Fürst.

5.1   Introduction

4 U 0115+634 is one of the X-ray pulsars for which CRSFs have been studied in great detail (see, e.g., Wheaton et al., 1979; White et al., 1983; Nagase et al., 1991; Heindl et al., 1999; Santangelo et al., 1999; Mihara et al., 2004; Nakajima et al., 2006; Tsygankov et al., 2007; Ferrigno et al., 2009, 2011). The source shows 3.61 s pulsation (Giacconi et al., 1972) and has an orbital period of $\sim$24.3 d (Cominsky et al., 1978; Rappaport et al., 1978). The optical counterpart is the O9e star V635 Cas (Johns et al., 1978; Unger et al., 1998).

In previous outbursts, CRSFs have been detected up to the fifth harmonic (Heindl et al., 2000). This is the largest number of detected CRSFs in an accreting X-ray pulsar. In later work, a negative correlation between L_{X} and E_{cyc} was found (e.g., Nakajima et al., 2006; Tsygankov et al., 2007; Müller et al., 2010), meaning that the source should be located in the supercritical luminosity regime. As already explained in Sect. 2.7.2, the relations between L_{X} and E_{cyc} could be due to the different deceleration mechanisms for the accreted material. Other authors even found a discontinuous behavior of the fundamental line energy and explained this by a sudden change of the accretion conditions (Li et al., 2012).

In this work we revisit the behavior of the CRSFs in 4U 0115+634. Focusing on *RXTE* and *INTEGRAL* data taken during a giant outburst in 2008 March/April.
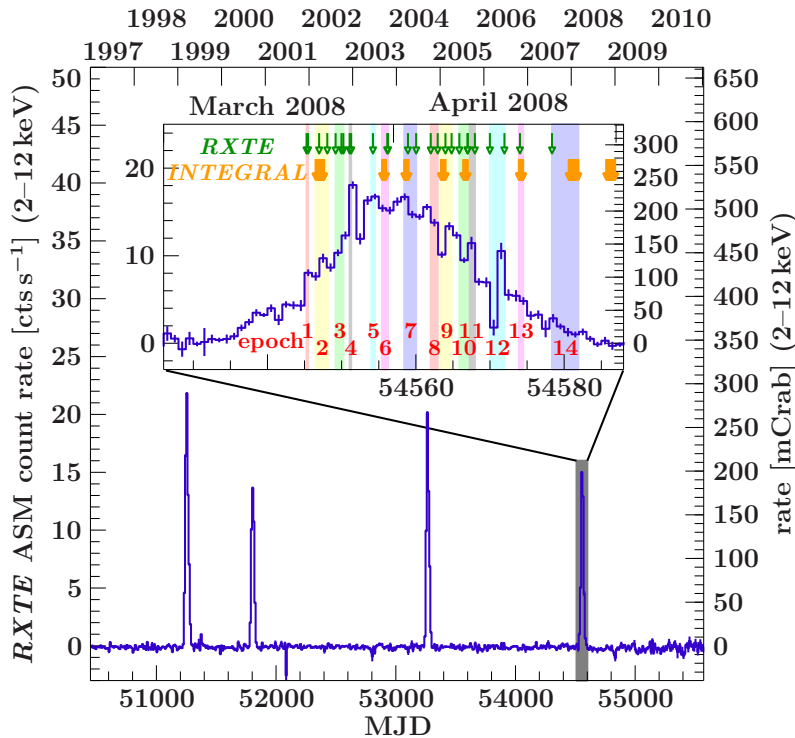
Figure 5.1: *RXTE*/ASM light curve of 4U 0115+634 (2–12 keV). The inset shows a close-up view of this light curve, showing the 2008 outburst in detail. Arrows indicate the times of pointed *RXTE* and *INTEGRAL* observations. Numbers indicate the observation epochs used in the data analysis (see also Table 5.1).

We show that the previously claimed relation between the source flux F_X and E_{cyc} strongly depends on the choice of the underlying continuum model. We argue that the cyclotron line is only modeled correctly when using an exponentially cutoff power-law continuum with a strong emission feature around 10 keV, resulting in a relatively stable centroid energy of the fundamental cyclotron line. Furthermore, alternative continua models, which have been used in some earlier investigations, result in incorrect cyclotron line parameters which can cause the apparent relation between source flux F_X and fundamental cyclotron line energy E_0. We verify our results with a *Suzaku* dataset taken during a later outburst of this source (see Sect. 5.5).

5.2   Observations and Data Reduction

T HE outburst of 4U 0115+634 started 2008 March 12, after a phase of almost four years of quiescence, when *Swift*/BAT detected a significant increase of the X-ray flux (Larionov & Arkharov, 2008). The outburst lasted about 40 days and exceeded a flux of ∼200 mCrab in the 2–12 keV *RXTE*/ASM band (Fig. 5.1). The whole outburst was monitored with pointed observations by the *RXTE* and several pointed observations by the *INTEGRAL*. Here, we use data from *RXTE*'s PCA and HEXTE, as well as *INTEGRAL*'s ISGRI. Data were reduced with our standard analysis pipelines, based on HEASOFT (v. 6.11) and *INTEGRAL* OSA v. 9.0. Data modeling was performed with the newest version of the *Interactive Spectral Interpretation System* (ISIS, Houck & Denicola, 2000).

Since PCU 2 is known to have been the best calibrated one (see Sect. 3.4.2), we only extracted spectra from this PCU in the `standard2f` mode. The hard X-ray spectrum from 15–250 keV was monitored with HEXTE (see Sect. 3.4.3). Because of the failure of cluster A before our observations, we only used data from cluster B. Concerning ISGRI (see Sect. 3.5.1), We extracted all available spectra for which

Table 5.1: Log of observations for the 2008 outburst of 4U 0115+634. The first part of the table contains the *RXTE* observations, the second part the ISGRI data.

ID^a	start date	MJD	$t_{\exp}{}^b$ [s]	epoch
01-01-00	2008 Mar 20	54545.27–54545.43	8336/2413	1
01-01-01	2008 Mar 20	54545.47–54545.49	1648/382	1
01-02-04	2008 Mar 21	54546.97–54547.20	12448/3938	2
01-02-00	2008 Mar 23	54548.07–54548.25	9904/3082	2
01-02-01	2008 Mar 24	54549.19–54549.30	6336/1948	3
01-02-02	2008 Mar 24	54549.97–54550.14	8832/3136	3
01-02-03	2008 Mar 25	54550.24–54550.28	2384/934	3
01-02-05	2008 Mar 26	54551.08–54551.17	4096/1679	4
01-02-06	2008 Mar 26	54551.28–54551.31	752/625	4
01-03-02	2008 Mar 29	54554.23–54554.38	576/2112	5
01-03-01	2008 Mar 31	54556.14–54556.16	768/473	6
01-03-00	2008 Mar 31	54556.25–54556.37	768/1558	6
01-03-03	2008 Apr 02	54558.93–54559.10	5456/3104	7
01-04-00	2008 Apr 04	54560.04–54560.22	4240/2998	7
01-04-01	2008 Apr 06	54562.01–54562.18	5888/2908	8
01-04-02	2008 Apr 06	54562.95–54563.09	5552/2317	8
01-04-03	2008 Apr 07	54563.99–54564.07	3856/1548	9
01-04-04	2008 Apr 08	54564.82–54564.98	7808/2853	9
01-04-05	2008 Apr 09	54565.86–54566.10	10896/4101	10
01-04-06	2008 Apr 10	54566.98–54567.00	1648/699	10
01-05-00	2008 Apr 11	54567.00–54567.01	1056/381	11
01-05-01	2008 Apr 11	54567.96–54568.13	9632/3176	11
16-01-00	2008 Apr 13	54569.98–54570.16	10192/3043	12
16-01-01	2008 Apr 15	54571.94–54572.12	10368/3162	12
16-02-00	2008 Apr 18	54574.04–54574.15	7184/1924	13
16-02-01	2008 Apr 22	54578.36–54578.51	6480/1679	14
664	2008 Mar 21	54546.48–54547.68	55981	2
667	2008 Mar 30	54555.46–54556.04	28279	6
668	2008 Apr 02	54558.45–54559.05	27655	7
669	2008 Apr 07	54563.38–54564.02	28495	9
670	2008 Apr 10	54566.41–54567.01	30990	10
673	2008 Apr 17	54573.90–54574.50	31360	13
675	2008 Apr 24	54580.62–54581.97	70902	14
677	2008 Apr 29	54585.69–54586.91	63662	–

^{a} For *RXTE*, the first column contains the number of the Obs-ID after "93032-". For ISGRI, it contains the revolution number. ^{b} For *RXTE*, the two numbers correspond to the PCA and HEXTE exposures, respectively.

4U 0115+634 was less than $10°$ off-axis. Table 5.1 contains an observation log (see also Fig. 5.1).

For the spectral analysis we used data between 3 and 50 keV for PCA, and between 20 and 100 keV for HEXTE and for ISGRI. A systematic error has been added in quadrature to the PCA and ISGRI data, using the canonical values of 0.5% and 2.0% (Jahoda et al., 2006, and IBIS Analysis User Manual[1]), respectively. To improve the S/N of the spectra, we averaged the data over 14 data blocks in time. These data blocks are defined in the fifth column of Table 5.1 and shown in Fig. 5.1. We omitted one ISGRI dataset from our analysis (revolution number 677), because no simultaneous *RXTE* data are available at that time and the source was almost in the off state during that observation.

5.3 Spectral Analysis

5.3.1 Pulsar Continuum Models

As described in Sect. 2.6.1, a large problem when analyzing X-ray spectra from X-ray binary pulsars is to find a good description of the broadband continuum and therefore mostly semi empirical models are used. For sources with cyclotron lines, the continuum model is modified with a description of the cyclotron line (see Sect. 2.7.2). Here, we model the CRSFs with **CYCLABS**, a pseudo-Lorentzian profile as given by Eq. 2.15, with the centroid energy, E_{cyc}, the width of the feature, W, and the optical depth of the line, τ. This approach allows the comparison of the line parameters with results from previous papers, in which also the **CYCLABS** model has been used (e.g., Nakajima et al., 2006; Tsygankov et al., 2007; Li et al., 2012). In the remainder of this Section, we label the cyclotron line parameters with the number of respective harmonic, where 0 corresponds to the fundamental line. As is common for CRSFs, W and τ are strongly correlated (Coburn, 2001). We therefore set a lower limit of 0.5 keV for the width, which is comparable to the typical PCA resolution.

In order to describe the data of 4U 0115+634, in addition to several of the continuum models discussed in Sect. 2.6.1, we take interstellar absorption into account, modeled as described in Sect. 2.6.2.1. We furthermore account for an intrinsic Fe Kα fluorescence line, which we describe with an additive narrow Gaussian emission line with frozen centroid energy at 6.4 keV, a width of 0.1 eV, and a flux A_{Fe} and equivalent width W_{Fe}. Assuming a narrow line is justified because in systems like 4U 0115+63 Fe Kα is expected to have a width of the order of $\lesssim 0.5$ keV (see, e.g., Torrejón et al., 2010), which cannot be resolved by the PCA.

In order to take into account that the flux normalization of the different instruments used is not perfectly known we introduce cross calibration constants c_{HEXTE} and c_{ISGRI} as free fit parameters. These constants also account for flux differences of the source between the observations which were not fully simultaneous. The PCA background was estimated using the standard models provided by GSFC. These estimates often show a flux deviation from the proper background by a few percent. This deviation was accounted for by multiplying the background flux with another fit parameter, c_{b} (see also Rothschild et al., 2011).

---

[1]http://www.isdc.unige.ch/integral/analysis#Documentation
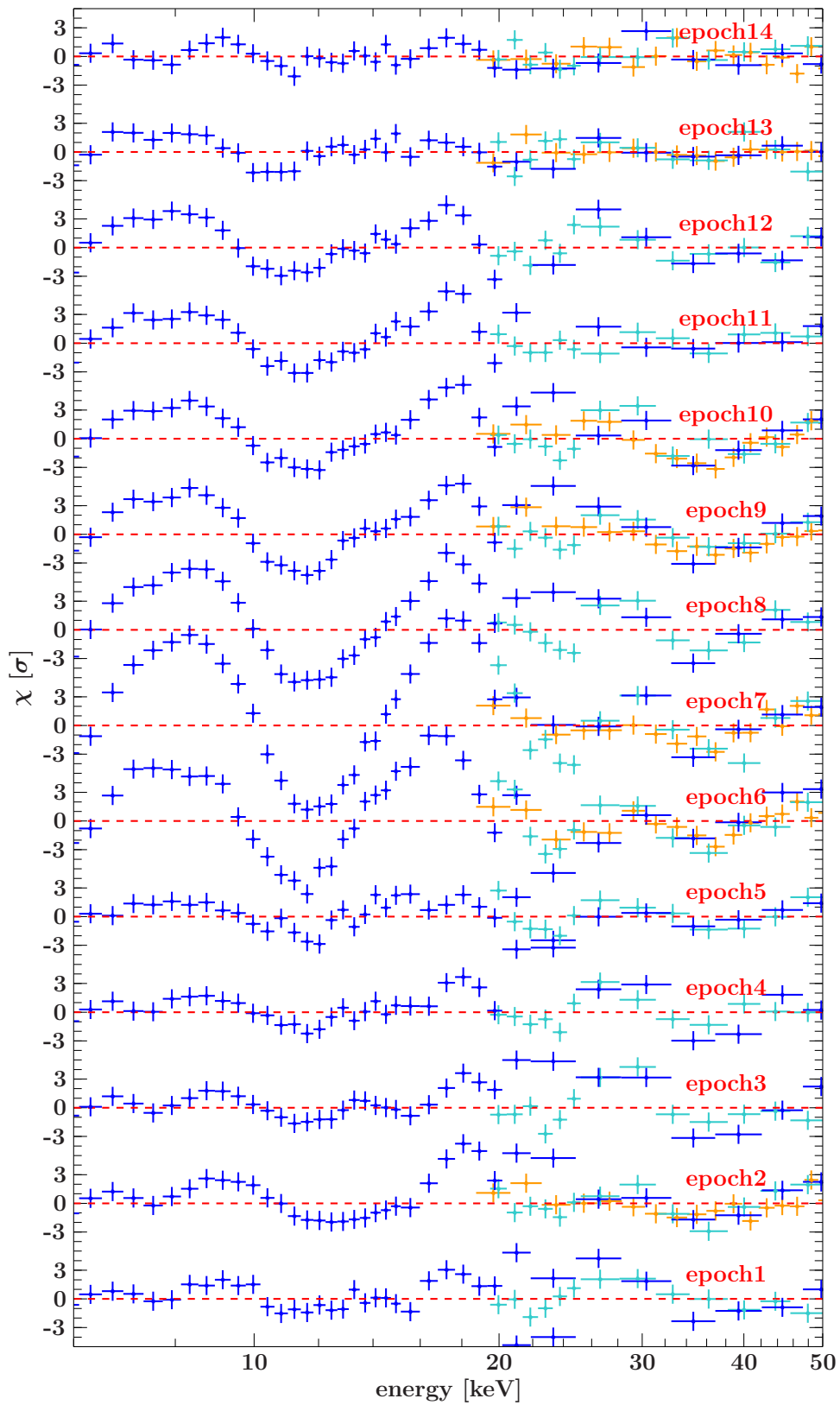
Figure 5.2: Deviations between the data and the best fit with `CutoffPL` and 10 keV feature for the PCA (circles), HEXTE (crosses), and ISGRI (filled diamonds) in units of standard deviations σ. For these fits, no cyclotron lines have been taken into account. The numbers on the right side indicate the respective epoch.
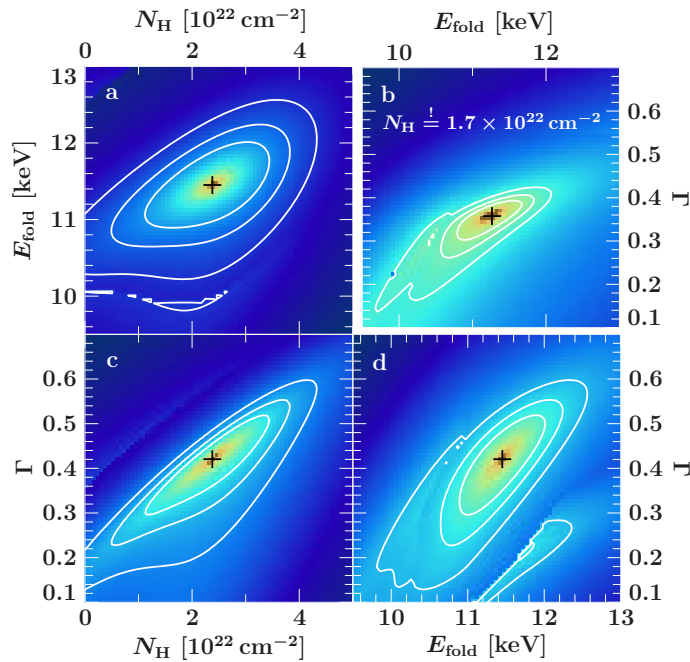
Figure 5.3: a, c, d: Confidence contours for the folding energy, the photon index and the hydrogen column density for epoch 6. b: Confidence contours between the E_{fold} and Γ with N_{H} frozen to $1.7 \times 10^{22}\,\mathrm{cm}^{-2}$. Contour lines correspond to the 68.3%, 90%, and 99% levels. Color indicates $\Delta\chi^2$ with respect to the best fit value, with the color scale running from orange (low $\Delta\chi^2$) to dark blue (large $\Delta\chi^2$).

5.3.2 Fitting Strategy

Since the `CutoffPL` (Eq. 2.4) is the easiest continuum model for X-ray pulsars, we used this model for our fits. Furthermore, the 10 keV feature (see Sect. 2.6.2.4) in emission is required to get a good description of the data . For each epoch, the fits have been simultaneously performed for all available instruments. Figure 5.2 shows the residuals of the best fit using this continuum without taking any CRSFs into account. These residuals clearly indicate the need of the cyclotron lines in this model at ~11, 22, and sometimes above 30 keV. As the quality of individual data sets is strongly variable over the outburst, in an initial fit run a variable number of CRSFs were added to individual fits until the reduced χ^2, $\chi^2_{\mathrm{red}} \sim 1$. To avoid continuum modeling with the absorption features, we fixed the widths of the CRSFs of the second and higher harmonics to typical values, i.e., 4 keV (Ferrigno et al., 2009).

In order to check whether the number of different cyclotron features in the model affects the fit results of the continuum parameters and the fundamental and first harmonic CRSF, in a second run all spectral fits included only the fundamental line and its first and second harmonics. For epochs, where only the first harmonic was necessary to obtain a good fit in our initial run, we added the second harmonic with fixed parameters during the second run, holding its parameters at the mean values of the results from the other epochs.

Since initial fits with the `CutoffPL` continuum showed large uncertainties for the hydrogen column density, N_{H}, without a significant variability between different epochs, we held N_{H} fixed at the mean value $N_{\mathrm{H}} = 1.7 \times 10^{22}\,\mathrm{cm}^{-2}$ to avoid unphysical correlations between these fit parameters (Fig. 5.3).

The two fit runs show that almost all fit parameters are equal within their respective uncertainties for both runs. Only E_{fold} and the line parameters of the second harmonic are slightly different in epoch 6 and 7. These differences can be explained by the fact that for these two cases the second run has to account for the equivalent of the four harmonics required in the first run. The differences affect mainly the higher energies and are compensated by a change in the folding energy and the closest cy-
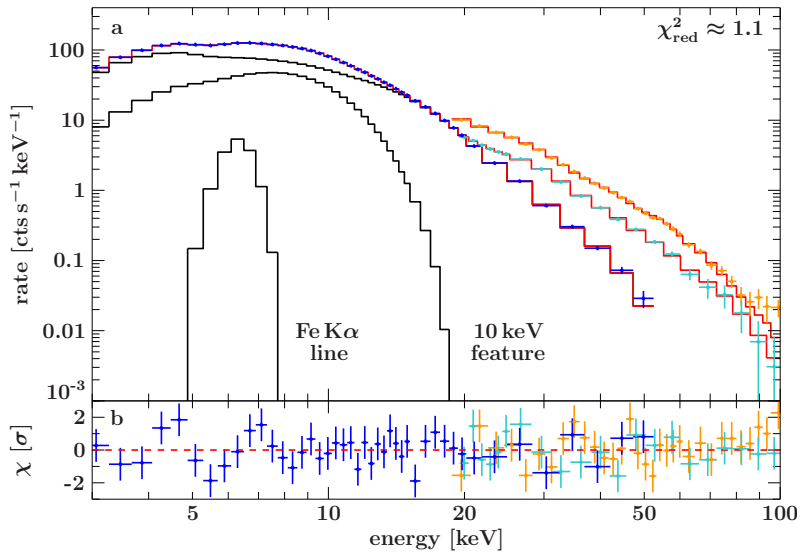
Figure 5.4: a: Folded spectrum from epoch 6 together with best fit (red) and all model components, i.e., `CutoffPL`, 10 keV feature, Fe Kα fluorescence line, and five cyclotron features. b: Residuals of the best fit, shown as the difference between the data and the model normalized to the uncertainty of each data point. Dark blue data points correspond to PCA, cyan points to HEXTE, and orange points to ISGRI.

clotron line, i.e., the second harmonic. The remainder of this paper is based on the results from the first fit run.

An example for the best fit using the `CutoffPL` continuum with 10 keV feature and five cyclotron features (fit run a, epoch 6) is shown together with all model components in Fig. 5.4. This spectrum was recorded by all three instruments during the maximum of the outburst, i.e., epoch 6. All fit results from runs using the `CutoffPL` continuum are summarized in Table 5.2.

5.4 Spectral Evolution: No Anticorrelation of the Cyclotron Line Energy with Flux

FIGURES 5.5–5.7 show the evolution of the continuum and cyclotron line parameters as well as the parameters for the Fe Kα line for the first fit run with the `CutoffPL` continuum and 10 keV feature, and fixed N_{H} (see also Table 5.2). As already noted in previous analyses for 4U 0115+634, the continuum varies over the outburst (e.g., Li et al., 2012). During the brightest phases of the outburst the spectrum is the hardest one. As shown in Fig. 5.3, the variation of Γ is significantly larger than the very slight correlation seen between Γ and E_{fold}. As expected, the source's intrinsic iron Kα line is significantly present during all epochs. As also observed in other X-ray transient pulsars (Inoue, 1985) and expected for a line originating from fluorescence, the line flux is positively correlated to the X-ray flux from the source. The equivalent width stays constant within the uncertainties over the outburst. The 10 keV feature varies in both, the centroid energy E_{G} and its flux A_{G}. Its energy seems to be slightly anticorrelated with the source flux, while the relative flux in the feature, i.e., the ratio between the flux in the 10 keV feature and the total flux, remains constant. Its width, σ_{G}, remains relatively constant between 3.0 keV and 3.5 keV.

Very different from virtually all previous analyses, however, the cyclotron line is seen to be only slightly varying over the outburst. The colored data points in Fig. 5.6 and 5.7 show the centroid energy, E_0, the width, W_0, and the optical depth, τ_0, of the fundamental cyclotron line against time and flux for the `CutoffPL` continuum, modi-

Table 5.2: Continuum parameters of the time resolved spectral analysis. Fits were performed with the `CutoffPL` model and a varying number of CRSFs.

ep^a	L_x^b	Γ	E_{fold} [keV]	A_{Fe}^c [10^{-3}]	W_{Fe} [eV]	E_G [keV]	A_G^c	σ_G [keV]	c_b	c_{HEXTE}	c_{ISGRI}	χ^2_{red}/dof
1	$4.38^{+0.02}_{-0.02}$	$0.59^{+0.04}_{-0.05}$	$10.7^{+0.5}_{-0.5}$	$2.5^{+0.6}_{-0.6}$	55^{+12}_{-12}	$8.3^{+0.3}_{-0.3}$	$0.18^{+0.02}_{-0.02}$	$3.4^{+0.1}_{-0.3}$	$1.00^{+0.02}_{-0.02}$	$0.73^{+0.02}_{-0.02}$	—	1.13/50
2	$5.35^{+0.02}_{-0.02}$	$0.56^{+0.03}_{-0.03}$	$11.5^{+0.4}_{-0.4}$	$2.9^{+0.7}_{-0.7}$	53^{+10}_{-10}	$8.0^{+0.2}_{-0.2}$	$0.19^{+0.02}_{-0.02}$	$3.3^{+0.1}_{-0.1}$	$0.96^{+0.01}_{-0.01}$	$0.74^{+0.01}_{-0.01}$	—	1.12/77
3	$7.48^{+0.02}_{-0.02}$	$0.54^{+0.03}_{-0.03}$	$11.6^{+0.3}_{-0.3}$	$3.7^{+0.9}_{-0.9}$	46^{+10}_{-10}	$7.3^{+0.2}_{-0.2}$	$0.34^{+0.01}_{-0.01}$	$3.6^{+0.1}_{-0.1}$	$0.94^{+0.01}_{-0.01}$	$0.75^{+0.01}_{-0.01}$	$0.87^{+0.02}_{-0.02}$	1.32/48
4	$8.66^{+0.03}_{-0.03}$	$0.45^{+0.03}_{-0.03}$	$10.8^{+0.3}_{-0.3}$	$4.4^{+1.0}_{-1.0}$	46^{+10}_{-10}	$7.1^{+0.2}_{-0.2}$	$0.37^{+0.03}_{-0.03}$	$3.5^{+0.1}_{-0.1}$	$0.94^{+0.02}_{-0.02}$	$0.78^{+0.01}_{-0.01}$	—	0.88/48
5	$9.24^{+0.05}_{-0.06}$	$0.42^{+0.05}_{-0.08}$	$10.7^{+0.4}_{-0.6}$	$5.4^{+1.7}_{-1.7}$	52^{+17}_{-17}	$7.0^{+0.5}_{-0.8}$	$0.44^{+0.08}_{-0.07}$	$3.6^{+0.3}_{-0.3}$	$0.92^{+0.05}_{-0.05}$	$0.94^{+0.02}_{-0.02}$	—	0.79/48
6	$10.18^{+0.04}_{-0.04}$	$0.36^{+0.04}_{-0.07}$	$11.3^{+0.5}_{-0.6}$	$5.8^{+1.6}_{-1.5}$	51^{+13}_{-13}	$7.2^{+0.7}_{-0.3}$	$0.31^{+0.07}_{-0.05}$	$3.0^{+0.4}_{-0.4}$	$0.93^{+0.04}_{-0.04}$	$0.88^{+0.02}_{-0.01}$	$1.04^{+0.02}_{-0.02}$	1.09/75
7	$9.43^{+0.03}_{-0.03}$	$0.36^{+0.04}_{-0.07}$	$10.8^{+0.4}_{-0.5}$	$6.4^{+1.2}_{-1.2}$	61^{+10}_{-10}	$7.7^{+0.4}_{-0.7}$	$0.30^{+0.04}_{-0.04}$	$3.1^{+0.2}_{-0.2}$	$0.94^{+0.02}_{-0.02}$	$0.84^{+0.01}_{-0.01}$	$1.05^{+0.02}_{-0.02}$	1.18/75
8	$8.70^{+0.03}_{-0.03}$	$0.38^{+0.04}_{-0.07}$	$10.2^{+0.3}_{-0.5}$	$5.9^{+1.0}_{-1.0}$	61^{+10}_{-10}	$7.7^{+0.4}_{-0.4}$	$0.32^{+0.04}_{-0.04}$	$3.3^{+0.2}_{-0.2}$	$0.93^{+0.02}_{-0.02}$	$0.78^{+0.01}_{-0.01}$	—	1.27/48
9	$7.84^{+0.03}_{-0.03}$	$0.50^{+0.03}_{-0.04}$	$11.5^{+0.4}_{-0.3}$	$5.1^{+1.0}_{-1.0}$	60^{+10}_{-10}	$7.7^{+0.4}_{-0.3}$	$0.32^{+0.03}_{-0.03}$	$3.3^{+0.2}_{-0.2}$	$0.93^{+0.02}_{-0.02}$	$0.75^{+0.01}_{-0.01}$	$0.96^{+0.02}_{-0.02}$	0.99/77
10	$7.17^{+0.03}_{-0.02}$	$0.52^{+0.04}_{-0.07}$	$11.6^{+0.4}_{-0.5}$	$4.8^{+0.9}_{-0.9}$	61^{+12}_{-12}	$7.8^{+0.5}_{-0.3}$	$0.27^{+0.03}_{-0.03}$	$3.1^{+0.2}_{-0.2}$	$0.95^{+0.02}_{-0.02}$	$0.75^{+0.01}_{-0.01}$	$0.87^{+0.02}_{-0.02}$	1.11/77
11	$5.76^{+0.02}_{-0.02}$	$0.52^{+0.04}_{-0.07}$	$10.7^{+0.4}_{-0.5}$	$3.9^{+0.8}_{-0.8}$	61^{+12}_{-12}	$8.0^{+0.4}_{-0.3}$	$0.21^{+0.02}_{-0.02}$	$3.0^{+0.2}_{-0.2}$	$0.97^{+0.02}_{-0.02}$	$0.76^{+0.01}_{-0.01}$	—	1.17/48
12	$4.33^{+0.02}_{-0.02}$	$0.56^{+0.06}_{-0.10}$	$10.5^{+0.6}_{-0.7}$	$2.6^{+0.6}_{-0.6}$	53^{+12}_{-12}	$8.2^{+0.3}_{-0.3}$	$0.18^{+0.02}_{-0.02}$	$3.0^{+0.2}_{-0.2}$	$0.96^{+0.01}_{-0.01}$	$0.73^{+0.01}_{-0.01}$	—	1.10/48
13	$2.84^{+0.02}_{-0.02}$	$0.59^{+0.06}_{-0.16}$	$9.6^{+0.5}_{-0.9}$	$1.9^{+0.5}_{-0.5}$	55^{+13}_{-14}	$7.9^{+0.6}_{-0.6}$	$0.13^{+0.02}_{-0.02}$	$3.1^{+0.2}_{-0.3}$	$0.95^{+0.02}_{-0.02}$	$0.72^{+0.02}_{-0.02}$	$0.86^{+0.03}_{-0.03}$	0.96/81
14	$1.40^{+0.02}_{-0.02}$	$0.41^{+0.22}_{-0.28}$	$8.3^{+1.2}_{-1.2}$	$0.6^{+0.5}_{-0.3}$	35^{+27}_{-17}	$8.5^{+0.5}_{-0.7}$	$0.04^{+0.03}_{-0.02}$	$3.0^{+0.5}_{-0.7}$	$0.98^{+0.02}_{-0.02}$	$0.69^{+0.04}_{-0.04}$	$0.44^{+0.03}_{-0.03}$	0.86/81

ep^a	E_0 [keV]	W_0 [keV]	τ_0	E_1 [keV]	W_1 [keV]	τ_1	E_2 [keV]	τ_2	E_3 [keV]	τ_3	E_4 [keV]	τ_4
1	$11.0^{+0.4}_{-0.8}$	$0.9^{+3.9}_{-0.9}$	$0.04^{+0.02}_{-0.02}$	$21.6^{+0.3}_{-0.3}$	$0.9^{+1.0}_{-0.4}$	$0.24^{+0.18}_{-0.07}$	—	—	—	—	—	—
2	$11.2^{+0.5}_{-0.6}$	$0.8^{+2.4}_{-0.3}$	$0.03^{+0.02}_{-0.02}$	$22.1^{+0.3}_{-0.3}$	$2.6^{+1.0}_{-0.9}$	$0.24^{+0.03}_{-0.03}$	$32.7^{+1.3}_{-1.3}$	$0.25^{+0.07}_{-0.07}$	$42.8^{+2.5}_{-2.2}$	$0.26^{+0.09}_{-0.08}$	—	—
3	$11.1^{+0.5}_{-0.5}$	$0.5^{+1.3}_{-0.0}$	$0.03^{+0.02}_{-0.02}$	$22.0^{+0.2}_{-0.2}$	$0.5^{+0.8}_{-0.0}$	$0.26^{+0.05}_{-0.05}$	$37.5^{+1.0}_{-1.0}$	$0.20^{+0.05}_{-0.05}$	—	—	—	—
4	$11.0^{+0.5}_{-0.7}$	$0.8^{+2.4}_{-0.3}$	$0.03^{+0.02}_{-0.02}$	$21.8^{+0.3}_{-0.3}$	$1.1^{+0.9}_{-0.6}$	$0.19^{+0.16}_{-0.05}$	$36.4^{+1.0}_{-1.2}$	$0.22^{+0.07}_{-0.07}$	—	—	—	—
5	$11.0^{+0.6}_{-0.7}$	$2.5^{+1.5}_{-1.5}$	$0.12^{+0.15}_{-0.07}$	$22.1^{+0.6}_{-0.6}$	$1.4^{+2.3}_{-0.9}$	$0.18^{+0.24}_{-0.07}$	$36.2^{+1.8}_{-1.8}$	$0.18^{+0.09}_{-0.08}$	—	—	—	—
6	$10.7^{+0.3}_{-0.4}$	$1.8^{+1.0}_{-1.2}$	$0.11^{+0.14}_{-0.07}$	$21.8^{+0.4}_{-0.4}$	$4.8^{+0.9}_{-0.9}$	$0.46^{+0.05}_{-0.05}$	$35.2^{+0.7}_{-2.0}$	$0.48^{+0.07}_{-0.08}$	$46.7^{+1.2}_{-2.0}$	$0.44^{+0.10}_{-0.13}$	$59.7^{+2.0}_{-3.2}$	$0.52^{+0.24}_{-0.25}$
7	$10.7^{+0.2}_{-0.3}$	$2.3^{+0.9}_{-0.9}$	$0.18^{+0.14}_{-0.08}$	$22.1^{+0.2}_{-0.2}$	$3.8^{+0.6}_{-0.5}$	$0.45^{+0.05}_{-0.03}$	$33.3^{+0.9}_{-0.8}$	$0.35^{+0.06}_{-0.07}$	$41.6^{+1.4}_{-1.6}$	$0.34^{+0.08}_{-0.08}$	$52.8^{+1.8}_{-2.0}$	$0.42^{+0.13}_{-0.14}$
8	$10.6^{+0.3}_{-0.3}$	$2.3^{+0.8}_{-0.7}$	$0.16^{+0.08}_{-0.05}$	$21.8^{+0.3}_{-0.3}$	$2.9^{+0.8}_{-0.7}$	$0.30^{+0.04}_{-0.04}$	$34.9^{+1.0}_{-0.4}$	$0.25^{+0.06}_{-0.05}$	—	—	—	—
9	$10.5^{+0.3}_{-0.3}$	$2.1^{+0.9}_{-0.7}$	$0.12^{+0.07}_{-0.04}$	$21.6^{+0.4}_{-0.4}$	$2.7^{+1.2}_{-0.9}$	$0.22^{+0.04}_{-0.03}$	$33.2^{+1.2}_{-1.3}$	$0.25^{+0.06}_{-0.06}$	$43.7^{+2.0}_{-1.7}$	$0.28^{+0.08}_{-0.07}$	—	—
10	$10.3^{+0.4}_{-0.5}$	$2.0^{+1.2}_{-0.9}$	$0.09^{+0.10}_{-0.04}$	$21.4^{+0.5}_{-0.5}$	$3.9^{+1.4}_{-1.0}$	$0.25^{+0.04}_{-0.04}$	$34.0^{+1.3}_{-1.0}$	$0.31^{+0.07}_{-0.07}$	$44.0^{+2.3}_{-1.9}$	$0.28^{+0.09}_{-0.08}$	—	—
11	$10.3^{+0.4}_{-0.4}$	$2.1^{+1.0}_{-1.0}$	$0.10^{+0.10}_{-0.05}$	$21.3^{+0.4}_{-0.4}$	$2.9^{+1.6}_{-1.0}$	$0.21^{+0.05}_{-0.03}$	$33.0^{+2.4}_{-1.5}$	$0.22^{+0.08}_{-0.07}$	—	—	—	—
12	$10.1^{+0.3}_{-0.4}$	$2.3^{+1.0}_{-0.9}$	$0.14^{+0.13}_{-0.06}$	$20.8^{+0.3}_{-0.4}$	$2.3^{+1.0}_{-0.8}$	$0.21^{+0.05}_{-0.04}$	$34.6^{+1.8}_{-1.9}$	$0.20^{+0.10}_{-0.08}$	—	—	—	—
13	$10.2^{+0.4}_{-0.5}$	$1.7^{+1.7}_{-1.0}$	$0.08^{+0.13}_{-0.06}$	$20.7^{+1.4}_{-2.2}$	$2.6^{+5.0}_{-2.1}$	$0.08^{+0.13}_{-0.05}$	—	—	—	—	—	—
14	$10.7^{+0.5}_{-0.8}$	$0.5^{+4.0}_{-0.0}$	$0.06^{+0.04}_{-0.03}$	$20.3^{+1.6}_{-1.4}$	$5.9^{+2.8}_{-3.2}$	$0.38^{+0.19}_{-0.19}$	—	—	—	—	—	—

Uncertainties and upper limits are at the 90% confidence level for one interesting parameter. ^{a} Epoch for data grouping (see text for details). ^{b} Absorbed luminosity in units of 10^{37} erg s^{-1}. L_x covers the energy band 3–50 keV and was calculated using a distance of 7 kpc (Negueruela & Okazaki, 2001). ^{c} In units of photons s^{-1} cm^{-2}.
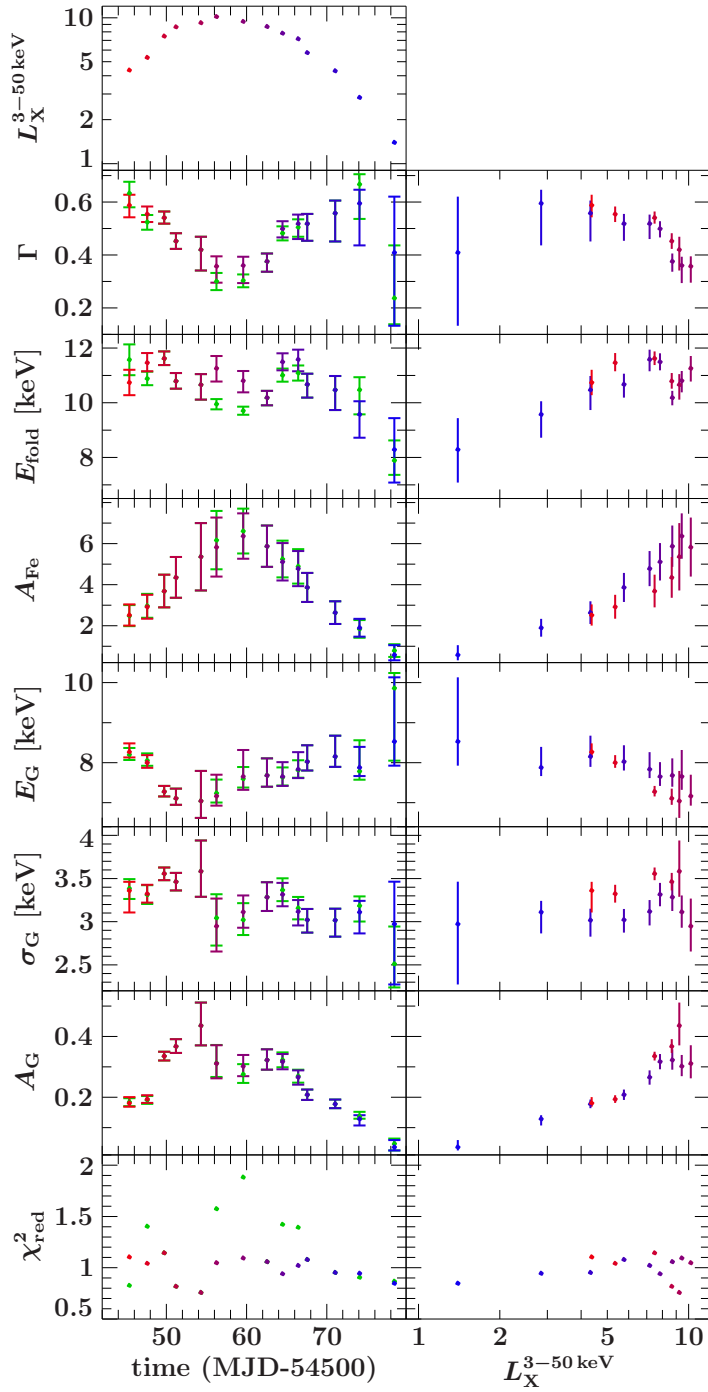
Figure 5.5: Left, temporal evolution and right, luminosity dependence of the continuum parameters (see text for definitions) and 10 keV feature for the fits with the `CutoffPL` continuum. The color gradient from reddish to bluish data points indicates the temporal evolution of the outburst. The data points show results from the initial fit run, where a variable number of cyclotron lines was used. Green data points in the left column correspond to the second fit run with a fixed number of three cyclotron lines (only in the left column), which was been performed as a consistency check (see text for details). Where no green points are visible, both fits gave the same results. L_X is in units of $10^{37}\,\mathrm{erg\,s^{-1}}$. A_G and A_{Fe} are in units of $\mathrm{photons\,s^{-1}\,cm^{-2}}$, while A_{Fe} is in multiples of 10^{-3}.
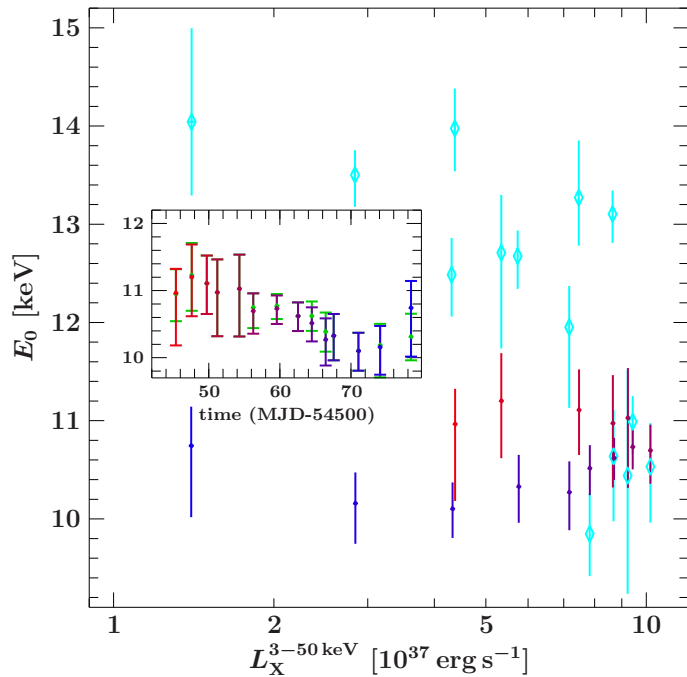
Figure 5.6: Luminosity and time dependence (inset) of the energy of the fundamental CRSF using the `CutoffPL` continuum model. The color coding is the same as in Fig. 5.5. Cyan data points (diamonds) show the results when using the `NPEX` continuum.

fied with the 10 keV feature. In these fits, the width W_0 remains constant throughout the outburst, and there is only a slight ($\sim 3\sigma$) indication that the optical depth τ_0 was somewhat shallower during the initial phases of the outburst, before $\sim$MJD 54552, although it cannot be excluded that some of this effect is due to a correlation with the "10 keV feature", which during this time of the outburst peaks close to the cyclotron line at around 8 keV. Most importantly, however, as shown in Fig. 5.6 the energy of the fundamental cyclotron line is only very slightly variable: during early phases of the outburst the line is around 11 keV, moving towards 10 keV as the outburst progressed. This result is contrary to all earlier studies of outbursts of 4U 0115+634, where strong changes in the line energy were seen (e.g., Mihara et al., 2004; Nakajima et al., 2006; Tsygankov et al., 2007; Li et al., 2012).

Where does this difference in line behavior come from? As discussed in Sects. 2.6.1 and 5.3.1 a large variety of continuum models can be used to describe the broad band spectra of accreting neutron stars. Due to the early successes of fitting spectra of 4U 0115+634 with the `NPEX` and `PLCUT` models, these continua have been extensively used when modeling the outburst behavior of this pulsar. Unfortunately, however, in most previous analyses – including some of our own – no attempt was made at modeling the data with any of the other available models.

For example, modeling the 2008 outburst of 4U 0115+634 with the `NPEX` model (following Nakajima et al., 2006, fixing Γ_2 to 2.0) results in fits that are of only slight worse quality as those using the `CutoffPL` model modified by the 10 keV feature, and we can recover the strong variation of the cyclotron line found in earlier analyses (Fig. 5.6, cyan data points)[2]. Depending on the choice of the continuum, we therefore find a fundamentally different behavior of the fundamental cyclotron line, especially the centroid energy.

Given that the fits with `NPEX` and `CutoffPL` give similarly good results, what is

---

[2]As explained in Sect. 2.6.1, modeling the spectra with the `PLCUT` model results in an unphysical break around the energy of the fundamental line, we therefore consider this continuum to be unsuitable for studying the cyclotron line behavior.
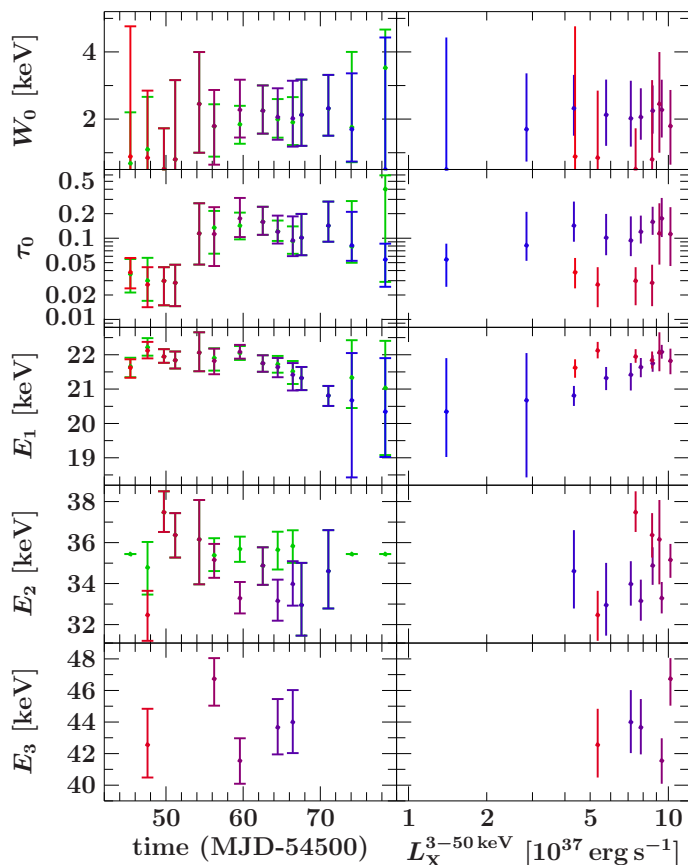
Figure 5.7: Time (left) and luminosity (right) dependence of the parameters of the CRSF. The color coding is the same as in Fig. 5.5.

the fundamental difference between both modeling approaches? **NPEX** models generally result in very broad cyclotron lines, with W_0 and W_1 often exceeding 5 keV (e.g., Nakajima et al., 2006, runs using the **PLCUT** model give similar results, see, e.g., Li et al., 2012). In contrast, using the **CutoffPL** continuum with the 10 keV feature results in widths of typically less than 3 keV, much more consistent with the narrow shapes of the residuals shown in Fig. 5.2. When lines are as broad as in the **NPEX** fits, they can influence the continuum fit. To illustrate how strongly these features distort the continuum, Fig. 5.8 shows the continuum shape inferred when setting τ_0, τ_1, τ_2, and τ_3 to zero. The residuals for the **CutoffPL** continuum with the 10 keV feature (dark blue) show sharp absorption dips at the cyclotron line energies of the fundamental and first harmonic line energies. For the **NPEX** model (green line), on the other hand, it is obvious that rather than describing narrow cyclotron lines, the multiplicative broad line model strongly influences the continuum. As discussed above, our spectral fits show that during the brightest phases of the outburst a significant hardening of the continuum emission is observed, together with a change of the exponential cutoff. While this is also seen in the variation of the continuum parameters, it is very likely that the luminosity dependence of the CRSF in the **NPEX** fits is due to the line partially modeling this behavior of the continuum, and not a real physical effect.

Using the results from the **CutoffPL** plus 10 keV feature fits for the line energy also solves another problem found in earlier spectral modeling. Here, using **NPEX** fits, the ratios between the fundamental and higher cyclotron lines were often found to deviate significantly from integers. While slightly non-integer ratios are expected when taking relativistic quantum mechanics into account (see the discus-
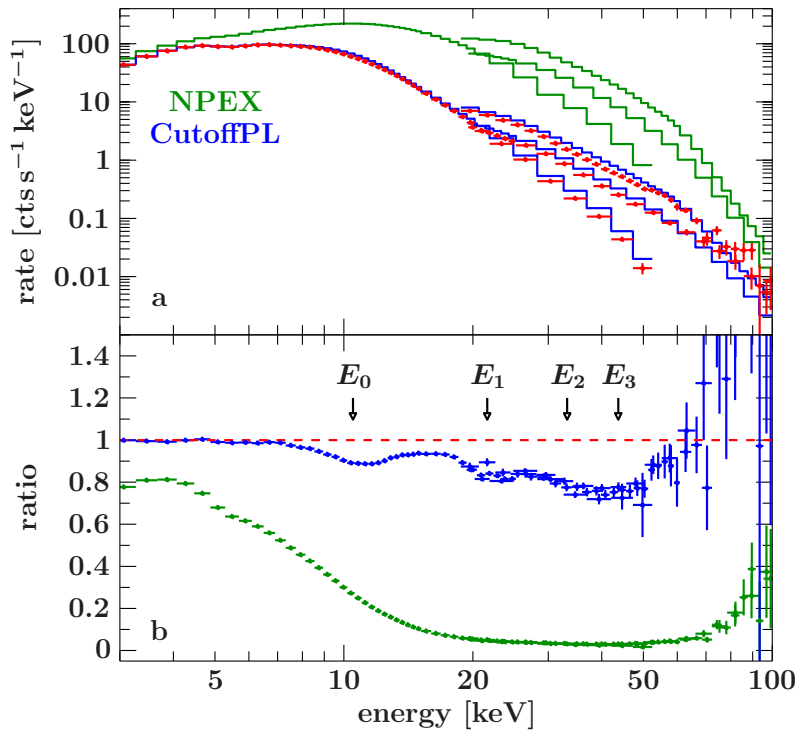
Figure 5.8: a: PCA, HEXTE, and ISGRI spectra from epoch 9 (red) together with the best fit models using the **NPEX** (green) and **CutoffPL** (blue) continua after setting the optical depth of the cyclotron lines to zero. b: Ratio between the data and the model.

sion by Pottschmidt et al., 2005), the large deviations from integer multiples seen previously (e.g., Santangelo et al., 1999; Heindl et al., 1999; Nakajima et al., 2006; Tsygankov et al., 2007) require rather complex model assumptions which introduce second order effects such as strong vertical B-field gradients, crustal field structures on small scales, or thermomagnetic effects for their explanation (see Schönherr et al., 2007, and references therein for a discussion). Figure 5.9 shows that we can recover these non-integer ratios in our **NPEX** fits, but when using the **CutoffPL** plus 10 keV feature model, these ratios are mostly in agreement with integer values, or at least only slightly higher, as expected from the most simple models for cyclotron line formation. We conclude that, also from a physical point of view, the **CutoffPL** continuum with the 10 keV feature gives a much more satisfactory description of the data.

Finally, we check the dependence of the line position on other free fit parameters when using the **CutoffPL** continuum modified by the 10 keV feature. Since the origin of the 10 keV feature remains still an open question, possible relations between the CRSF centroid energy and the parameters of the 10 keV feature have to be investigated, and other continuum parameters such as E_{fold} or Γ could influence the results for the cylotron line parameters. Figure 5.10 shows the behavior of $\Delta\chi^2$ in the vicinity of the best fit values for three epochs representative for the early phase, peak, and late phase of the 2008 outburst for selected combinations of important fit parameters. These contour plots show that the line energy is not affected by cross correlations with other parameters, i.e., possible variations in the line energy of the fundamental cyclotron line are not due to variations observed in the parameters of the 10 keV feature or the continuum parameters.

In contrast to the stable behavior of the line when using **CutoffPL** with a 10 keV feature, Fig. 5.11 illustrates the dependence of the CRSF centroid energy on the continuum parameters of the **NPEX** model. In many cases, strong correlations between E_0 and Γ_1 as well as between E_0 and E_{fold} are present. These correlations are a further indicator that the Lorentzian component is used to model the continuum rather
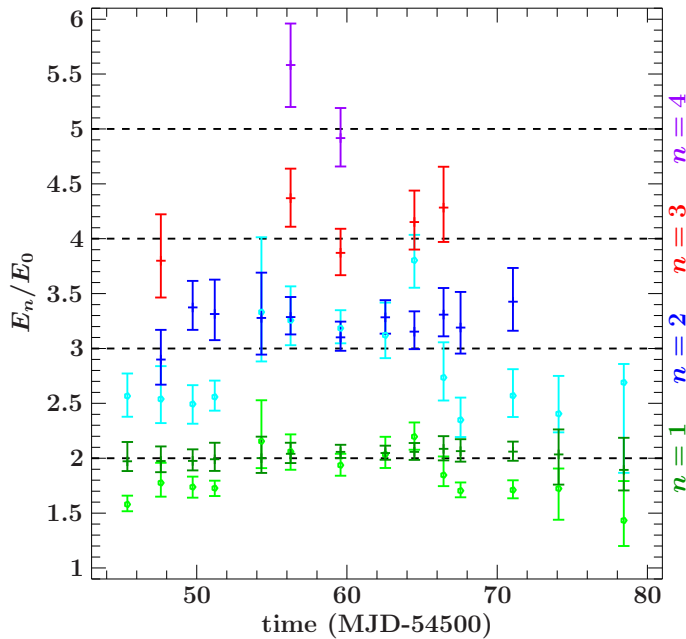
Figure 5.9: Ratios of the cyclotron line energies E_n/E_0 with respect to the centroid energy of the fundamental line against time. The dark green, dark blue, red and purple data points (bars) correspond to E_1/E_0, E_2/E_0, E_3/E_0, and E_4/E_0, respectively, using the **CutoffPL** continuum with a 10 keV feature. The light green and cyan data points (filled circles) show the results for E_1/E_0 and E_2/E_0 using **NPEX**. The dashed lines indicate integer values for these ratios.

than a cyclotron line when using the **NPEX** model.

5.5   4U 0115+634 with *Suzaku*

V ERIFYING new results as reported in this Sections by other datasets is an important validy check. For this purpose, we used two *Suzaku* observations of the outburst in 2011 June/July.

5.5.1   Observations and Data Reduction

As displayed in Fig. 5.12, the outburst lasted about 40 days, exceeding a flux of $\sim$300 mCrab in the 15–50 keV band. *Suzaku* observed 4U 0115+634 on July 5 and July 8 with exposure times of 24 ksec and 42 ksec, respectivley. A detailed description of the data extraction process is given in Hertel (2013).

We used data from XIS0 and 3 in the energy range 1.5–9 keV. Because of a mismatch between XIS1 and the other XIS spectra at energies $\gtrsim$8 keV caused by a higher level of background for XIS1, we used only data in the energy range 1.5–8 keV. Due to known Si and Au calibration features at energies 1.72–1.88 keV and 2.19–2.37 keV, we excluded these ranges for all XIS spectra (Nowak et al., 2011). We use data from the PIN instrument in the energy range 16–55 keV. Because of the insufficient S/N, we did not use the data from the GSO instrument of the HXD. For the analysis, the PIN and the XIS spectra were rebinned to a S/N of 5 and 140, respectively.

5.5.2   Spectral Analysis

We used the same approach as for the 2008 outburst to model the X-ray spectra of 4U 0115+634: an absorbed cutoff power-law plus a broad Gaussian emission feature around 10 keV. Furthermore, we accounted for an Fe Kα fluorescence line at 6.4 keV, and multiplied the continuum with pseudo-Lorentzian profiles to model the CRSFs. Since the flux normalizations of the different instruments are not perfectly known,
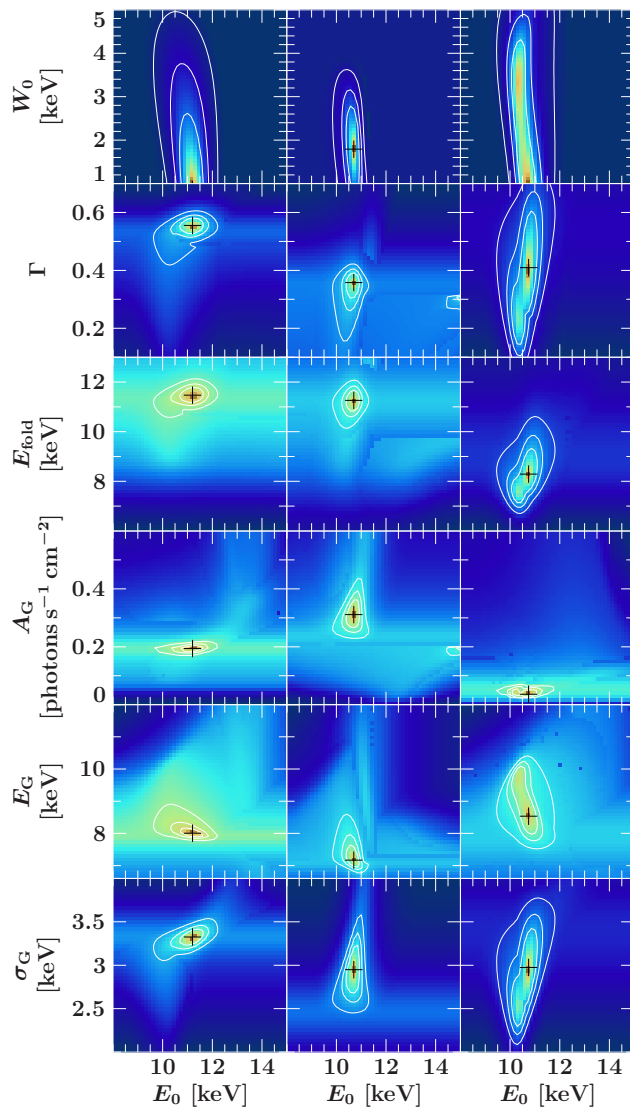
Figure 5.10: Confidence contours between the fundamental CRSF energy and other fit parameters. The columns show the results for epochs 2, 6, and 14, respectively. Contour lines correspond to the 68.3%, 90%, and 99% confidence levels. Color indicates $\Delta\chi^2$ with respect to the best fit value, with the color scale running from orange (low $\Delta\chi^2$) to dark blue (large $\Delta\chi^2$).
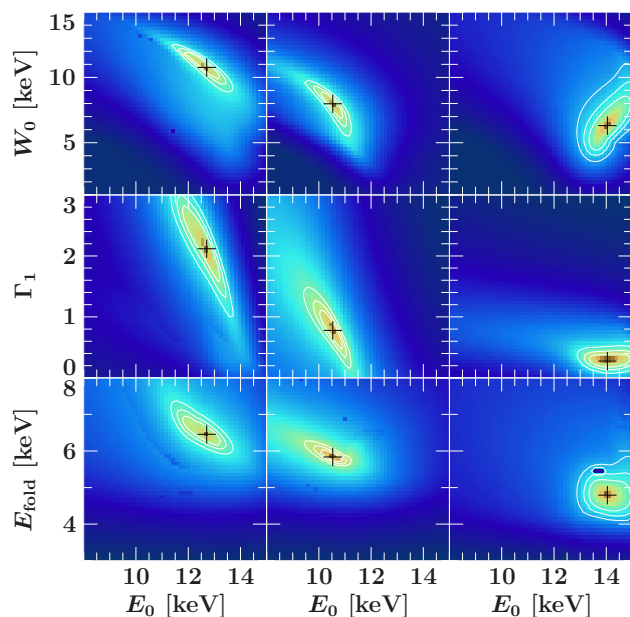
Figure 5.11: Confidence contours between the fundamental cyclotron line energy and continuum parameters when using the **NPEX** model. The displayed epochs, colors and lines are the same as in Fig. 5.10.
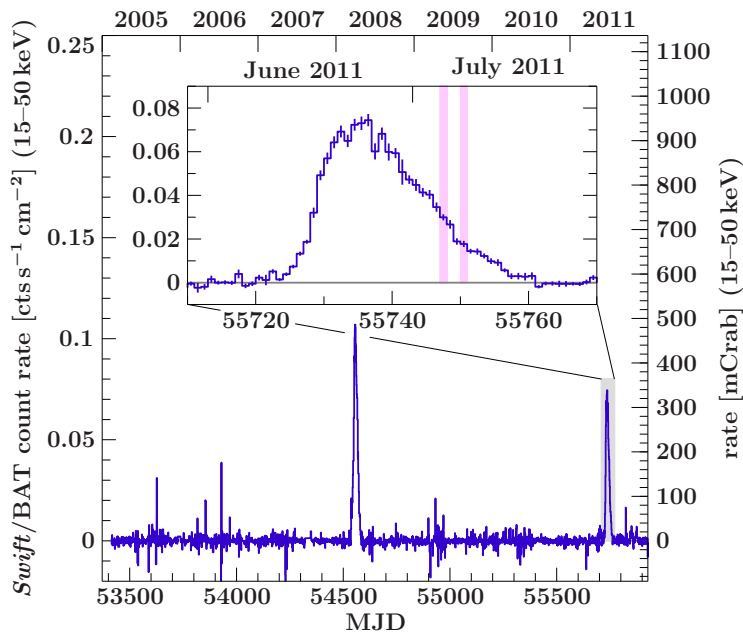
Figure 5.12: *Swift*/BAT light curve of 4U 0115+634 (15–50 keV). The inset shows a close-up view on the 2011 outburst. The shaded regions in the inset indicate the times of pointed *Suzaku* observations.

we introduce the cross calibration constants c_{XIS0}, c_{XIS1}, c_{XIS3}, and c_{PIN}, where we chose PIN to be the reference instrument and thus froze its calibration constant to 1.

Initial fits without taking cyclotron features into account result in absorption like residuals around $\sim$22 keV and $\sim$33 keV for epoch 1 (epoch 1 and 2 correspond to the two *Suzaku* pointings performed on 2011, July 5, and July 8, respectively, as displayed in Fig. 5.13). We added two cyclotron line features to our model at these energies. Since the fundamental cyclotron line is expected to be located at $\sim$11 keV (as we found for the 2008 outburst), the main problem of studying this feature with *Suzaku* is the data gap between XIS and PIN, i.e., between 9 and 16 keV. Nonetheless, to study the influence of the fundamental CRSF, we performed two fit runs. In the first run we did not account for the fundamental cyclotron line. In the second run we added the fundamental line to our model and used the result from the 2008 outburst that the line ratio E_1/E_0 is consistent with 2.0 for all observed flux levels. We fixed E_0 to half of E_1 from the first fit run. The width and depth of the fundamental cyclotron line were frozen to the mean values from the outburst from 2008, i.e., $\tau_0 = 0.1$ and $W_0 = 2$ keV. Note that adding the fundamental line to the model does not change the best fit value for E_1 significantly. In both fit runs we had to freeze the width of the first and second harmonic to typical values as obtained from the 2008 outburst, i.e., 2 keV and 4 keV, respectively, as these widths cannot be well constrained. Caused by the lower count rate in epoch 2 and the resulting decrease of the statistics, we furthermore had to freeze the centroid energy of the second harmonic to the result obtained from epoch 1. The results of fit run two are summarized in Table 5.3. Both fit runs result in fits of equal quality in terms of χ^2_{red}. The resulting spectral fits are displayed in Fig. 5.13.

5.5.3   Discussion of the Results from *Suzaku*

For the 2008 outburst, we found variability of the spectral shape, i.e., significant changes of the photon index as well as for the parameters of the 10 keV feature. Because of the similar flux level, we find, not unexpectedly, no evidence for a change of the spectral shape for the two *Suzaku* observations performed in the fading phase.
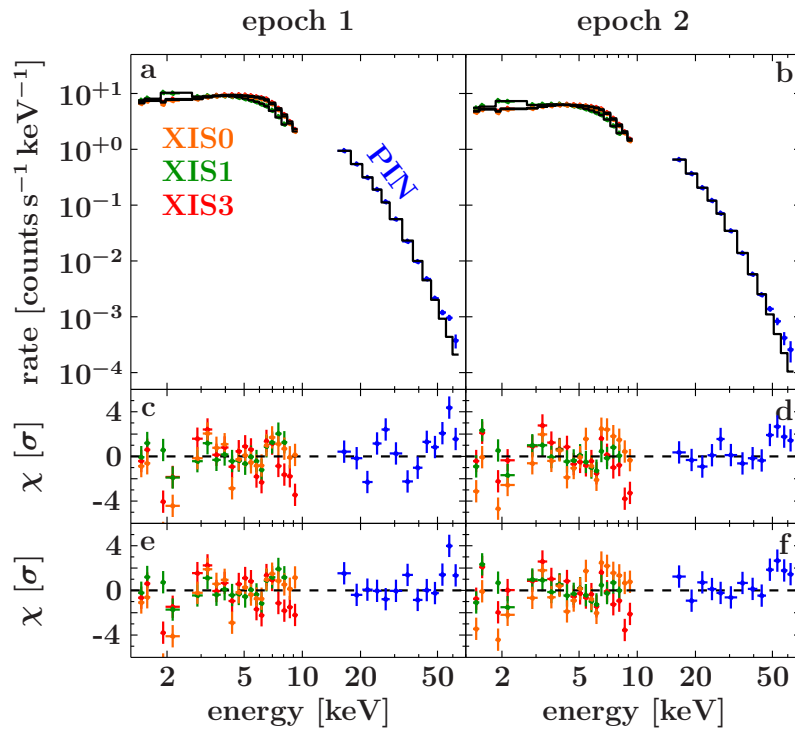
Figure 5.13: Panels a and b show simultaneous spectral fits of 4U 0115+634. The histograms show the best-fit continuum. Panels c and d show the behavior of the residuals when no cyclotron line is added to the spectral model. Panels e and f display the residuals of the best fit using a model including three cyclotron line features. For better visibility, the spectra have been binned stronger for this plot than for the spectral fits.

For GRO J1008–57, Kühnel et al. (2013) found that, even for different outbursts, the spectral shape depends only on one parameter: the X-ray flux. Studying the temporal behavior of the spectral shape during the complete 2011 outburst is not possible as no *Suzaku* observations were performed during the rising and maximum phase of the outburst. In order to test whether the spectral continuum changes for different outbursts and depends only on the flux level, as found by Kühnel et al. (2013), we compared the fit results from the 2011 outburst to those from 2011 at the same flux level. This is possible, because the same model has been used for both analyses. For this purpose we used the epochs 1, 12, and 13 from Table 5.2. We find that many of the spectral parameters are indeed consistent with each other or deviate only slightly.

With values typically around 80 eV, the equivalent width of the Fe Kα fluorescence line is slightly higher in 2011 than in 2008 (where $W \approx 35 - 60$ eV), indicating the possibility of a larger amount of fluorescent material in the binary system. Unfortunately, due to the higher low energy cutoff of the PCA data, the results for N_{H} from the 2008 outburst have too large uncertainties to be compared with the 2011 values to verify this speculation.

Besides this parameter, there are two continuum parameters which are significantly different between the outbursts in 2008 and 2011, the photon index, Γ, and the centroid energy of the 10 keV feature, E_{G}. While Γ is typically 0.6 ± 0.1 in 2008, with typicalle 0.30 ± 0.06, it is significantly harder in 2011. Also, E_{G} typically ranged at about 8 keV in 2008, while in 2011 it is located at significantly higher energies around 9 keV. These results indicate a difference of the spectral shape between the outbursts in 2008 and 2011, even at the same flux level. The model of the background of PCA, with a FoV of 1°, is calculated without accounting for the Galactic ridge emission. Thus, for sources located in the Galactic plane, the PCA is known to be affected by the emission of the Galctic ridge at energies between about 2 and 10 keV (Müller et al., 2012, and references therein), while for *Suzaku* spectra this emission is corrected by background measurements of the focussing optics. Furthermore, different

Table 5.3: Continuum parameters of the spectral analysis. Fits were performed with an absorbed `CutoffPL` model, a 10 keV feature, a Fe Kα fluorescence line.

epoch	L_X^a	N_H [10^{22} cm^{-2}]	Γ	$E_{\rm fold}$ [keV]	$A_{\rm Fe}^b$ [10^{-3}]	$W_{\rm Fe}$ [eV]	E_G [keV]	A_G^b	σ_G [keV]
1	$3.89^{+0.15}_{-0.16}$	$1.53^{+0.08}_{-0.07}$	0.32 ± 0.06	$9.3^{+0.5}_{-0.4}$	$3.0^{+1.0}_{-0.8}$	83^{+38}_{-24}	9.3 ± 0.4	$0.116^{+0.016}_{-0.014}$	3.0 ± 0.2
2	2.64 ± 0.10	$1.40^{+0.07}_{-0.06}$	0.27 ± 0.06	$8.5^{+0.5}_{-0.4}$	$1.9^{+0.6}_{-0.4}$	76^{+26}_{-18}	9.4 ± 0.3	$0.082^{+0.010}_{-0.009}$	3.1 ± 0.2

epoch	E_0 [keV]	E_1 [keV]	τ_1	E_2 [keV]	τ_2	$c_{\rm XIS0}$	$c_{\rm XIS1}$	$c_{\rm XIS3}$	$\chi^2_{\rm red}$/dof
1	10.5 ± 0.3	21.0 ± 0.5	0.15 ± 0.06	$33.2^{+1.5}_{-1.4}$	0.16 ± 0.06	$0.99^{+0.10}_{-0.08}$	$1.08^{+0.10}_{-0.09}$	$1.00^{+0.10}_{-0.08}$	1.30/487
2	10.7 ± 0.4	21.5 ± 0.7	0.14 ± 0.06	33.2 (fix)	0.09 ± 0.08	$0.97^{+0.09}_{-0.08}$	$1.08^{+0.10}_{-0.09}$	$0.98^{+0.09}_{-0.08}$	1.26/628

Uncertainties and upper limits are at the 90% confidence level for one interesting parameter. For E_0, the uncertainty has been calculated by error propagation of the uncertainty of E_1.
^{a} Absorbed luminosity in the energy band 3–50 keV in units of 10^{37} erg s^{-1}, calculated using a distance of 7 kpc (Negueruela & Okazaki, 2001). ^{b} In units of photons s^{-1} cm^{-2}.

energy bands for different instruments could cause deviations for the same fit parameter. Additionally, calibration uncertainties of the reference instruments could lead to uncertainties in, e.g., the flux determination. It cannot be excluded that the differences in the spectra could possibly be caused by these reasons.

Because of these issues, conclusions whether the shape of the 2011 *Suzaku* spectrum of 4U 0115+634 of 2011 is different to the shape of the 2008 outburst at the same luminosity level are at this point not possible. This question could be answered when performing further monitoring observation in future, covering several giant outbursts of 4U 0115+634. Alternatively, studying archived data taken during many years of comparable instruments allows for the comparison of the spectral shape over different outbursts.

The cyclotron lines' parameters from our *Suzaku* analysis are not in disagreement with the results obtained from the *RXTE* spectra of the 2008 outburst. Figure 5.14 displays the results for the fundamental cyclotron line energy from both datasets. The discussion about the implications of these results for the cyclotron lines' parameter are given in the next Sect. 5.6.

5.6 Conclusions

WE have presented a study of the 2008 outburst of 4U 0115+634 based on *RXTE* and *INTEGRAL* data (Fig. 5.1). We reproduced the results from previous work (e.g., Nakajima et al., 2006; Tsygankov et al., 2007; Li et al., 2012, and others) that the spectra can be successfully modeled by, e.g., the `NPEX` model. We showed that for these fits the very broad absorption features, which are thought to describe the CRSFs, rather model the broadband continuum. Our result that the continuum parameters are strongly variable over the outburst (Fig. 5.5), could be responsible for the change in the cyclotron line energy in these fits.

We have shown that the spectral continuum can be also well described with a model introduced by Klochkov et al. (2007) for EXO 2030+375 and Ferrigno et al. (2009) for 4U 0115+634, i.e., the `CutoffPL`, modified by strong Gaussian emission feature around 10 keV and several (up to five) cyclotron lines (Table 5.2 and Fig. 5.4). Furthermore, this model also gives a well description of *Suzaku* observations of an outburst in 2011. Due to an unphysical break close to the energy of the fundamental cyclotron line, the `PLCUT` model does not give a physical description of the continuum. Using the `CutoffPL` together with the 10 keV feature, we have shown that the modeling of lines reflects the theoretical expectation in both the line shape and the
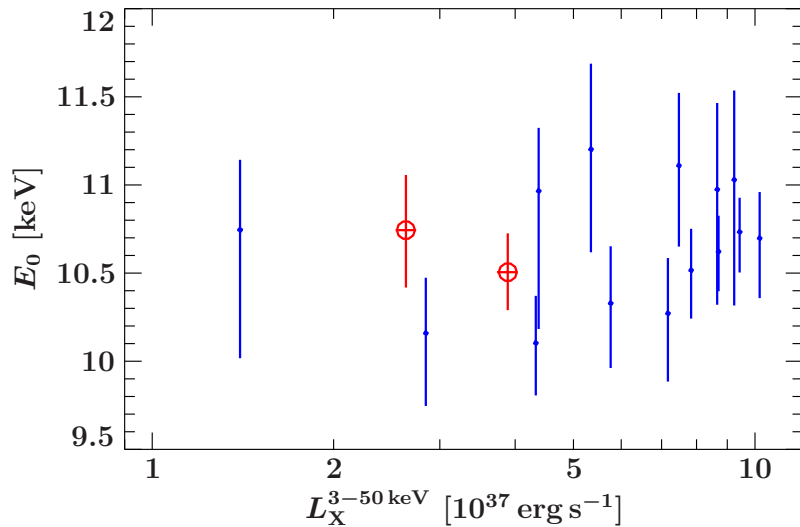
Figure 5.14: X-ray luminosity over centroid energy of the fundamental cyclotron line. Blue data points display the results from the 2008 outburst of 4U 0115+634, while red circles indicate the results from the 2011 outburst, assuming that $E_0 = \frac{1}{2}E_1$.

ratios of the harmonics. In this model, the luminosity dependency of the centroid energy is not present. As shown also by Ferrigno et al. (2011), the line centroid energy is remarkably stable throughout the brightest phase of the outburst. Here we show that such stability is present, albeit at lower significance, also during the early and late phases. Boldin et al. (2013) recently confirmed the dependance of the cyclotron line behavior on the underlying continuum model based on an analysis of archival data of several instruments.

This result is also obtained from the 2011 outburst as observed with *Suzaku* (see Fig. 5.14). In this model, the continuum variations are explained by a slight anticorrelation of the centroid energy of the Gaussian feature with luminosity and a significant variation of Γ.

The strong systematic influence of the chosen continuum on the cyclotron line behavior illustrates a problem that is potentially inherent to all cyclotron line measurements. We emphasize, however, that this does not mean that the general picture of the different regimes of magnetized neutron star accretion and general luminosity dependence of the cyclotron line as outlined by Becker et al. (2012, and references therein) is incorrect. In the sample of sources discussed by Becker et al. (2012), 4U 0115+634 was an outlier. The change of line energy inferred from the **NPEX** and **PLCUT** models was almost a jump at a 3–50 keV luminosity of around 3×10^{37} erg s^{-1} and strong hysteresis effects were present (Fig. 5.6). Such a behavior has not been seen in any of the other cyclotron line sources. The second strongest luminosity-dependent cyclotron line variability is observed in V0332+53 (Mowlavi et al., 2006; Tsygankov et al., 2006; Nakajima et al., 2010), in which the cyclotron lines are so strong that the change can be seen by eye even in the raw detector spectra. While the boundaries between the different accretion regimes estimated by Becker et al. (2012) might therefore have to be adjusted, the overall principal behavior of the accretion column discussed by these authors still holds.

Chapter 6

GX 304−1

F INALLY we present an analysis of the 2011 April/May outburst of the HMXB GX 304−1. We performed a spectral study of this system, which was monitored regularly through this outburst by *RXTE*. This work will be submitted to the journal *Astronomy & Astrophysics* in the near future. A few parts of the work on GX 304−1, especially the spectral fits, were performed within a collaboration of my summer student Jieun Choi (University of California, Berkeley Astronomy Department), who spent the summer 2011 at the Remeis observatory in Bamberg.

6.1 Introduction

T HE system GX 304−1, detected in 1967 by a balloon experiment (Lewin et al., 1968), has a Be-type companion star (Mason et al., 1978) and shows X-ray pulsations of ∼272 s (McClintock et al., 1977). Remaining in states of quiescence as, e.g., between 1980 and 2008, and showing regular outbursts with intervals of 132.5 ± 0.4 d (Priedhorsky & Terrell, 1983) otherwise, makes GX 304−1 a prime example of sources with a highly unpredictable outburst behavior (Manousakis et al., 2008; Klochkov et al., 2012). GX 304−1 is an X-ray source which exhibits a cyclotron line at ∼54 keV (Yamamoto et al., 2011b). Using data from *RXTE* and *Suzaku*, these authors found possible evidence for a positive correlation between the cyclotron line energy and the X-ray flux. Using *INTEGRAL* data, Klochkov et al. (2012) confirmed this correlation and found the line varying between ∼48 keV and ∼55 keV. According to Becker et al. (2012), this correlation indicates that GX 304−1 accretes within the subcritical regime.

In this work we present an analysis of *RXTE* data of an outburst in 2011 April/May.

6.2 Observations and Data Reduction

M *AXI*/GSC detected the onset of an outburst of GX 304−1 on 2011 April 20 (Yamamoto et al., 2011a), when the source reached a flux of 84 ± 5 mCrab (2–20 keV). This outburst, as displayed in Fig. 6.1, was the seventh of a series of Type I outbursts of this source. This outburst was regularly monitored by *RXTE*, from its rising phase until re-entry into quiescence in mid-May. The maximum flux of GX 304−1 during this outburst reached values of ∼1 Crab in the 15–50 keV *Swift*/BAT band.
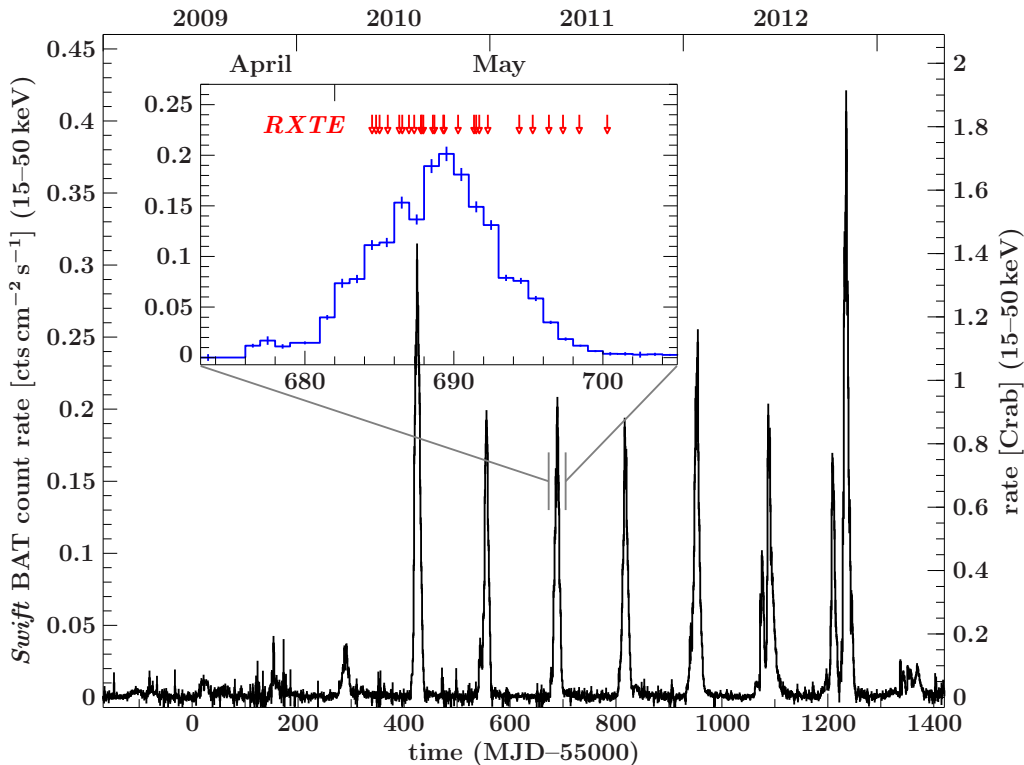
Figure 6.1: 15–50 keV *Swift*/BAT light curve of GX 304−1. The inset provides a closer view on the 2011 April/May outburst. The red arrows indicate the observations times for PCA.

For our analysis we extracted PCA data from PCU2's top layer only (Jahoda et al., 2006) with our standard analysis pipelines which are based on HEASOFT (v. 6.13). We excluded data taken during the passage of the SAA. We analyzed PCA spectra in the **standard2f** mode between 3.5 keV and 50 keV and binned these spectra to obtain a reasonable S/N. A systematic error was added in quadrature, using the canonical values of 0.5% (Jahoda et al., 2006). Light Curves of the **GoodXenon** mode with a resolution of 0.125 s were extracted in the energy bands 2–6 keV and 10–100 keV and were corrected to the barycenter of the solar system. A detailed observation log is given in Table 6.1.

6.3 Continuum Model

W ITH the **CutoffPL** (Sect. 2.6.1, Eq. 2.4), we use for GX 304−1 the simplest model of X-ray spectra of accreting pulsars. This model together with interstellar absorption (as explained in Sect. 2.6.2.1) describes the PCA spectra with low statistics quite well, however, spectra taken during the maximum of the outburst show emission like residuals in the soft energy band below 10 keV (Fig. 6.2b and c). Such features are often caused by soft photons, emitted by the hot spot on the magnetic poles on the neutron star (see Sect. 2.4) and are modeled by the radiation emitted by a black body with a radius R_{BB} and a temperature kT_{BB}. The radius of the black body is calculated assuming a distance of 2.4 ± 0.5 kpc (Parkes et al., 1980). Such soft components were already observed in some X-ray pulsars, as, e.g., RX J0440.9+4431 (La Palombara et al., 2012), or GRO J1008–57 (Kühnel et al., 2013). Additionally, a source intrinsic Fe Kα fluorescence line is required to describe

the observations well (Fig. 6.2b and d). We model this feature with an additional Gaussian feature with a width of 0.1 eV. This is justified, because typically the width of the Fe Kα line is on the order of the resolution of the PCA ($\sim$0.5 keV, Torrejón et al., 2010).

In addition, to account for uncertainties in the background model of the PCA, we introduce a background scaling constant c_b. At first glance, this model leads to a good description of the data (Fig. 6.2f) with respect to χ^2_{red}. However, the background constant results in values typically $(60 \pm 10)\%$. This value is much lower than expected for this background correction constant (e.g., Müller et al., 2013; Kühnel et al., 2013). Thus, this spectral model is not able to describe the data sufficiently and differences between the data and the model are then compensated by undersubtracting the background as shown in the small value of c_b. Fixing this constant to 1 leads to absorption like features at the high energies of PCA (see Fig. 6.2e). Yamamoto et al. (2011b) reported on the discovery of a cyclotron line at $E_{\mathrm{cyc}} \approx 54$ keV and a width of $W \approx 10$ keV. We add a multiplicative feature **CYCLABS** (Eq. 2.15) to our model, fix the energy and width to the value from Yamamoto et al. (2011b), and allow the depth τ to vary. This approach, even with frozen $c_b \overset{!}{=} 1$ leads to a better fit quality (see Fig. 6.2g) compared to the model with a variable c_b. In summary, the model M we use can be written as

$$M = \texttt{tbabs} \times (\texttt{CutoffPL} + \text{black body} + \text{Fe}_{6.4\,\text{keV}}) \times \texttt{CYCLABS}. \tag{6.1}$$

Figure 6.2 provides an example spectrum (ObsID 96369-01-05-02), together with the best continuum model and the residuals when adding the model components one by one.

6.4   Spectral Parameters

USING the model as described by Eq. 6.1 leads to good spectral fits with $0.5 \lesssim \chi^2_{\mathrm{red}} \lesssim 1.3$. The low values for χ^2_{red} are caused by a relatively low S/N of the affected spectra, making the additional model components as the black body or the CRSF unnecessary. However, in order to be able to compare the fit result with each other, we accept these low values for χ^2_{red} and use the same model for all observations. Initial fits have shown a relatively high uncertainty of the folding energy E_{fold}. We therefore fix this value to 17 keV. The results for the fit parameters are given in Table 6.1. Figure 6.3 displays the evolution and the flux dependence of the spectral parameters.

As summarized by, e.g., Reig & Nespoli (2013) for accreting X-ray pulsars, the photon index Γ typically shows a negative correlation with the X-ray flux (here we use the energy range between 3 keV and 50 keV for the flux). We also find this behavior for GX 304−1. Quite remarkabe, however, is the temporal evolution of the hydrogen column density N_{H}. Despite the very low sensitivity of the PCA for this parameter, we detect a significant rise of N_{H} at $55686 \lesssim \mathrm{MJD} \lesssim 55689$, from $\sim 4 \times 10^{22}\,\mathrm{cm}^{-2}$ to values up to about four times larger. The flux of the iron Kα fluorescence line is, as expected (e.g., Torrejón et al., 2010), positively correlated with the X-ray flux. The black body emission shows temporal variabilities as well: the radius is quite constant over the outburst, however, for three ObsIDs we find a significantly lower radius (but see also Sect. 6.5.4). The temperature is higher during the maximum of the outburst, while, additionally, a hysteresis effect is visible. We find no significant temporal variability of the depth of the cyclotron line.
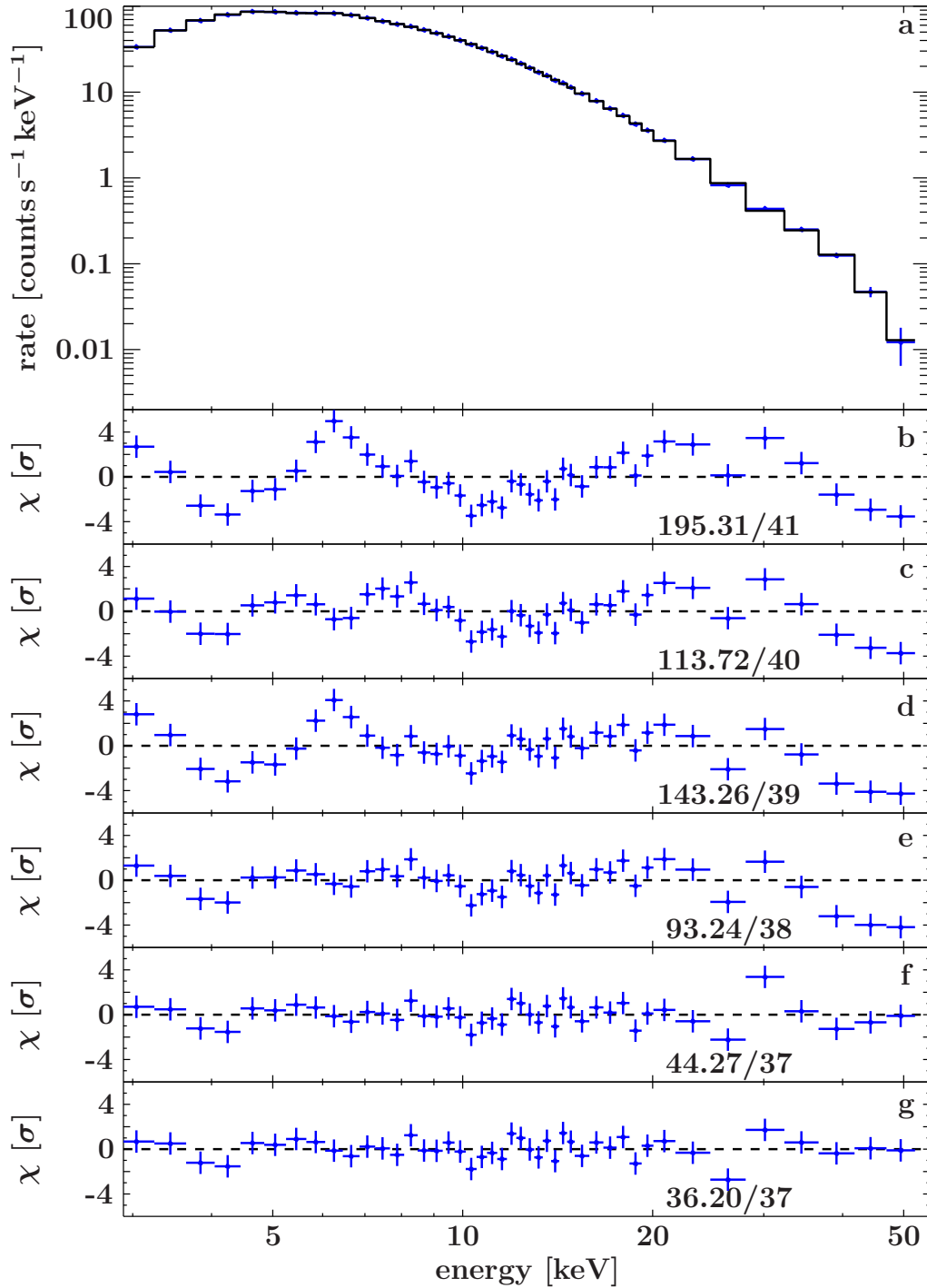
Figure 6.2: a: observed and reduced spectrum of GX 304−1 (ObsID 96369-01-05-02, blue data points) together with the best model (histogram). The model consists of an absorbed **CutoffPL** with a black body, an iron Kα fluorescence line, and a CRSF at ∼55 keV. Panels b–g show the residuals of the best fit when adding the single model components one by one. Panel b displays the residuals for an absorbed **CutoffPL**, in panels c and d the Fe Kα and the black body have been added respectively. Panel e shows the residuals when both of these two components are added to the model. Panel f shows the residuals, when allowing the PCA background to vary, and panel g when adding a CRSF at ∼55 keV, instead. Numbers indicate the values for χ^2/dof.
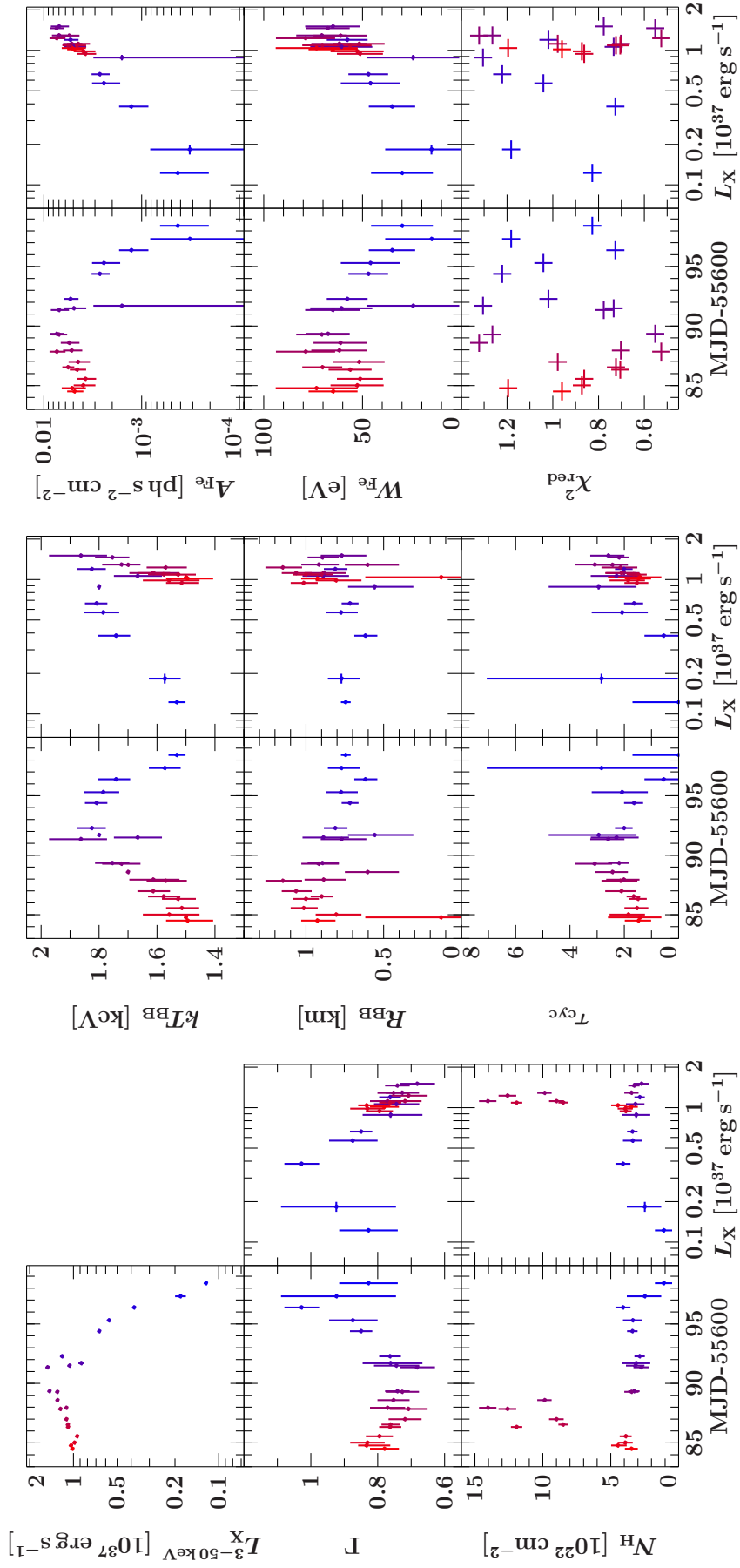
Figure 6.3: Spectral parameters as well as χ^2_{red} against time and flux. The color gradient from reddish to bluish data points indicates the temporal evolution of the outburst. Data points without error bars were held fixed to the displayed values. The flux covers the energy band 3 keV–50 keV.

Table 6.1: Continuum parameters of the time resolved spectral analysis. Fits were performed with the `CutoffPL` model and a varying number of CRSFs.

ObsID[a]	time[b]	$t_{\rm exp}$[c] [ks]	L_X[d]	N_H[e]	Γ	$R_{\rm BB}$ [km]	$T_{\rm BB}$ [keV]	$A_{\rm Fe}$[f]	$W_{\rm Fe}$ [eV]	τ	$\chi^2_{\rm red}$/dof
01-03-00	84.50–84.52	1.680	$1.02^{+0.02}_{-0.02}$	3.5 ± 0.5	0.78 ± 0.05	$0.93^{+0.10}_{-0.12}$	$0.93^{+0.10}_{-0.12}$	4.9 ± 1.0	65 ± 13	$1.5^{+0.6}_{-0.5}$	0.96/37
01-03-01	84.77–84.79	0.352	$1.04^{+0.03}_{-0.04}$	$4.5^{+0.5}_{-0.7}$	$0.834^{+0.025}_{-0.072}$	$0.13^{+0.49}_{-0.13}$	1.5	$5.2^{+1.4}_{-1.5}$	73 ± 20	$1.4^{+1.2}_{-0.8}$	1.20/38
01-03-02	85.01–85.02	1.168	0.99 ± 0.03	3.9 ± 0.6	0.83 ± 0.06	$0.81^{+0.14}_{-0.17}$	$0.81^{+0.14}_{-0.17}$	4.0 ± 1.0	53 ± 14	1.9 ± 0.7	0.87/37
01-04-00	85.54–85.57	2.224	0.94 ± 0.02	3.9 ± 0.5	0.80 ± 0.05	$1.02^{+0.09}_{-0.10}$	$1.02^{+0.09}_{-0.10}$	3.8 ± 0.9	51 ± 12	1.5 ± 0.5	0.86/37
01-05-00	86.31–86.36	3.584	1.09 ± 0.02	11.9 ± 0.5	0.76 ± 0.04	1.00 ± 0.09	1.00 ± 0.09	4.6 ± 0.9	56 ± 10	1.5 ± 0.4	0.70/37
01-05-01	86.45–86.62	6.656	1.09 ± 0.02	8.5 ± 0.4	$0.762^{+0.027}_{-0.028}$	$0.90^{+0.07}_{-0.08}$	$0.90^{+0.07}_{-0.08}$	5.7 ± 0.8	70 ± 10	$1.66^{+0.26}_{-0.25}$	0.72/37
01-05-02	86.96–87.00	1.264	1.12 ± 0.03	9.0 ± 0.6	0.72 ± 0.05	1.07 ± 0.10	1.07 ± 0.10	4.5 ± 1.2	52^{+14}_{-13}	2.1 ± 0.6	0.98/37
02-01-03	87.84–87.86	0.816	1.23 ± 0.03	12.6 ± 0.7	0.71 ± 0.06	$1.15^{+0.12}_{-0.13}$	$1.15^{+0.12}_{-0.13}$	7.4 ± 1.4	79^{+16}_{-15}	2.1 ± 0.7	0.53/37
02-01-04	87.94–87.96	1.104	1.12 ± 0.03	14.1 ± 0.7	0.77 ± 0.06	$0.89^{+0.13}_{-0.15}$	$0.89^{+0.13}_{-0.15}$	5.2 ± 1.2	62 ± 15	$2.0^{+0.7}_{-0.6}$	0.70/37
02-01-05	88.55–88.63	1.024	1.29 ± 0.03	9.9 ± 0.6	0.75 ± 0.05	$0.60^{+0.15}_{-0.20}$	1.7	$5.5^{+1.2}_{-1.3}$	61 ± 14	$2.4^{+0.7}_{-0.6}$	1.32/38
01-06-00	89.27–89.30	1.088	1.29 ± 0.03	3.5 ± 0.6	$0.73^{+0.05}_{-0.06}$	$0.92^{+0.12}_{-0.13}$	$0.92^{+0.12}_{-0.13}$	7.0 ± 1.3	71 ± 13	$3.1^{+0.8}_{-0.7}$	1.26/37
01-06-01	89.33–89.37	2.000	1.46 ± 0.03	3.3 ± 0.5	0.74 ± 0.04	0.90 ± 0.10	0.90 ± 0.10	7.4 ± 1.2	68 ± 12	$2.2^{+0.5}_{-0.4}$	0.55/37
01-06-03	91.34–91.36	0.720	1.51 ± 0.04	2.7 ± 0.6	0.68 ± 0.06	$0.77^{+0.14}_{-0.16}$	$0.77^{+0.14}_{-0.16}$	7.0 ± 1.5	65 ± 14	$2.6^{+0.7}_{-0.6}$	0.78/37
01-06-04	91.48–91.50	0.640	1.06 ± 0.04	3.2 ± 0.7	0.74 ± 0.07	$0.89^{+0.14}_{-0.17}$	$0.89^{+0.14}_{-0.17}$	4.9 ± 1.3	61 ± 16	$2.3^{+1.0}_{-0.9}$	0.73/37
01-07-00	91.69–91.71	0.256	0.88 ± 0.05	3.1 ± 1.0	$0.76^{+0.09}_{-0.10}$	$0.56^{+0.18}_{-0.25}$	1.8	1.6 ± 1.6	24 ± 24	$2.9^{+1.9}_{-1.4}$	1.31/38
01-07-01	92.25–92.30	3.856	1.20 ± 0.02	2.9 ± 0.4	0.76 ± 0.04	0.81 ± 0.08	0.81 ± 0.08	5.4 ± 1.0	58 ± 10	2.0 ± 0.4	1.02/37
01-08-00	94.32–94.46	7.776	0.66 ± 0.01	3.4 ± 0.4	0.85 ± 0.04	0.72 ± 0.06	0.72 ± 0.06	2.7 ± 0.6	47 ± 10	1.6 ± 0.4	1.22/37
01-08-01	95.29–95.30	1.136	0.57 ± 0.02	3.4 ± 0.8	0.87 ± 0.08	0.78 ± 0.10	0.78 ± 0.10	2.4 ± 0.8	46^{+16}_{-15}	$2.1^{+1.2}_{-1.0}$	1.04/37
01-09-00	96.34–96.42	4.208	0.38 ± 0.01	4.1 ± 0.6	1.03 ± 0.06	0.62 ± 0.08	0.62 ± 0.08	1.3 ± 0.5	35 ± 12	$0.6^{+0.8}_{-0.6}$	0.73/37
01-09-01	97.32–97.33	0.832	0.18 ± 0.02	$2.5^{+1.4}_{-1.3}$	$0.92^{+0.17}_{-0.18}$	$0.77^{+0.09}_{-0.12}$	$0.77^{+0.09}_{-0.12}$	$0.3^{+0.5}_{-0.3}$	15 ± 24	$2.8^{+4.3}_{-2.9}$	1.18/37
01-10-00	98.40–98.44	3.600	0.122 ± 0.003	1.1 ± 0.7	0.83 ± 0.09	0.75 ± 0.04	0.75 ± 0.04	0.4 ± 0.3	30 ± 16	≤1.7	0.83/37

Uncertainties and upper limits are at the 90% confidence level for one interesting parameter. Numbers without uncertainties were held fixed to the number stated. [a] PCA ObsID after 96369.- [b] MJD $- 55600$. [c] PCA exposure time. [d] Unabsorbed luminosity in units of 10^{37} erg s^{-1}. L_X covers the energy band 3–50 keV and was calculated using a distance of 2.4 kpc (Parkes et al., 1980). [e] In units of 10^{22} cm^{-2}. [f] In units of photons s^{-1} cm^{-2}.

6.5   Results and Discussion

THE analysis of the PCA spectra of this outburst is a very good example for one of the central difficulties for these kinds of studies. In this Section, we demonstrate how apparently good fits could lead to wrong interpretations and how temporal trends of spectral fit parameters could possibly be artificial, leading to erroneous conclusions.

6.5.1   The Photon Index

As is typical for accreting X-ray pulsars (e.g., Reig & Nespoli, 2013, and references cited therein), GX 304−1 shows a clear negative correlation between the photon index, and the X-ray flux. This result indicates a softer spectrum for higher fluxes.

6.5.2   Photoelectric Absorption

Since the effective area of the PCA for soft photons below $\sim 10\,\mathrm{keV}$ is relatively small, studying the temporal evolution of N_H is in most cases only possible with *Suzaku*'s or *XMM-Newton*'s instruments. However, in this analysis we find, even using the PCA, a remarkable result for the photoelectric absorption: while N_H mostly stays rather constant around $\sim 4 \times 10^{22}\,\mathrm{cm}^{-2}$ (which is in agreement with most of the values for N_H, found by Yamamoto et al., 2011b, using *Suzaku*), there is a significant jump at $55686 \lesssim \mathrm{MJD} \lesssim 55689$, to values up to $\sim 15 \times 10^{22}\,\mathrm{cm}^{-2}$. The spectral parameters N_H, Γ, and E_fold are known to be strongly correlated with each other (see, e.g., 4U 0115+634, Müller et al., 2013). Figure 6.4 shows, among others, the confidence contours between N_H and other fit parameters.

Note that for the calculations of these contours, E_fold was allowed to vary to account for possible influences of this parameter. These contours show that the change in N_H is not caused by some cross correlations with other parameters, and therefore has to be real. What kind of physical process can cause such an increase of the hydrogen column density?

The probably easiest explanation is a gas cloud which crosses the line of sight to the observer leading to absorption of soft X-rays. This cloud could possibly originate from the accreted material or from the stellar wind from the optical companion star. These stars are known to exhibit a clumpy structure of their winds (see, e.g., Oskinova et al., 2012, and references cited therein), leading to possible occultations of the X-ray emitting regions. However, since typical velocities of these winds are on the order of a few $10^3\,\mathrm{km\,s}^{-1}$ (e.g., Castor et al., 1975), a respective clump has to be unrealistically large to cause an occultation lasting several days as observed. Smaller relative velocities between the X-ray emitting region and a clump which are caused by the orbital motion of the neutron star are one possibility to solve this problem.

Another possible explanation is the occultation of the neutron star by the Be-disk of the optical companion. With an assumption of the orbital plane to be tilted with respect to the Be-disk, the orbital motion of the neutron star might lead to an occultation of the X-ray emitting region when the neutron star passes by behind the Be-disk. Such tilted planes were suggested by, e.g., Okazaki et al. (2013), giving a possible explanation of double outburst, as observed for this source in 2012 (see Fig. 6.1). The theory of a Be-disk occultation effect could be verified using observations of this system performed during different orbital cycles at the same orbital phase. *RXTE* observations of GX 304−1 from 2010 show an increase of N_H at MJD $\sim$ 55433
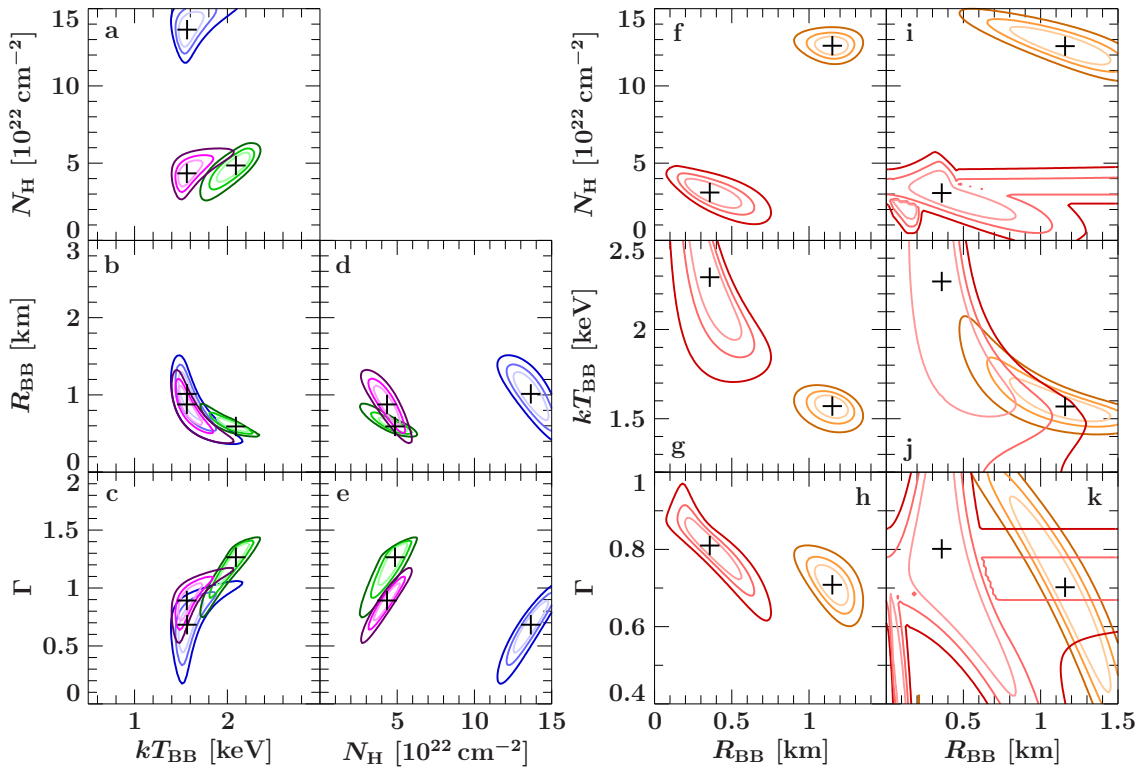
Figure 6.4: Confidence contours between several fit parameters for some selected fits. Contour lines correspond to the 68.3%, 90%, and 99% significance levels (from light to dark, respectively). Magenta lines correspond to ObsID 96369-01-04-00, green ones to 96369-01-08-01, blue ones to 96369-02-01-04, red ones to 96369-01-07-00, and orange ones to 96369-02-01-03. For all panels, except f, g, and h, E_{fold} has been allowed to vary. See text for further details.

(see Fig. 9 in Devasia et al., 2011, confirmed by Yamamoto et al., 2011b). Devasia et al. (2011) found a jump from $\sim$3 to $\sim$5 $\times 10^{22}\,\mathrm{cm}^{-2}$. In units of orbital periods (P_{orb} = 132.5 $\pm$ 0.4 d, Priedhorsky & Terrell, 1983), a conservative estimate of the time interval between the inset of these two events leads to $1.91 \pm 0.02\,P_{\mathrm{orb}}$, which is not consistent with an integer value as expected for regular events caused by the orbital motion. However, Be-disks are known to be highly variable with time (e.g., Norton et al., 1991, and references therein). This gives a possibe explanation of the slightly different orbital phases of these putative occultations and of the difference between the maximum values in 2010 and 2011 for N_{H} during these events.

Figure 6.5 (upper panel) shows the hardness ratio (HR) of the PCA light curves for different epochs. For these ratio curves, we used the 1–6 keV and the 10-100 keV light curves in the `GoodXenon` mode. We corrected these light curves for their variations caused by the pulsation of the neutron star and took an average of the count rate over bins as large as the pulse period. We obtained the pulse period by the epoch folding technique, as described in, e.g., Leahy et al. (1983). Since a higher value for N_{H} leads to a stronger absorption of the soft X-ray photons, this ratio is systematically higher for observations taken during the tentative occultation. In contrast to the HR with low N_{H}, where these values stays rather constant between $\sim$0.4 and $\sim$0.6, at higher values for N_{H}, these ratios vary within $\sim$0.5 and $\sim$0.9. This variation could be caused by changes of N_{H}, while for a higher column density the soft part of the spectrum gets more strongly absorbed. These variations of the order of hours could
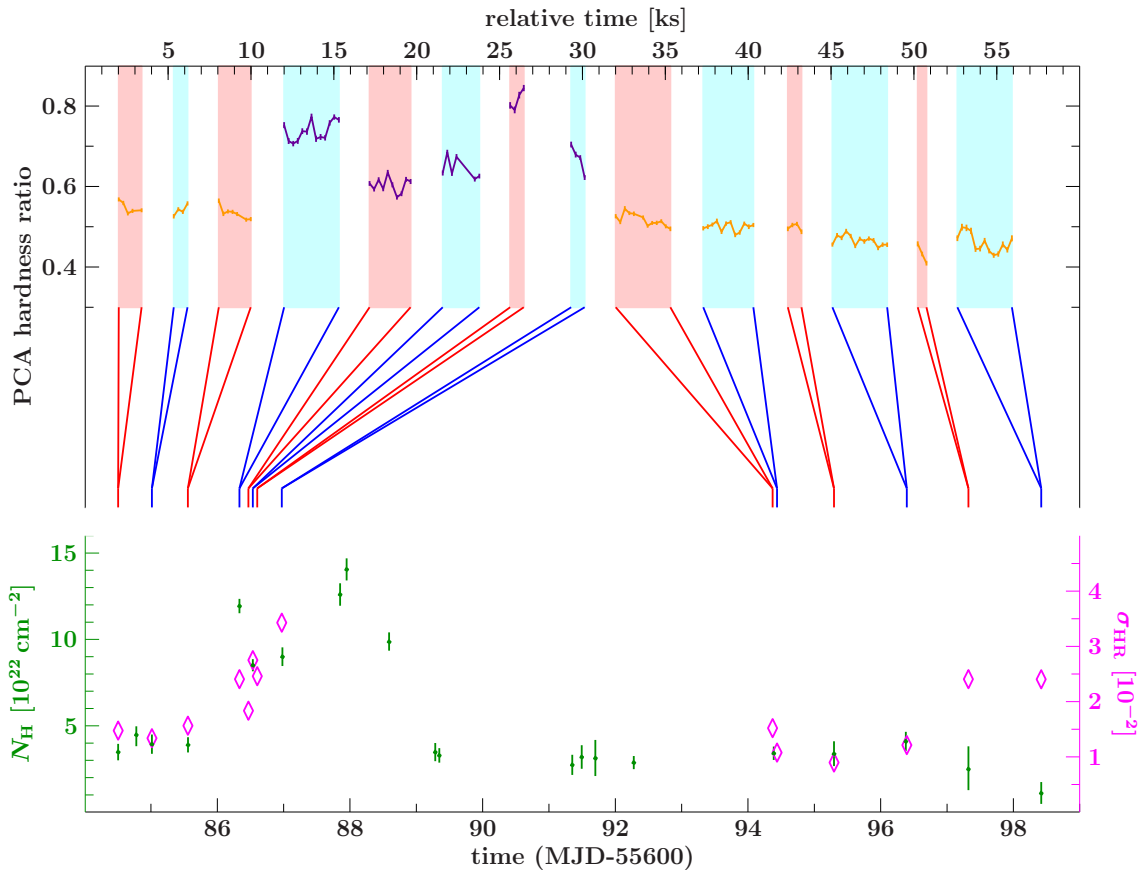
Figure 6.5: Upper panel: PCA hardness ratios for single ObsIDs (corresponding to the upper x-axis). Purple curves belong to ObsIDs with values for N_H greater than $7 \times 10^{22}\,\text{cm}^{-2}$, while orange curves belong to best fit values of N_H below this threshold. Ratios were calculated using the Equation (10–100 keV light curve)/(2–6 keV light curve). The lines below these ratios indicate the respective MJDs (lower x-axis). For clarity, these lines have the same colors as the respective shaded regions in the upper panel. Lower panel: Green data points display the temporal evolution of N_H during the outburst. Magenta diamonds show the standard deviation of the hardness ratio σ_{HR} from the upper panel.

be the evidence for respective density fluctuations of the Be-disk, through which the X-rays propagate. Such density variations were suggested by, e.g., McDavid et al. (2000), and references cited therein. Additionally to these variations on timescales of hours, the purple curves in the upper panel of Fig. 6.5 shows another significant HR variability of the order of a few 10 min, which is possibly caused by the same effect of N_H-variations in the Be-disk.

To check whether this scenario is consistent with typical densities for Be-disks, we adopt a value from Stee et al. (2013), who stated densities of the order of a few $10^{-11}\,\text{g}\,\text{cm}^{-3}$ for the disk of the Be-star HD 110432. Assuming the difference between N_H within the tentative occultation and outside to be $\Delta N_H \approx 10^{23}\,\text{cm}^{-2}$ and a mean density of the Be-disk of $5 \times 10^{-11}\,\text{g}\,\text{cm}^{-3}$ (which is of the order typical values for the density of Be-disks discussed in Stee et al., 2013), we obtain a distance of $d \approx 0.05 R_\odot$ for the X-rays propagating through a hydrogen cloud. Note that we only account for the case of non-ionized H atoms, which might leads to a systematic decrease of d. This value might be at first glance inconsistent with the result from Hanuschik (1996) that the thickness of a Be-disk can exceed the stellar radius. However, this

author furthermore concluded that at lower distances to the star, the Be-disk has to be comparably thin in height. Furthermore, deformations of the Be-disk caused by the gravitational force of the neutron star (as simulated by Okazaki et al., 2013) could lead to a decrease of the Be-disk's density. We conclude that the propagation distance of the X-rays through the medium is not in contradiction to typical Be-disk densities.

To verify the Be-disk occultation scenario further monitoring observations during outbursts, ideally performed with instruments sensitive at soft energies are required. If this scenario is real, observations with instruments with a high sensitivity will possibly allow for studies of the structures of Be-disks.

6.5.3   The Fe Kα Fluorescence Line

The Fe Kα fluorescence line is present in virtually all observations of GX 304−1 presented in this work. As seen for many X-ray binaries (among others, e.g., Inoue, 1985; Torrejón et al., 2010; Müller et al., 2012, 2013), we find a clear correlation between the X-ray flux and the flux of this feature. The equivalent width of this feature stays relatively constant within the uncertainties until MJD $\sim$ 55693, while at the dimming phase, the equivalent width decreases. Since this quantity depends on the material in the vicinity of the X-ray source (Torrejón et al., 2010), the amount of material has to decrease, or alternatively the neutron star removes from the fluorescing material by the orbital motion.

6.5.4   The Emission of the Black Body

Spectra with a high S/N require a further model component, i.e., a soft component which is described by the thermal emission of a black body. Figure 6.3 shows a hysteresis shaped change of the temperature of this soft component. However, Fig. 6.4 (panels b and c) clearly indicates strong cross correlations between this temperature and the radius as well as the photon index. It cannot be excluded that this apparent change in temperature is caused by a change of these other parameters.

For almost all spectra, the radius of the black body is relatively constant between $0.7\,\mathrm{km}$ and $1.2\,\mathrm{km}$ (Fig. 6.3). However, every now and then this value is significantly lower. Mukherjee et al. (2013) simulated magneto hydrodynamical instabilities in accretion mounds and found that for HMXBs above a threshold mass instabilities indeed can occur. Could the possible drops of R_{BB} be caused by these instabilities? Figure 6.4 (panels f, g, and h) displays confidence contours for two ObsIDs with a large difference in the radius. These panels indicate that this difference cannot be explained by cross correlations, but must be a real change. However, panels i, j, and k show the same confidence contours with E_{fold} allowed to vary. These panels show much larger, even chaotic, contours which intersect. These contours indicate that the change of R_{BB} might, despite the disjunct confidence contours in panels f, g, and h, be caused by changes of other parameters, or even by the frozen folding energy.

This result demonstrates a problem, which potentially affects all spectral analyses with frozen parameters. Calculating confidence contours with all parameters allowed to vary is an indispensable tool for these kinds of studies which prevents wrong conclusions.
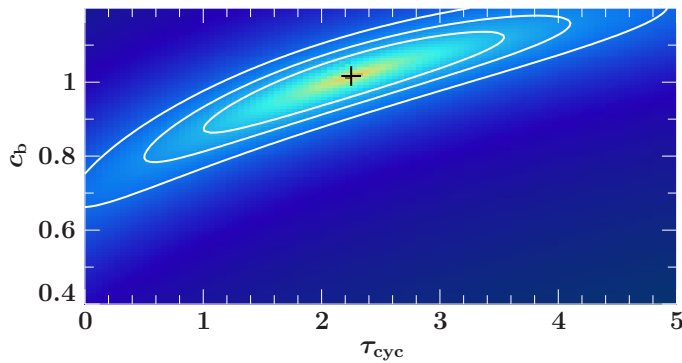
Figure 6.6: Confidence contours between the PCA background scaling constant c_b and the depth of a putative cyclotron line for ObsID 96369-01-05-02. Contour lines correspond to the 68.3%, 90%, and 99% levels. Color indicates $\Delta\chi^2$ with respect to the best fit value, with the color scale running from orange (low $\Delta\chi^2$) to dark blue (large $\Delta\chi^2$).

6.5.5 The Cyclotron Resonance Scattering Feature

Initial fit runs without a cyclotron line at $\sim 54\,\mathrm{keV}$ (Yamamoto et al., 2011b) led to acceptable fits with respect to χ^2_{red} (see Fig. 6.2f). However, the background scaling constant for these fits result in unrealistically low values of $(60 \pm 10)\%$ (see Sect. 6.3). Freezing c_b to 1 results in absorption like residuals at the high energy end of the detector's sensitivity around $50\,\mathrm{keV}$ (see Fig. 6.2e). Adding a cyclotron line feature with energy and width frozen to values from Yamamoto et al. (2011b), leads to acceptable fits with respect to χ^2_{red}. Showing a strong cross correlation, Fig. 6.6 demonstrates the capability of both model components, the varying background, and the cyclotron feature, to describe the data well. However, due to the unrealistically low value for c_b, we reject this model component and prefer the presence of the cyclotron feature (Yamamoto et al., 2011b).

Although the optical depth of this feature is nearly constant within the uncertainties (see Fig. 6.3), the effective area of the PCA is not sufficiently large at the affected energies to study variabilities of this feature as found by Klochkov et al. (2012). Beyond that, since the PCA covers only the red wing of this feature, it cannot be excluded that these residuals are in reality caused by some sort of high energy cutoff or other model specific problems. We conclude that it is not clear whether the cyclotron line is present, but we find at least evidence for this feature.

Chapter 7

Conclusions and Outlook

ACCRETING X-ray binary pulsars are systems where mass transfer from an optical companion star towards the neutron star leads to the emission of X-rays produced by interactions between the material and the extremely strong magnetic and gravitational fields in the vicinity of the compact object. From an observational point of view, these systems are, in particular with Be-companions, far away from being completely understood. For instance, the occurrence of outbursts of X-ray pulsars (e.g., XTE J1946+274, Sect. 4.4.1) strongly depends on the interactions of the Be-disks with the neutron stars. For this we need a well working general picture of Be-disks as well as a good knowledge of the orbits.

The work presented in this thesis is focussed on the analyses of X-ray spectra of Be-X-ray binaries recorded during outbursts. The modeling of these spectra is not straight forward. Complex physical processes within the accretion columns and largely unknown geometries induce the need of empirical models to describe the resulting X-ray spectra. A central result of my thesis is obtained through my analysis of 4U 0115+634 (Sect. 5), demonstrating a problem which potentially affects all spectral studies of this type of objects. The result that the same set of spectra can be modeled with different empirical models comparably well clearly shows a weak point of these kind of analyses. The probably worst consequence is the danger of possible misinterpretation of the results for spectral parameters and the respective wrong conclusions about the physical mechanisms behind. For 4U 0115+634 I address this problem regarding the behavior of the cyclotron line and revise previous results for the accretion regime of this source.

In the following Sect. 7.1 I summarize the main results for the three systems analyzed in this work in more detail. In Sect. 7.2 I give a future perspective regarding the science of accreted X-ray binary pulsars.

7.1 Results of the Systems in this Work

XTE J1946+274

After a phase of many years of quiescence, XTE J1946+274 underwent a series of outbursts which started in 2010. I perform a time resolved as well as a pulse phase resolved spectral analysis of quasi-simultaneous observations of *RXTE*, *INTEGRAL*, and *Swift*. I discuss several scenarios which might explain the enigmatic outburst behavior of XTE J1946+274, however, none of these scenarios can be clearly established

as the real one. I study the X-ray spectra using standard empirical continuum models. The detected disagreement between *RXTE* and *Swift* spectra can be explained by the presence of the emission of the galactic ridge in the *RXTE* spectra (e.g., Ebisawa et al., 2007). My result for the flux of this feature is consistent with values from literature (e.g., Yamauchi et al., 2009). A previously detected CRSF at $\sim$35 keV (Heindl et al., 2001) can be excluded for the data set I analyzed. I find weak evidence for the CRSF to be located at $\sim$25 keV at the 93% level, indicating that this feature might be variable between individual outbursts. The large difference of the results for the centroid energy of this feature cannot be explained by pure mass accretion rate effects, and, if real, have to be caused by a fundamentally different outburst behavior between individual outbursts.

4U 0115+634

With five observationally confirmed cyclotron lines, 4U 0115+634 is one of the most extensively studied X-ray sources. Using *RXTE* and *INTEGRAL* spectra of a giant outburst of 2008 together with a standard phenomenological continuum model, I reproduce previous results that 4U 0115+634 belongs to the group of cyclotron sources with a negative correlation between the X-ray flux and the fundamental cyclotron line energy (Nakajima et al., 2006; Tsygankov et al., 2007; Müller et al., 2010). Using another empirical continuum model, however, leads to a constant cyclotron line energy for all flux levels observed. This result is in contrast to virtually all previous analyses of the cyclotron lines in 4U 0115+634. In this thesis I demonstrate that the result of an anticorrelated cyclotron line energy with flux is caused by an unphysical interplay between the continuum parameters and the parameters of the cyclotron line, which in these cases rather models the broadband X-ray spectrum than representing a real CRSF. This result indicates that 4U 0115+634 does not accrete in the supercritical regime, as previously assumed. The boundary regimes from Becker et al. (2012) might have to be adjusted.

GX 304−1

GX 304−1 was regularly monitored during an outburst in 2011 April/May with *RXTE*. The results of the analysis of this data set are not in disagreement with a previous detected cyclotron line at $\sim$54 keV (Yamamoto et al., 2011b). I furthermore find a sudden increase of the equivalent hydrogen column density by a factor of about four, which after about three days declined to the initial value. I discuss several scenarios which might explain this detection. One of the most promising is the is the occultation of the X-ray emitting neutron star by the Be-disk of the optical companion star.

7.2 Outlook

A better understanding of the enigmatic outburst behaviors of X-ray pulsars is only possible with a better understanding of the nature of Be-disks. Further theoretical models based on computer simulations which describe the interactions between the neutron star and the Be-disk are needed to improve this situation. Simulations from, e.g., Okazaki et al. (2002) are the first step into this direction.

Regarding the spectra of X-ray binary pulsars, the ongoing development of physical model spectra based on analytical simulations of theoretical descriptions of the processes within accretion columns (e.g., Becker & Wolff, 2007; Schwarm, 2010, 2013, in prep.), have the potential to solve problems like the ambiguous results for 4U 0115+634 using different empirical continuum models (see Sect 5 and 7.1). These physically well-founded models which join the broadband continuum and the cyclotron lines will allow for spectral fits with a purely physical parameter space of X-ray spectra. With the recently successfully launched X-ray mission *NuSTAR* (Harrison et al., 2010), an instrument with slightly higher resolution than the *RXTE*-HEXTE or the *Suzaku*-HXD is now available. With its higher resolution and the much higher expected S/N in the spectra, we will be able, for the first time, to resolve cyclotron lines and study their luminosity-dependent behavior without the danger of a systematic influence of the choice of a continuum model.

Appendix A

Bibliography

Abramowicz M.A., Chen X., Kato S., et al., 1995, ApJ 438, L37

Alpar M.A., Cheng A.F., Ruderman M.A., Shaham J., 1982, Nat 300, 728

Als-Nielsen J., McMorrow D., 2001, Elements of Modern X-Ray Physics, Chichester: John Wiley & Sons Ltd

Anderson P.W., Itoh N., 1975, Nat 256, 25

Araya-Góchez R.A., Harding A.K., 2000, ApJ 544, 1067

Arnaud K.A., 1996, In: Jacoby G.H., Barnes J. (eds.) Astronomical Data Analysis Software and Systems V. ASP Conf. Ser. 101, San Francisco: ASP, p. 17

Aschenbach B., 2009, Exp. Astron. 26, 95

Barthelmy S.D., Barbier L.M., Cummings J.R., et al., 2005, Space Sci. Rev. 120, 143

Basko M.M., Sunyaev R.A., 1976, MN-RAS 175, 395

Becker P.A., Klochkov D., Schönherr G., et al., 2012, A&A 544, A123

Becker P.A., Wolff M.T., 2007, ApJ 654, 435

Bell S.J., Hewish A., 1967, Nat 213, 1214

Bildsten L., Chakrabarty D., Chiu J., et al., 1997, ApJS 113, 367

Blum S., Kraus U., 2000, ApJ 529, 968

Böck M., 2012, Ph.D. thesis, Friedrich-Alexander-Universität Erlangen-Nürnberg

Bodaghee A., Tomsick J.A., Rodriguez J., James J.B., 2012, ApJ 744, 108

Boldin P.A., Tsygankov S.S., Lutinov A.A., 2013, Astron. Let., submitted (arXiv:1305.6785)

Bondi H., Hoyle F., 1944, MNRAS 104, 273

Brainerd J., Lamb F.K., 1987, ApJ 317, L33

Brandt N., Podsiadlowski P., 1995, MN-RAS 274, 461

Burbidge E.M., Burbidge G.R., Fowler W.A., Hoyle F., 1957, Rev. Mod. Phys. 29, 547

Burrows D.N., Hill J.E., Nousek J.A., et al., 2005, Space Sci. Rev. 120, 165

Caballero I., Pottschmidt K., Marcu D.M., et al., 2013, ApJ 764, L23

Caballero I., Wilms J., 2012, MemSAIt 83, 230

Campana S., Israel G., Stella L., 1999, A&A 352, L91

Carroll B.W., Ostlie D.A., 2007, An Introduction to Modern Astrophysics, Reading: Addison-Wesley

Carter B., 1971, Phys. Rev. Lett. 26, 331

Castor J.I., Abbott D.C., Klein R.I., 1975, ApJ 195, 157

Chakrabarty D., Bildsten L., Finger M.H., et al., 1997, ApJ 481, L101

Chakrabarty D., Morgan E.H., Muno M.P., et al., 2003, Nat 424, 42

Chakrabarty D., van Kerkwijk M.H., Larkin J.E., 1998, ApJ 497, L39

Chandrasekhar S., 1931, ApJ 74, 81

Chauville J., Zorec J., Ballereau D., et al., 2001, A&A 378, 861

Coburn W., 2001, Ph.D. thesis, Univ. of California, San Diego

Coe M.J., 2000, In: Smith M.A., Henrichs H.F., Fabregat J. (eds.) The Be Phenomenon in Early-Type Stars, IAU Colloquium 175. ASP Conf. Ser. 214, San Francisco: ASP, p. 656

Collins G.W., 1987, In: Slettebak A., Snow T.P. (eds.) Physics of Be Stars. IAU Colloq. 92, Cambridge: Cambridge Univ. Press

Cominsky L., Clark G.W., Li F., et al., 1978, Nat 273, 367

Costa E., Frontera F., Heise J., et al., 1997, Nat 387, 783

Cui W., 1997, ApJ 482, L163

dal Fiume D., Orlandini M., Cusumano G., et al., 1998, A&A 329, L41

Daugherty J.K., Harding A.K., 1986, ApJ 309, 362

Dauser T., 2010, Diploma thesis, Friedrich-Alexander-Universität Erlangen-Nürnberg

Davidson K., 1973, Nature Physical Science 246, 1

Davis J.E., 2001, ApJ 548, 1010

Davis J.E., 2003, In: Truemper J.E., Tananbaum H.D. (eds.) X-Ray and Gamma-Ray Telescopes and Instruments for Astronomy. Proc. SPIE 4851, Bellingham, p.101

Degenaar N., Linares M., Altamirano D., Wijnands R., 2012, ApJ 759, 8

Devasia J., James M., Paul B., Indulekha K., 2011, MNRAS 417, 348

Draine B., 2011, Physics of the Interstellar and Intergalactic Medium, Princeton: Princeton University Press

Draper Z.H., Wisniewski J.P., Bjorkman K.S., et al., 2011, ApJ 728, L40

Dupree A.K., 1986, ARA&A 24, 377

Duro R., Dauser T., Wilms J., et al., 2011, A&A 533, L3

Ebisawa K., Maeda Y., Kaneda H., Yamauchi S., 2001, Sci 293, 1633

Ebisawa K., Yamauchi S., Tanaka Y., et al., 2007, Prog. Theor. Phys. Suppl. 169, 121

Erkut M.H., Alpar M.A., 2004, ApJ 617, 461

Fabregat J., Torrejón J.M., 2000, A&A 357, 451

Falkner S., 2013, Master thesis, Friedrich-Alexander-Universität Erlangen-Nürnberg, in prep.

Ferrigno C., Becker P.A., Segreto A., et al., 2009, A&A 498, 825

Ferrigno C., Falanga M., Bozzo E., et al., 2011, A&A 532, A76

Finger M.H., Bildsten L., Chakrabarty D., et al., 1999, ApJ 517, 449

Frank J., King A., Raine D., 1992, Accretion Power in Astrophysics, Cambridge: Cambridge University Press

Frémat Y., Neiner C., Hubert A.M., et al., 2006, A&A 451, 1053

Fürst F., 2011, Ph.D. thesis, Friedrich-Alexander-Universität Erlangen-Nürnberg

Fürst F., Kreykenbohm I., Suchy S., et al., 2011a, A&A 525, A73

Fürst F., Suchy S., Kreykenbohm I., et al., 2011b, A&A 535, A9

Fürst F., Wilms J., Rothschild R.E., et al., 2009, Earth and Planetary Science Letters 281, 125

Gehrels N., Chincarini G., Giommi P., et al., 2004, ApJ 611, 1005

Geier S., 2009, Ph.D. thesis, Friedrich-Alexander-Universität Erlangen-Nürnberg

Ghosh P., Lamb F.K., 1979, ApJ 234, 296

Ghosh P., Pethick C.J., Lamb F.K., 1977, ApJ 217, 578

Giacconi R., Gursky H., Paolini F.R., Rossi B.B., 1962, Phys. Rev. Lett. 9, 439

Giacconi R., Murray S., Gursky H., et al., 1972, ApJ 178, 281

Giacconi R., Rossi B., 1960, J. Geophys. Res. 65, 773

Glasser C.A., Odell C.E., Seufert S.E., 1994, IEEE Trans. Nucl. Sci. 41, 1343

Glendenning N.K., 1992, Phys. Rev. D 46, 4161

Gottlieb E.W., Wright E.L., Liller W., 1975, ApJ 195, L33

Göğüş E., Alpar M.A., Gilfanov M., 2007, ApJ 659, 580

Green D.A., Tuffs R.J., Popescu C.C., 2004, MNRAS 355, 1315

Green R.F., Schmidt M., Liebert J., 1986, ApJS 61, 305

Grinberg V., Hell N., Pottschmidt K., et al., 2013, A&A, in press (arXiv:1303.1198)

Grundstrom E.D., Boyajian T.S., Finch C., et al., 2007, ApJ 660, 1398

Haberl F., Pietsch W., 2004, A&A 414, 667

Haensel P., Potekhin A.Y., Yakovlev D.G., 2007, Neutron Stars 1: Equation of State and Structure, Astrophysics and Space Science Library, New York: Springer

Hanke M., 2007, Diploma thesis, Friedrich-Alexander-Universität Erlangen-Nürnberg

Hanke M., 2011, Ph.D. thesis, Friedrich-Alexander-Universität Erlangen-Nürnberg

Hanuschik R.W., 1996, A&A 308, 170

Harrison F.A., Boggs S., Christensen F., et al., 2010, In: Arnaud M., Murray S.S., Takahashi T. (eds.) Space Telescopes and Instrumentation 2010: Ultraviolet to Gamma Ray. Proc. SPIE 7732, Bellingham, p. 77320S

Heindl W.A., Coburn W., Gruber D.E., et al., 2000, In: McConnell M.L., Ryan J.M. (eds.) The 5th Compton Symp. AIP Conf. Proc. 510, New York: AIP, p.173

Heindl W.A., Coburn W., Gruber D.E., et al., 1999, ApJ 521, L49

Heindl W.A., Coburn W., Gruber D.E., et al., 2001, ApJ 563, L35

Hertel D., 2013, Diploma thesis, Friedrich-Alexander-Universität Erlangen-Nürnberg, in prep.

Hilditch R.W., 2001, An Introduction to Close Binary Stars, Cambridge: Cambridge University Press

Houck J.C., Denicola L.A., 2000, In: Manset N., Veillet C., Crabtree D. (eds.) Astronomical Data Analysis Software and Systems IX. ASP Conf. Ser. 216, San Francisco: ASP, p. 591

Hulse R.A., Taylor J.H., 1975, ApJ 195, L51

Illarionov A.F., Sunyaev R.A., 1975, A&A 39, 185

Inoue H., 1985, Space Sci. Rev. 40, 317

Jahoda K., Markwardt C.B., Radeva Y., et al., 2006, ApJS 163, 401

Johns M., Koski A., Canizares C., et al., 1978, IAU Circ. 3171

Kalberla P.M.W., Burton W.B., Hartmann D., et al., 2005, A&A 440, 775

Kaper L., van der Meer A., 2007, In: St.-Louis N., Moffat A.F.J. (eds.) Massive Stars in Interactive Binaries. ASP Conf. Ser. 367, San Francisco: ASP, p. 447

Karttunen H., Kröger P., Oja H., et al., (eds.) 2007, Fundamental Astronomy, Berlin: Springer

Kepler S.O., Kleinman S.J., Nitta A., et al., 2007, MNRAS 375, 1315

Kippenhahn R., Weigert A., 1990, Stellar Structure and Evolution, Berlin: Springer, 5th edition

Kirsch M.G., Briel U.G., Burrows D., et al., 2005, In: Siegmund O.H.W. (ed.) UV, X-Ray, and Gamma-Ray Space Instrumentation for Astronomy XIV. Proc. SPIE 5898, Bellingham, p.22

Klochkov D., Doroshenko V., Santangelo A., et al., 2012, A&A 542, L28

Klochkov D., Ferrigno C., Santangelo A., et al., 2011a, A&A 536, L8

Klochkov D., Horns D., Santangelo A., et al., 2007, A&A 464, L45

Klochkov D., Santangelo A., Staubert R., Ferrigno C., 2008, A&A 491, 833

Klochkov D., Staubert R., Santangelo A., et al., 2011b, A&A 532, A126

Knoll G.F., 2010, Radiation detection and measurement, New York: Wiley, 4th edition

Kostov V.B., McCullough P.R., Hinse T.C., et al., 2013, ApJ 770, 52

Koyama K., Tsunemi H., Dotani T., et al., 2007, PASJ 59, 23

Kraus U., Nollert H.P., Ruder H., Riffert H., 1995, ApJ 450, 763

Kraus U., Zahn C., Weth C., Ruder H., 2003, ApJ 590, 424

Krauß F., 2013, Master thesis, Friedrich-Alexander-Universität Erlangen-Nürnberg

Kretschmar P., 1996, Ph.D. thesis, Eberhard-Karls Universität Tübingen

Kreykenbohm I., 1997, Master's thesis, Eberhard Karls Universität Tübingen

Kreykenbohm I., 2004, Ph.D. thesis, Eberhard-Karls-Universität Tübingen

Kreykenbohm I., Coburn W., Wilms J., et al., 2002, A&A 395, 129

Kreykenbohm I., Göğüş E., Belloni T., et al., 2010, In: Eighth Integral Workshop. The Restless Gamma-ray Universe (INTEGRAL 2010), PoS (INTEGRAL 2010) 60.

Kreykenbohm I., Kretschmar P., Wilms J., et al., 1999, A&A 341, 141

Krimm H.A., Barthelmy S.D., Baumgartner W., et al., 2010, ATel 2663

Kühnel M., 2011, Master thesis, Friedrich-Alexander-Universität Erlangen-Nürnberg

Kühnel M., Müller S., Kreykenbohm I., et al., 2013, A&A, in press

La Palombara N., Sidoli L., Esposito P., et al., 2012, A&A 539, A82

Labanti C., Di Cocco G., Ferro G., et al., 2003, A&A 411, L149

Lamb F.K., Miller M.C., 2001, ApJ 554, 1210

Langer S.H., Rappaport S., 1982, ApJ 257, 733

Larionov V., Arkharov A., 2008, ATel 1427

Lasota J.P., 2001, New Astron. Rev. 45, 449

Lattimer J.M., Prakash M., 2001, ApJ 550, 426

Lattimer J.M., Prakash M., 2004, Sci 304, 536

Leahy D.A., 1991, MNRAS 251, 203

Leahy D.A., 2002, A&A 391, 219

Leahy D.A., Darbro W., Elsner R.F., et al., 1983, ApJ 266, 160

Lebrun F., Leray J.P., Lavocat P., et al., 2003, A&A 411, L141

Lense J., Thirring H., 1918, Phys. Z. 19, 156

Levine A.M., Bradt H., Cui W., et al., 1996, ApJ 469, L33

Lewin W.H.G., Clark G.W., Smith W.B., 1968, Nat 219, 1235

Lewin W.H.G., van Paradijs J., van den Heuvel E.P.J., (eds.) 1995, X-Ray Binaries, Cambridge: Cambridge University Press

Li J., Wang W., Zhao Y., 2012, MNRAS 423, 2854

Li Z., Han Z., 2008, ApJ 685, 225

Liebert J., Bergeron P., Holberg J.B., 2005, ApJS 156, 47

Liebert J., Fontaine G., Young P.A., et al., 2013, ApJ 769, 7

Liu Q.Z., van Paradijs J., van den Heuvel E.P.J., 2000, A&AS 147, 25

Liu Q.Z., van Paradijs J., van den Heuvel E.P.J., 2005, A&A 442, 1135

Liu Q.Z., van Paradijs J., van den Heuvel E.P.J., 2007, A&A 469, 807

Lovelace R.V.E., Romanova M.M., Bisnovatyi-Kogan G.S., 1995, MNRAS 275, 244

Lund N., Budtz-Jørgensen C., Westergaard N.J., et al., 2003, A&A 411, L231

Maeder A., 2009, Physics, Formation and Evolution of Rotating Stars, Berlin: Springer

Makishima K., Mihara T., Nagase F., Tanaka Y., 1999, ApJ 525, 978

Manchester R.N., Hobbs G.B., Teoh A., Hobbs M., 2005, AJ 129, 1993

Manousakis A., Beckmann V., Bianchin V., et al., 2008, ATel 1613

Markowitz A., Reeves J.N., George I.M., et al., 2009, ApJ 691, 922

Martin R.G., Pringle J.E., Tout C.A., Lubow S.H., 2011, MNRAS 416, 2827

Mas-Hesse J.M., Giménez A., Culhane J.L., et al., 2003, A&A 411, L261

Masetti N., Landi R., Pretorius M.L., et al., 2007, A&A 470, 331

Masetti N., Orlandini M., Palazzi E., et al., 2006, A&A 453, 295

Mason K.O., Murdin P.G., Parkes G.E., Visvanathan N., 1978, MNRAS 184, 45P

Mauche C.W., Liedahl D.A., Akiyama S., Plewa T., 2008, In: Axelsson M. (ed.) Cool Discs, Hot Flows: The Varying Faces of Accreting Compact Objects. AIP Conf. Proc. 1054, New York: AIP, p.3

McBride V.A., Wilms J., Coe M.J., et al., 2006, A&A 451, 267

McClintock J.E., Nugent J.J., Li F.K., Rappaport S.A., 1977, ApJ 216, L15

McCulloch P.M., Klekociuk A.R., Hamilton P.A., Royle G.W.R., 1987, Aust. J. Phys. 40, 725

McDavid D., Bjorkman K.S., Bjorkman J.E., Okazaki A.T., 2000, In: Smith M.A., Henrichs H.F., Fabregat J. (eds.) The Be Phenomenon in Early-Type Stars, IAU Colloquium 175. ASP Conf. Ser. 214, San Francisco: ASP, p. 460

Mermilliod J.C., 1982, A&A 109, 48

Mészáros P., 1984, In: Woosley S.E. (ed.) High Energy Transients in Astrophysics. AIP Conf. Proc. 115, New York: AIP, p.165

Mészáros P., 1992, High-Energy Radiation from Magnetized Neutron Stars, Chicago: University of Chicago Press

Mészáros P., Nagel W., 1985, ApJ 298, 147

Mészáros P., Riffert H., Berthiaume G., 1988, ApJ 325, 204

Mihara T., Makishima K., Nagase F., 2004, ApJ 610, 390

Mihara T., Makishima K., Ohashi T., et al., 1990, Nat 346, 250

Mitsuda K., Bautz M., Inoue H., et al., 2007, PASJ 59, 1

Morihana K., Tsujimoto M., Yoshida T., Ebisawa K., 2013, ApJ 766, 14

Moritani Y., Nogami D., Okazaki A.T., et al., 2011, PASJ 63, L25

Mowlavi N., Kreykenbohm I., Shaw S., et al., 2006, A&A 451, 817

Mukherjee D., Bhattacharya D., 2012, MNRAS 420, 720

Mukherjee D., Bhattacharya D., Mignone A., 2013, MNRAS 430, 1976

Müller S., 2009, Diploma thesis, Friedrich-Alexander-Universität Erlangen-Nürnberg

Müller S., Ferrigno C., Kühnel M., et al., 2013, A&A 551, A6

Müller S., Geier S., Heber U., 2010a, Ap&SS 329, 101

Müller S., Kühnel M., Caballero I., et al., 2012, A&A 546, A125

Müller S., Kühnel M., Pottschmidt K., et al., 2010b, ATel 3077

Müller S., Obst M., Kreykenbohm I., et al., 2010, In: Eighth Integral Workshop. The Restless Gamma-ray Universe (INTEGRAL 2010), PoS (INTEGRAL 2010) 116.

Nagase F., Dotani T., Tanaka Y., et al., 1991, ApJ 375, L49

Nagel W., 1980, ApJ 236, 904

Naik S., Maitra C., Jaisawal G.K., Paul B., 2013, ApJ 764, 158

Nakajima M., Mihara T., Makishima K., 2010, ApJ 710, 1755

Nakajima M., Mihara T., Makishima K., Niko H., 2006, ApJ 646, 1125

Negueruela I., Okazaki A.T., 2001, A&A 369, 108

Negueruela I., Reig P., Coe M.J., Fabregat J., 1998, A&A 336, 251

Nelson R.W., Salpeter E.E., Wasserman I., 1993, ApJ 418, 874

Nespoli E., Fabregat J., Mennickent R.E., 2010, A&A 516, A94

Norton A.J., Coe M.J., Estela A., et al., 1991, MNRAS 253, 579

Nowak M.A., Hanke M., Trowbridge S.N., et al., 2011, ApJ 728, 13

Odaka H., Khangulyan D., Tanaka Y.T., et al., 2013, ApJ 767, 70

Okazaki A.T., Bate M.R., Ogilvie G.I., Pringle J.E., 2002, MNRAS 337, 967

Okazaki A.T., Hayasaki K., Moritani Y., 2013, PASJ 65, 41

Okazaki A.T., Nagataki S., Naito T., et al., 2011, In: Active OB stars: structure, evolution, mass loss, and critical limits. Proc. IAU Sym 272, Cambridge: Cambridge University Press, p. 628

Okazaki A.T., Negueruela I., 2001, A&A 377, 161

Oskinova L.M., Feldmeier A., Kretschmar P., 2012, MNRAS 421, 2820

Özel F., 2006, Nat 441, 1115

Parkes G.E., Murdin P.G., Mason K.O., 1980, MNRAS 190, 537

Paul B., Dotani T., Nagase F., et al., 2005, ApJ 627, 915

Podsiadlowski P., Rappaport S., Han Z., 2003, MNRAS 341, 385

Porter J.M., Rivinius T., 2003, PASP 115, 1153

Pottschmidt K., Kreykenbohm I., Wilms J., et al., 2005, ApJ 634, L97

Pottschmidt K., Rothschild R.E., Gasaway T., et al., 2006, In: AAS/High Energy Astrophysics Division #9. BAAS 38, p. 384

Priedhorsky W.C., Terrell J., 1983, ApJ 273, 709

Pringle J.E., 1996, MNRAS 281, 357

Pustylnik I.B., 2005, Ap&SS 296, 69

Rappaport S., Clark G.W., Cominsky L., et al., 1978, ApJ 224, L1

Raubenheimer B.C., 1990, A&A 234, 172

Reig P., Nespoli E., 2013, A&A 551, A1

Rivinius T., Baade D., Štefl S., Maintz M., 2001, A&A 379, 257

Rothschild R.E., Blanco P.R., Gruber D.E., et al., 1998, ApJ 496, 538

Rothschild R.E., Markowitz A., Rivers E., et al., 2011, ApJ 733, 23

Ruderman M., 1991, ApJ 382, 587

Russeil D., 2003, A&A 397, 133

Sako M., Kahn S.M., Paerels F., et al., 2003, In: High Resolution Spectroscopy with XMM-Newton and Chandra. Invited review, MSSL workshop Oct. 24–25 [arXiv:astroph/0309503]

Sala G., Haberl F., José J., et al., 2012, ApJ 752, 158

Santangelo A., Segreto A., Giarrusso S., et al., 1999, ApJ 523, L85

Sasaki M., Klochkov D., Kraus U., et al., 2010, A&A 517, A8

Schaffenroth V., Geier S., Drechsel H., et al., 2013, A&A 553, A18

Schmid C., 2012, Ph.D. thesis, Friedrich-Alexander-Universität Erlangen-Nürnberg

Schönherr G., Wilms J., Kretschmar P., et al., 2007, A&A 472, 353

Schwarm F.W., 2010, Diploma thesis, Friedrich-Alexander-Universität Erlangen-Nürnberg

Schwarm F.W., 2013, Ph.D. thesis, Friedrich-Alexander-Universität Erlangen-Nürnberg, in prep.

Serlemitsos P.J., Soong Y., Chan K.W., et al., 2007, PASJ 59, 9

Shakura N., Postnov K., Kochetkova A., Hjalmarsdotter L., 2012, MNRAS 420, 216

Shakura N.I., Sunyaev R.A., 1973, A&A 24, 337

Shapiro S.L., Lightman A.P., 1976, ApJ 204, 555

Shu F.H., Adams F.C., Lizano S., 1987, ARA&A 25, 23

Slettebak A., 1988, PASP 100, 770

Smith D.A., Takeshima T., 1998, ATel 36

Staubert R., Shakura N.I., Postnov K., et al., 2007, A&A 465, L25

Stee P., Meilland A., Bendjoya P., et al., 2013, A&A 550, A65

Stella L., Vietri M., 1998, ApJ 492, L59

Strohmayer T.E., Zhang W., Swank J.H., et al., 1996, ApJ 469, L9

Struve O., 1931, ApJ 73, 94

Suchy S., Pottschmidt K., Rothschild R.E., et al., 2011, ApJ 733, 15

Suchy S., Pottschmidt K., Wilms J., et al., 2008, ApJ 675, 1487

Swank J.H., Becker R.H., Boldt E.A., et al., 1976, ApJ 209, L57

Takahashi T., Abe K., Endo M., et al., 2007, PASJ 59, 35

Tanaka Y., 1986, In: Mihalas D., Winkler K.H. (eds.) Radiation Hydrodynamics in Stars and Compact Objects. Proceedings of Colloquium No. 89 of the IAU 255, Berlin, Heidelberg: Springer, p.198

ten Brummelaar T., Mason B.D., McAlister H.A., et al., 2000, AJ 119, 2403

Titarchuk L., 1994, ApJ 434, 570

Toor A., Seward F.D., 1977, ApJ 216, 560

Torrejón J.M., Schulz N.S., Nowak M.A., Kallman T.R., 2010, ApJ 715, 947

Touhami Y., Gies D.R., Schaefer G.H., et al., 2013, ApJ 768, 128

Townsend R.H.D., Owocki S.P., Howarth I.D., 2004, MNRAS 350, 189

Tsygankov S.S., Lutovinov A.A., Churazov E.M., Sunyaev R.A., 2006, MNRAS 371, 19

Tsygankov S.S., Lutovinov A.A., Churazov E.M., Sunyaev R.A., 2007, Astronomy Letters 33, 368

Tutukov A.V., Yungel'Son L.R., 1993, Astr. Rep. 37, 411

Ubertini P., Lebrun F., Di Cocco G., et al., 2003, A&A 411, L131

Unger S.J., Roche P., Negueruela I., et al., 1998, A&A 336, 960

Unsöld A., Baschek B., 2001, The new cosmos: an introduction to astronomy and astrophysics, Berlin: Springer, 5th edition

Štefl S., 1999, In: Wolf B., Stahl O., Fullerton A.W. (eds.) Variable and Non-spherical Stellar Winds in Luminous Hot Stars. Lecture Notes in Physics 523, Heidelberg: Springer, p.24

Vallée J.P., 2008, ApJ 681, 303

van der Klis M., 1989, ARA&A 27, 517

van der Klis M., Swank J.H., Zhang W., et al., 1996, ApJ 469, L1

Vedrenne G., Roques J.P., Schönfelder V., et al., 2003, A&A 411, L63

Verner D.A., Yakovlev D.G., 1995, A&AS 109, 125

Verrecchia F., Israel G.L., Negueruela I., et al., 2002, A&A 393, 983

Vrtilek S.D., Boroson B.S., 2013, MNRAS 428, 3693

Warwick R.S., Turner M.J.L., Watson M.G., Willingale R., 1985, Nat 317, 218

Wheaton W.A., Doty J.P., Primini F.A., et al., 1979, Nat 282, 240

White N.E., 1989, A&AR 1, 85

White N.E., Swank J.H., Holt S.S., 1983, ApJ 270, 711

Wilms J., Allen A., McCray R., 2000, ApJ 542, 914

Wilson C.A., Finger M.H., Coe M.J., Negueruela I., 2003, ApJ 584, 996

Wilson C.A., Finger M.H., Wilson R.B., Scott D.M., 1998, IAU Circ. 7014, 2

Wilson-Hodge C.A., Cherry M.L., Case G.L., et al., 2011, ApJ 727, L40

Winkler C., 2012, In: An INTEGRAL view of the high-energy sky (the first 10 years), PoS (INTEGRAL 2012) 001.

Winkler C., Courvoisier T.J.L., Di Cocco G., et al., 2003, A&A 411, L1

Wolter H., 1952, Annalen der Physik 445, 286

Worrall D.M., Marshall F.E., Boldt E.A., Swank J.H., 1982, ApJ 255, 111

Yamamoto T., Mihara T., Sugizaki M., et al., 2011a, ATel 3309

Yamamoto T., Sugizaki M., Mihara T., et al., 2011b, PASJ 63, 751

Yamauchi S., Ebisawa K., Tanaka Y., et al., 2009, PASJ 61, 225

Yan J., Li H., Liu Q., 2012, ApJ 744, 37

Yokogawa J., Imanishi K., Tsujimoto M., et al., 2003, PASJ 55, 161

Zhang W., Smale A.P., Strohmayer T.E., Swank J.H., 1998, ApJ 500, L171

Zhang Z., Gilfanov M., Bogdan A., 2013, A&A in press (arXiv: 1211.0399)

Zorec J., Briot D., 1997, A&A 318, 443

Appendix B

Acknowledgements

O NE of the parts of a Ph.D. thesis where one can make the worst mistakes is probably the "Thank You"-Section. Many people have supported me during the last years and helped making this thesis possible. Before I start thanking individual people, I would like to emphasize that the Dr. Karl Remeis observatory in Bamberg is a perfect place to work. Especially the "everybody helps everybody"-mentality at the observatory leads to a perfect environment to learn and study. Therefore, I would like to say thank you to all people of the observatory.

Especially I want to thank my supervisor Jörn Wilms for the opportunity to do my Ph.D. and for believing in me. I highly appreciate that, even on days with massive workload, he never hesitates to support, to discuss, and to help with problems. I am very grateful to him for sending me to conferences, where I presented my work and got in contact with other scientists. His supporting and motivating way to supervise leads to a perfect atmosphere to successfully perform science.

I furthermore want to thank my office mates of the "Kniggezimmer" for the good working atmosphere, the discussions, and also the nonsense we sometimes did together. I am aware that not everybody enjoys my every now and then appearing wordplays and you guys have mostly been directly within the firing line. I am very grateful to Matthias Kühnel for plenty of neutron star related discussions. Many outcomes of this work have their origin in these discussions. Additionally, Matthias deserves many thanks for his readiness to help others with ISIS issues and computer related problems. I furthermore want to thank Stephan Geier. His sunny disposition contributed much to the great atmosphere in our office, but also his scientific expertise helped frequently. Especially for the "Spreizblock"-project, I wish Stephan great success. I want to thank Dominik Hertel for his patience concerning the *Suzaku* extraction and for many discussions especially related to 4U 0115+634. I would like to thank Christian Heuser for being a good colleague and hope he will be successful in his fight against rip-off artists selling things like "filters for nuclear power generated electricity". I want to thank Ralf Ballhausen who just started working on X-ray binary pulsars in the Knigge room. I would like to express my gratitude to the former Kniggerians Lew Classen, Thomas Kupfer, Patrick Brünner, Heiko Hirsch, and Viktoria Lohmann. It has been a great honor for me to have shared the office with all of you and I want to thank you for the absolutely great working atmosphere.

I would like to thank Ingo Kreykenbohm. The discussions with him helped me a lot to get into the field of X-ray neutron star binaries. I want to thank Ingo for proofreading numerous paper drafts and for his excellent job as a computer administrator. Many thanks go to Felix Fürst from whom I learned lots of things related

to X-ray analysis. I appreciate Felix' very helpful comments on paper drafts. Talking about good comments, I want to thank Katja Pottschmidt for many discussions. I admire Katja for her ability to find even the tiniest mistakes in paper drafts and her perfectionism. I thank Victoria Grinberg. She helped many times with *INTEGRAL* data extractions and analyses. Thanks go to Manfred Hanke, who helped me a lot with ISIS related problems, especially during my first months at the observatory. I want to express my gratefulness to Fritz-Walter Schwarm for discussions about the theory behind cyclotron lines, and also for his computer administrations. Furthermore, I want to say thank you to Tommy Dauser for his frequent help with computer related issues. I thank Sebastian Falkner for discussions about the relations between accretion geometry of neutron stars and pulse profiles. I thank Maria Obst, for 4U 0115+634 related discussions. Furthermore, I thank Moritz Böck for his competent advice, not only with respect to flux calculations. Natalie Hell deserves thanks for critically proofreading some parts of my work and teaching me lots of grammar. I want to thank Gabi Schönherr, especially for her last-minute support. Furthermore, I want to thank Frau Bues. From being my first academic teacher of astronomy to proofreading my work, I cannot imagine the Remeis observatory without her. I would like to thank the working group around Uli Heber and Horst Drechsel for contributing to the great atmosphere at the observatory. I would like to thank Edith Day. Her enthusiasm concerning administration helped me, as a person hating red tape, many times. I want to thank my summer student Jieun Choi and the DAAD for making this campaign possible. Jieun spent the summer 2011 at our institute in Bamberg and I had the pleasure to work with her together on the system GX 304–1. I want to thank her for the great collaboration. I would like to say thank you to Carlo Ferrigno. I am very grateful for the excellent teamwork with him regarding 4U 0115+634.

During my time in Bamberg we started a collaboration with colleagues in Alicante/Spain. I would like to thank José Miguel Torrejón, Silvia Martínez Núñez, José Joaquín Rodes-Rocas, Guillermo Bernabéu, Ana González Galán, and Ángel Giménez García for the very good teamwork and discussions.

Talking about good collaborations, I would like to thank the people of the MAG-NET collaboration. Our regular telecons were a great opportunity to get a wider view of the field of X-ray pulsars. Especially, I would like to thank Rick Rothschild, Gabi Schönherr, Isabel Caballero, Slawomir Suchy, Diana Marcu, Peter Kretschmar, and Rüdiger Staubert for many discussions and advice relating to our science.

Financially I want to thank the *Deutsches Zentrum für Luft- und Raumfahrt* for funding my PhD position (grant 50OR0905). For this work, I often made use of NASA's High Energy Astrophysics Science Archive Research Center's data browser[1] as well as of the Digital Library "The SAO/NASA Astrophysics Data System"[2]. For this work I used data from NASA's missions *RXTE* and *Swift*. Concerning the latter mission, I want to thank Neil Gehrels and the *Swift* operations team for making short notice ToO observations of XTE J1946+274 possible. Furthermore, I made use of data obtained by *INTEGRAL*. This is an ESA project with instruments and science data centre funded by ESA member states (especially the PI countries: Denmark, France, Germany, Italy, Switzerland, Spain), Czech Republic, and Poland, and with the participation of Russia and the USA. To verify my results on 4U 0115+634, I used data from *Suzaku*, a collaborative mission between JAXA and NASA. I would like to thank the MIT, especially J. C. Houck and J. E. Davis, for the development and the

---

[1]http://heasarc.gsfc.nasa.gov/cgi-bin/W3Browse/w3browse.pl
[2]http://adsabs.harvard.edu/abstract_service.html

Thank you!

Danke!